

1996

# FTIR analysis of transient CO<sub>2</sub> emissions in a circulating fluidized bed boiler

Thomas Steven Raines  
*Iowa State University*

Follow this and additional works at: <https://lib.dr.iastate.edu/rtd>

 Part of the [Chemical Engineering Commons](#), and the [Mechanical Engineering Commons](#)

## Recommended Citation

Raines, Thomas Steven, "FTIR analysis of transient CO<sub>2</sub> emissions in a circulating fluidized bed boiler " (1996). *Retrospective Theses and Dissertations*. 11334.  
<https://lib.dr.iastate.edu/rtd/11334>

This Dissertation is brought to you for free and open access by the Iowa State University Capstones, Theses and Dissertations at Iowa State University Digital Repository. It has been accepted for inclusion in Retrospective Theses and Dissertations by an authorized administrator of Iowa State University Digital Repository. For more information, please contact [digirep@iastate.edu](mailto:digirep@iastate.edu).

## INFORMATION TO USERS

This manuscript has been reproduced from the microfilm master. UMI films the text directly from the original or copy submitted. Thus, some thesis and dissertation copies are in typewriter face, while others may be from any type of computer printer.

**The quality of this reproduction is dependent upon the quality of the copy submitted.** Broken or indistinct print, colored or poor quality illustrations and photographs, print bleedthrough, substandard margins, and improper alignment can adversely affect reproduction.

In the unlikely event that the author did not send UMI a complete manuscript and there are missing pages, these will be noted. Also, if unauthorized copyright material had to be removed, a note will indicate the deletion.

Oversize materials (e.g., maps, drawings, charts) are reproduced by sectioning the original, beginning at the upper left-hand corner and continuing from left to right in equal sections with small overlaps. Each original is also photographed in one exposure and is included in reduced form at the back of the book.

Photographs included in the original manuscript have been reproduced xerographically in this copy. Higher quality 6" x 9" black and white photographic prints are available for any photographs or illustrations appearing in this copy for an additional charge. Contact UMI directly to order.

# UMI

A Bell & Howell Information Company  
300 North Zeeb Road, Ann Arbor MI 48106-1346 USA  
313/761-4700 800/521-0600



**FTIR analysis of transient CO<sub>2</sub> emissions  
in a circulating fluidized bed boiler**

**by**

**Thomas Steven Raines**

**A Dissertation Submitted to the  
Graduate Faculty in Partial Fulfillment of the  
Requirements for the Degree of  
DOCTOR OF PHILOSOPHY**

**Department: Mechanical Engineering  
Major: Mechanical Engineering**

**Approved:**

Signature was redacted for privacy.

**In Charge of Major Work**

Signature was redacted for privacy.

**For the Major Department**

Signature was redacted for privacy.

**For the Graduate College**

**Iowa State University  
Ames, Iowa**

**1996**

**Copyright © Thomas Steven Raines 1996. All rights reserved.**

**UMI Number: 9626063**

**Copyright 1996 by  
Raines, Thomas Steven**

**All rights reserved.**

---

**UMI Microform 9626063  
Copyright 1996, by UMI Company. All rights reserved.**

**This microform edition is protected against unauthorized  
copying under Title 17, United States Code.**

---

**UMI**  
**300 North Zeeb Road**  
**Ann Arbor, MI 48103**

**TABLE OF CONTENTS**

1.	INTRODUCTION .....	1
2.	COAL COMBUSTION THEORY .....	4
2.1	Composition of Coal .....	4
2.2	Coal Combustion Basics .....	5
2.3	Combustion Phases .....	5
2.4	Devolatilization Reaction Rates and Kinetics ..	7
2.5	Devolatilization Models .....	8
2.6	Volatiles Combustion .....	15
2.7	Char Combustion .....	20
2.8	Fluidized Bed Combustion of Coal .....	31
2.9	Pollutants .....	41
3.	FTIR THEORY .....	44
3.1	Origins of Theory of Light .....	44
3.2	Optical Spectroscopy .....	46
3.3	The Interferometer .....	47
3.4	Interferogram .....	50
3.5	Apodization .....	52
3.6	Resolution .....	54
3.7	FTIR Advantages .....	55
3.8	System Components .....	55
3.9	Quantum Mechanics .....	58
3.10	Calibration .....	61
4.	SPECTRAL ANALYSIS THEORY .....	66
4.1	Signal Identification .....	66
4.2	Autocorrelation Function .....	69
4.3	Power Spectral Density .....	70
4.4	The Periodogram .....	71
4.5	Pseudo-Random Binary Input .....	72
4.6	Limitations of Spectral Analysis .....	73
5.	EXPERIMENTAL APPARATUS AND METHODS .....	75
5.1	FTIR System .....	75
5.2	FTIR Calibration .....	76

5.3	Bubbling Fluidized Bed Combustor .....	79
5.4	Combustor Fuel Feeding Systems .....	82
5.5	Power Plant Sampling System .....	82
5.6	Coal Feed .....	86
5.7	Coal Tested .....	88
5.8	Data Acquisition .....	89
5.9	Data Analysis .....	92
5.10	Time Domain Analysis .....	93
5.11	Frequency Domain Analysis .....	100
6.	RESULTS .....	102
6.1	Tests in Laboratory Scale Fluidized Bed .....	102
6.3	Spectral Analysis .....	120
6.4	Pollutant Formation .....	126
7.	CONCLUSIONS .....	130
7.1	Laboratory Scale Testing .....	130
7.2	Circulating Fluidized Bed Testing .....	131
7.3	Spectral Analysis .....	133
7.4	Recommendations for Future Work .....	134
	BIBLIOGRAPHY .....	135
	APPENDIX A: QUANTIFICATION PROGRAM .....	141
	APPENDIX B: PROGRAM TO DEVELOP BODE PLOT .....	145
	APPENDIX C: UNCERTAINTY ANALYSIS .....	147

## NOMENCLATURE

a	coefficient in devolatilization rate power law (s)
a	absorptivity
a <sub>0</sub>	factor in char burnout rate constant power law (m/s)
A	pre-exponential factor in Arrhenius law (1/s)
A	devolatilization coefficient in coal combustion model= $Q\{[CO_2]_i - [CO_2]_f\} = Ng_0$
A	infrared absorbance
A	matrix of absorbances
A <sub>a</sub>	pre-exponential factor in Arrhenius law (1/s) applied to chemical rate coefficient
A <sub>i</sub>	pre-exponential factor for devolatilization of individual pseudo-species (1/s)
A <sub>b</sub>	bed area (m <sup>2</sup> )
A <sub>p</sub>	particle external surface area (m <sup>2</sup> )
b	pathlength of FTIR gas cell (m)
B	char coefficient in coal combustion model= $[CO_2]_f - [CO_2]_s = \frac{N\pi\rho_c d_i}{2\tau_c}$
c	concentration
c <sub>m</sub>	mass fraction of initial coal to be reacted
C	concentration matrix
C <sub>p</sub>	oxygen concentration in particulate phase (mol/m <sup>3</sup> )
[CO <sub>2</sub> ] <sub>A</sub>	concentration of CO <sub>2</sub> at analyzer (mol/m <sup>3</sup> )
[CO <sub>2</sub> ] <sub>f</sub>	$N(g_0 + kd_i^2[O_2]_e)/Q$ (mole/m <sup>3</sup> )
[CO <sub>2</sub> ] <sub>i</sub>	$Nkd_i^2[O_2]_e/Q$ for char coal combustion (mol/m <sup>3</sup> )
[CO <sub>2</sub> ] <sub>0</sub>	initial concentration of CO <sub>2</sub> in bed (mol/m <sup>3</sup> )
[CO <sub>2</sub> ] <sub>R</sub>	concentration of CO <sub>2</sub> exiting the reactor (mol/m <sup>3</sup> )
[CO <sub>2</sub> ] <sub>avg</sub>	average concentration of CO <sub>2</sub> in the combustor steady state background emissions (mol/m <sup>3</sup> )
d	coal particle diameter (mm)
d <sub>i</sub>	initial coal particle diameter (mm)

$d_f$	diameter of spherical fragment following primary fragmentation (mm)
$D$	effective coefficient of molecular diffusion of oxygen in the flue gas
$D_a$	general bulk diffusion coefficient of species a ( $m^2/s$ )
$D_b$	bed diameter (m)
$D_e$	intraparticle diffusion coefficient ( $m^2/s$ )
$D_G$	molecular diffusion coefficient in gas phase
$D_m$	diffusivity of oxygen to the coal particle ( $m^2/s$ )
$D_{AB}$	binary diffusion coefficient of A in B ( $m^2/s$ )
$E$	activation energy (cal/mol)
$E_a$	apparent activation energy for the combustion of char (cal/mol)
$E_i$	activation energy for volatiles release for individual species i (cal/mol)
$E_O$	mean activation energy (cal/mol)
$E_V$	overall activation energy for volatiles release (cal/mol)
$\mathcal{F}$	Fourier transform operator
$g(t)$	dynamic system transfer function
$g_O$	rate of production of $CO_2$ from combustion of volatiles (mol/s/particle)
$h$	a convective heat transfer coefficient
$h_m$	mass flux of oxygen per unit area of surface per unit of concentration difference
$H$	fluidized bed height (m)
$\Delta H$	standard enthalpy of formation ( $kJ/kg^\circ C$ )
$I_S$	infrared energy through a sample
$I_B$	intensity of the infrared energy without the sample in place
$k$	overall char reaction rate constant (m/s)
$k_1$	rate constant for first parallel reaction (1/s)

$k_2$	rate constant for second parallel reaction (1/s)
$k_C$	overall mass transfer coefficient for the reactive volatiles
$k_d$	diffusion rate of gas to particle surface ( $\text{kg(C)}/(\text{m}^2 \text{ kPa s})$ )
$k_g$	gas thermal conductivity
$k_i$	volatiles pseudo-species rate constant (1/s)
$k_V$	volatiles release rate constant (1/s)
$k_O$	surface reaction rate constant for char burnout (m/s)
$k_V$	general intrinsic reaction rate constant (1/s)
$K$	dynamic system gain
$K$	absorptivity matrix,
$L$	bed depth (m)
$m$	mass of carbon in particle or batch (g, kg)
$m$	constant heating rate (deg/s) used in devolatilization rate equation
$m_C$	cumulative carbon reacted during batch test (g, kg)
$m_{\text{coal}}$	mass of coal batched in the fluidized bed (g)
$m_i$	initial mass of carbon in char particle (g)
$m_t$	total amount of carbon in batch dump (g, kg)
$M$	molecular weight of diffusing species (g/mol)
$M_C$	molecular weight of carbon (g/mol)
$n$	exponent in char burnout time power law
$n$	apparent reaction order
$n$	oxygen transfer rate to one particle
$n(t)$	white noise input function
$N$	number of coal particles in bed
$\dot{N}$	molar flow of oxygen to a single coal particle (mol/s)
$N_f$	number of spherical fragments following primary fragmentation
$[O_2]_e$	oxygen concentration in emulsion phase of fluidized bed ( $\text{mol}/\text{m}^3$ )

$[O_2]_i$	oxygen concentration at fluidized bed inlet ( $\text{mol/m}^3$ )
$p_g$	partial pressure of oxygen in the bulk gas
$p_s$	partial pressure of oxygen on the coal particle surface
$Pr$	Prandtl number
$q$	mass of carbon oxidized per unit area of particle outer surface per second, ( $\text{kg/m}^2\text{s}$ ),
$Q$	volumetric flow rate exiting the combustor ( $\text{m}^3/\text{s}$ )
$Q$	heat generation rate in fluidized bed combustion
$Q_b$	total gas exchange rate from each bubble
$R$	universal gas constant, $8.314 \text{ kJ}/(\text{kg K})$ , $1.9872 \text{ cal}/\text{deg mole}$
$Re$	Reynolds number $=Ud_p/\mu$
$R_{yy}$	autocorrelation function
$Sc$	Schmidt number $=\mu/\rho D_g$
$Sh$	Sherwood number
$S_{yy}$	power spectral density of input function
$S_{xx}$	power spectral density of output function
$t$	time (s)
$t_b$	char burnout time (s)
$t_c$	char burnout time, chemical kinetics control (s)
$t_d$	char burnout time, diffusion control (s)
$t_o$	initial time associated with the instrument lag response (s)
$t_v$	total devolatilization time (s)
$T$	temperature (K)
$T$	infrared energy transmittance in an FTIR
$T_b$	bed temperature (K)
$T_f$	characteristic frequency of dynamic system
$T_m$	boundary layer temperature (K)
$T_p$	particle temperature (K)
$u$	superficial bed velocity (m/s)
$u(t)$	input function to a dynamic function

$u_a$	bubble velocity (m/s)
$u_o$	minimum fluidization velocity (m/s)
$v$	devolatilization power law exponent
$V$	fraction of volatiles released from coal particles
$V_b$	bubble volume
$V_i$	volatiles pseudo-species fraction
$V^*$	maximum volatiles fraction released from coal particles
$V_b$	bed volume ( $m^3$ )
$V_{nr}^*$	the potential ultimate yield of the non-reactive volatiles
$V_r^*$	actual ultimate yield
$V_r^*$	potential ultimate yield of the reactive volatiles
$V_{\infty,1}$	fraction of volatiles released from coal particles for first parallel reaction
$V_{\infty,2}$	fraction of volatiles released from coal particles for second parallel reaction
$X$	cross flow factor, $=Q_b H / u_a V_b$
$y(t)$	dynamic system response function

#### Greek Symbols

$\alpha$	coefficient in devolatilization rate power law for a fluidized bed (s)
$\delta$	Dirac delta function
$\epsilon_p$	particle void
$\epsilon_p$	particle emissivity
$v$	exponent in devolatilization rate power law
$\rho_c$	density of char particle ( $g/m^3$ )
$\rho_{p0}$	original particle density
$\sigma$	standard deviation
$\sigma$	Stefan-Boltzmann radiation constant
$\tau_c$	characteristic char burnout time (s)

$\tau_i$	contribution of interphase mass transfer of $O_2$ between bubble and emulsion phase to the characteristic char burnout time (s)
$\tau_v$	characteristic volatiles release time (s)
$\Phi$	mechanism factor in char combustion rate constant
$\omega$	frequency
$\Omega$	$u-(u-u_0)\exp(-X)$

**ACKNOWLEDGMENTS**

I want to thank Dr. Robert Brown for his guidance, wisdom, and the opportunity to embark on this research. I greatly appreciated that he gave me enough guidance to accomplish the research, but gave me freedom to work on my own. I also thank Dr. Turgut Sarpkaya, my friend and mentor, for his encouragement and advice.

This research would not have been possible without the assistance and support of Mr. Jeff Witt and the staff at the Iowa State University heating plant. Their help in installing the FTIR equipment and operating the plant during tests is greatly appreciated. The assistance of Mr. Jim Pollard of Ames Laboratory in preparing coal and sharing his knowledge of coal preparation is appreciated.

Most of all I wish to thank my family for putting up with my long hours and absences while doing this work. I could not have done this without their support

Funding for this work was partially provided by The U. S. Department of Energy through Cooperative Agreement No. DE-FC21-91MC28081.

## 1. INTRODUCTION

The detailed design of a fluidized bed boiler is partially dependent on the fuel (coal) characteristics, especially char burnout time. Characterization of coals is widely performed in bench-top laboratory scale reactors or, to a lesser degree, in pilot plant testing.

The design of fluidized bed combustors should be matched with the characteristics of the fuel and additives [65]. Optimal combustion efficiency,  $\text{SO}_2$  and  $\text{NO}_x$  emission levels, and the amount and composition of solid residues depend on the coal type and the combustion conditions. Combustion efficiency is mainly related to the combustion process of the char particles, as the volatiles combustion is considered to proceed to completion [65].

The combustion of coal, whether in pulverized state or in a fluidized bed combustor, consists of two dominant processes: volatile evolution and combustion and char combustion. When coal is heated, light hydrocarbons and carbon monoxide, the volatiles, are given off and combusted fairly rapidly. While the details of volatiles release and combustion are not well known, the process can be approximated as a first-order chemical reaction. This reaction can be modeled as an exponential decay process of the  $\text{CO}_2$  produced for small perturbations in temperature.

The remaining carbon-rich residue, char, burns much more slowly than the volatiles. The char combustion process is better understood than that of volatiles. It can be shown that for short time periods this process can also be modeled as an exponential decay in the  $\text{CO}_2$  produced.

Most coal combustion research has been conducted in laboratory scale combustors, some as small as 5 cm diameter, using only 1 (or a few), coal particles with initial diameters

from 295  $\mu\text{m}$  to 20 mm [25,27,52]. Although some coal combustion research has been conducted in industrial-scale boilers, most of that work is related to identifying the gas species present in the flue gas for purposes of studying combustion efficiency or pollution control [3,60,46]. There is some question how well the combustion models and parameters identified in a pulverized coal combustion regime or in small, bubbling fluidized bed laboratory-scale reactors apply to industrial-scale circulating fluidized bed boilers.

The operating parameters of a circulating fluidized bed combustor are quite different from a bubbling bed. Compared to a bubbling bed combustor, in a circulating bed the voidage is much higher, the superficial velocity is higher, the two phase theory of fluidization does not apply as there is no distinct bubble phase, combustion air enters the CFB in multiple stages, and the heat transfer coefficient for particles is less. Since very little research has been done in circulating fluidized bed combustors, how much difference these parameters make is not certain.

Fourier transform spectroscopy (FTS) is the technique of determining a spectrum by the explicit application of a Fourier transform to the output of an optical device, normally a two-beam interferometer. A Fourier transform infrared (FTIR) spectrometer was chosen for this research because of its ability to simultaneously identify and quantify multiple gas species in boiler flue gas. Commonly used gas analysis instruments (non-dispersive infrared (NDIR) or chemiluminescent) are limited to one gas species for each instrument and performance can be affected by unidentified gas species, such as methane or water vapor affecting  $\text{SO}_2$ . Not only can an FTIR overcome these obstacles, but additional gases can be quantified by simply developing a new quantification method for the additional gas.

Fourier transform infrared spectroscopy has the capability of simultaneously obtaining data on gas concentration, temperature, and particle size [3,60,46]. With a 10 m multipass cell the minimum detection level can be less than 1 part per million.

Many researchers have determined devolatilization and char burnout times from the visible flame of burning particles [52, 14]. A new method of determining these times based on the spectral analysis of the transient CO<sub>2</sub> emissions of a batch of coal into an operating boiler is presented. This method eliminates the reliance upon visibility of a flame and is applicable for signals possessing a small amount of random noise.

An impulse perturbation to the steady state combustion process was simulated by rapidly dumping a batch of known weight of coal into the coal feeder. This perturbation resulted in a sharp increase in CO<sub>2</sub> emissions, followed by a fast exponential decay during devolatilization and a slower exponential decay during char burnout.

Analysis of the data was conducted in both time domain and frequency domain. In the time domain, the devolatilization and char time constants were calculated assuming the CO<sub>2</sub> responses were exponential decays. In the frequency domain, the time constants were determined from cornering frequencies of a Bode plot where the devolatilization and char burnout were modeled as first order processes occurring simultaneously.

Major objectives of this investigation included: determination of the amount of modulated fuel compared to the steady-state fuel feed, development of spectral analysis as a method for characterizing fluidized bed combustor fuels, and comparison of coal characterization in a full-scale boiler to a laboratory-scale combustor.

## 2. COAL COMBUSTION THEORY

Coal has long been used throughout the world as a fuel. It is widely available, fairly easily mined in many cases, easily transported, quite safe in handling, economical in many applications in comparison with other fuels, and has a good heating value.

The world's estimated supply of economically recoverable coal is 750 billion tons. The former Soviet Union, the United States, and China together have 87% of the world's coal [46]. Canada, West Germany, Australia, and Great Britain collectively have another 10%.

### 2.1 Composition of Coal

Coal is composed primarily of carbon, hydrogen, oxygen, small amounts of nitrogen and sulfur, moisture, and inorganic minerals, called ash, left after burning. It is not of uniform composition, but an aggregate of microscopically distinguishable, physically distinctive, and chemically different substances.

Because of the wide range of composition and properties, some kind of classification system is required to bring a sense of order to the description of coal. Coal is classified on the basis of rank, which indicates how properties may vary, amount of carbon in the coal, and geological maturity. Rank assigns the position of a particular kind of coal in the progression from the original plant matter to carbon. In general, as rank increases carbon content increases, heating value increases, and oxygen content decreases.

In the United States, the American Society for Testing and Materials (ASTM) has developed a system for classification of coal into ranks. The ranks of coal, in increasing order, are lignite, subbituminous, bituminous, and anthracite [7,46].

## 2.2 Coal Combustion Basics

As might be expected for a complex substance like coal, the combustion process is also complex. The number of substances in coal, the percentage of these substances, and the rank of the coal all contribute to varying combustion rates and kinetics. The combustion of coal in any system is primarily a matter of combustion of carbon, with combustion of volatiles proceeding sequentially prior to or parallel to the carbon combustion [26]. The fundamentals of coal combustion involve the reaction kinetics of both the carbon and the volatiles. The exact composition and combustion processes of the volatiles is not well understood, partially because the volatiles content and composition vary so much from one type of coal to another. Coal combustion is influenced by coal rank, particle size, and combustion temperature.

Coal is burned in three different forms: as lumps on a grate or in a shaft; crushed and burned in a fluidized bed; or pulverized and burned in a dilute suspension [26]. Coal particle sizes in combustion range from less than 100 $\mu$ m in the pulverized size to 5 to 50 mm in a fixed or broken bed.

Coal is a charring or pyrolyzing solid in that it is distilled when heated [40]. The volatile gases emitted in the interior of the solid diffuse out of the solid and burn with air in much the same way as liquid fuel vapors. The problem of combustion of pyrolyzing solids requires a detailed understanding of both the internal (solid phase) and the external (gas phase) energy and species conservation [40].

## 2.3 Combustion Phases

The coal combustion process occurs in three phases: drying, generation of volatiles, and combustion of volatiles and char [54,66]. Devolatilization is the release of volatile matter (carbon, pyrolysis water, hydrocarbons, and hydrogen)

by thermal or chemical decomposition [54,66]. Saxena [54] states there is much evidence which supports the hypothesis that devolatilization of coal is a chemical decomposition reaction. The final products of devolatilization are a carbon-rich residue (char) and a more hydrogen-rich volatile fraction [26]. Coal is always hydrogen starved in the sense that its empirical formula is usually  $\text{CH}_{0.6}$  to  $\text{CH}$  while the desired products are in the range  $\text{CH}$  to  $\text{CH}_4$  [26]. The evolved volatiles may combust on the surface of or in the vicinity of the particle, or both. Pyrolysis is devolatilization carried out under inert conditions [54].

The volatile component of coal can account for as much as 50% of the heating value, by weight [51,54]. Devolatilization in small particles (less than  $50\mu\text{m}$ ) is isothermal and usually controlled by chemical kinetics. Heat and mass transfer resistances make the devolatilization of large particles (greater than  $100\mu\text{m}$ ) significantly different.

As coal is introduced into a hot furnace or fluidized bed, it begins to heat up and the three phases of combustion take place [35,54]. The drying phase of coal, where moisture is driven off, occurs below 373 K. The release of occluded gases, such as  $\text{CO}_2$  and methane, is almost complete by 473 K. In the temperature range 473-773 K, the organic sulfur compounds decompose, with hydrogen sulfide and certain organic sulfur compounds being evolved. The evolution of hydrogen usually begins around 673-773 K. A 'critical point' occurs about 973 K, characterized by a sharp and rapid evolution of hydrogen and carbon monoxide. In general, as the temperature of the furnace or fluidized bed increases, the amounts of hydrogen, carbon monoxide, methane and nitrogen evolved increase, while the evolution of more complex hydrocarbons decreases. The expulsion of oils begins at about 573-673 K, the yield of tar usually increasing to a maximum about 773-823 K.

Devolatilization is a finite rate chemical kinetic process, which leaves a char layer near the surface as it continues [42]. The gaseous products of devolatilization are expelled out first through the partially devolatilized solid and then through the char. This outward gas flow in the direction of the increasing temperature introduces convection, which opposes the inward solid phase heat conduction.

#### 2.4 Devolatilization Reaction Rates and Kinetics

The devolatilization process above 673 K involves energy input to break the C-C bonds in the coal. Cracking of bridges between ring systems results in the formation of free radical groups such as  $-\text{CH}_2$ ,  $-\text{O}$ -, and other larger radicals. These free radicals are highly reactive and combine in the gas phase to produce aliphatics (mainly methane) and water which diffuse out of the coal particle. Formation of methane and CO occurs at higher temperatures and results from cleavage of methyl groups split off from aromatic rings, cleavage of biaryl-ethers, and rearrangements of the resulting aryl-oxy radicals [59]. Letting R represent a radical obtained from hydrocarbons, such as benzene, naphthalene, or phenanthrene, the following typical reactions take place in stages as the temperature is increased [54]:

Cracking:



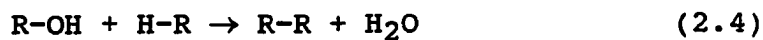
Saturation:



Tar Production:



Condensation Reaction:



Additionally, oxides of carbon are produced by the following reaction:



The hydrogen partly produces hydrocarbons and partly liberates as molecular hydrogen.

According to Essenhigh [26] there has been very little study of volatile kinetics.

### 2.5 Devolatilization Models

Instead of using actual chemical structures and elementary reactions, it is assumed that coal decomposes thermally as if it is a mixture of many components, each of which decomposes independently by a first order reaction [54,33]. Since the composition of the volatiles is so variable, and strongly dependent on the parent coal, the evolved matter is lumped into a single component, total volatiles. A large number of independent chemical decomposition reactions produce the primary volatile species. Differing chemical bond strengths cause drastic differences in the temperatures at which various bonds rupture. There are two phenomenological models used to describe devolatilization: independent reaction model and competing reaction model.

### 2.5.1 Independent reaction models

2.5.1.1 Single reaction model      The simplest description of the devolatilization reaction approximates the complex decomposition and transport phenomena as a first order reaction for total weight loss of the volatiles occurring uniformly in the particle [1,33,35,54]:

$$dV/dt = k_v(V^* - V) \quad (2.7)$$

where  $V$  is the total mass of volatiles evolved up to time  $t$  and  $V^*$  represents both the ultimate yield of volatiles as time  $t \rightarrow \infty$  and the effective volatile content of coal. The rate constant  $k_v$  is usually expressed as an Arrhenius relationship:

$$k_v = A \exp(-E/RT) \quad (2.8)$$

where  $E$  is the apparent activation energy,  $R$  is the gas constant, and  $T$  is the absolute temperature. The values  $k_v$  and  $V^*$  are determined experimentally. The ultimate volatiles yield  $V^*$  is temperature dependent and increases with temperature [1,54]. There is a lesser dependence on heating rate, pressure, and particle size [1,14,59]. Wall [67] states secondary reactions are responsible for the variations in yield.

According to Howard [33], there is little agreement on the observed rates of pyrolysis, with the discrepancy being several orders of magnitude at a given temperature. Some, but not all, of the disagreement can be attributed to coal type. Differences in equipment and experimental procedures are also likely important.

If the heating rate is held at a constant rate  $m$  (Eq. 2.9) [15,54]:

$$m = \frac{dT}{dt} \quad (2.9)$$

Eq. 2.7, 2.8, and 2.9 can be combined to give:

$$\int_0^V \frac{dV}{V^* - V} = \int_0^T \frac{A}{m} \exp(-E / RT) dT \quad (2.10)$$

Assuming  $E/RT \gg 1$  for pyrolysis reactions [33], Eq. 2.10 is integrated [33,54] to give the volatile weight loss as:

$$\frac{V^* - V}{V^*} = \exp \left[ - \frac{ART^2}{mE} \exp \left( - \frac{E}{RT} \right) \right]. \quad (2.11)$$

Equation 2.11 requires the use of three experimentally determined parameters,  $E$ ,  $V^*$ , and  $A$ .

This model does have some limitations [54]. Particularly, researchers have shown that the value of the apparent yield  $V^*$  is a function of, and increases with, temperature. The values of  $k_v$  and  $E$  are different for each set of experimental conditions [1]. Consequently, devolatilization can be more accurately represented by a number of parallel independent first order reactions with different activation energies. This forms the basis for the multireaction model.

In general, the single reaction models are still widely used to describe devolatilization kinetics due to their simplicity and mathematical tractability, despite limitations.

2.5.1.2 Multireaction models based on total volatiles  
[33,54] Multireaction models are based on the assumption that coal decomposes thermally as if it were a mixture of many pseudospecies  $V_i$ , each of which decomposes via an independent, irreversible, first order reaction as a result of differences

in chemical bond strengths, and with a characteristic energy [33,35,54]:

$$dV_i/dt = k_i(V_i^* - V_i) \quad (2.12)$$

The Arrhenius factor for all reactions is:

$$k_i = A \exp(-E/RT). \quad (2.13)$$

The activation energy  $E$  can be approximated as a continuous distribution function  $f(E)$ , with  $f(E)dE$  being the fraction of potential volatiles having an activation energy between  $E$  and  $E + dE$ . For all the volatiles:

$$dV^* = V^* f(E) dE. \quad (2.14)$$

Combining Eq. 2.12, 2.13, and 2.14 gives [33,54]:

$$\frac{V^* - V}{V^*} = \int_0^{\infty} \exp[-At \exp(-E/RT)] f(E) dE. \quad (2.15)$$

A Gaussian distribution for the activation energy density function  $f(E)$  has been proposed by Saxena [54] and Howard[33]:

$$f(E) = \frac{1}{\sigma \sqrt{2\pi}} \exp \left[ -\frac{(E - E_0)^2}{2\sigma^2} \right] \quad (2.16)$$

where  $E_0$  is the mean activation energy and  $\sigma$  is the standard deviation. Integrating Eq. 2.12 yields:

$$\frac{V_i^* - V_i}{V_i^*} = \exp \left( -\int_0^t k_i dt \right). \quad (2.17)$$

For total volatiles:

$$\begin{aligned} \frac{v^* - v}{v^*} &= \int_0^{\infty} \exp\left(-\int_0^t k_i dt\right) f(E) dE \\ &= \int_0^{\infty} \exp\left[-A \int_0^t \exp(-E / RT) dt\right] f(E) dE. \end{aligned} \quad (2.18)$$

Equation 2.18 is applicable to a nonisothermal process, eliminating the temperature dependence of  $v^*$ , and reduces to Eq. 2.11 for an isothermal process. The four parameters ( $E$ ,  $v^*$ ,  $\sigma$ , and  $A$ ) which describe the process are only one more than needed for the single reaction model (Eq. 2.11) and are determined experimentally. Eliminating the temperature dependence of  $v^*$  allows data on a given coal to be correlated with one set of values under different sets of experimental conditions [15]. However, per Howard [33], the physical meaning of Eq. 2.18 is difficult to visualize and it is not widely used.

2.5.1.3 Multi-reaction models based on the individual components [33] An alternative approach applies the first order model to each of the volatile components and assumes that the devolatilizing coal may follow any of a number of reaction paths:

$$\frac{dv_i}{dt} = -A_i \exp(-E_i / RT) [v_i^* - v]. \quad (2.19)$$

In this equation  $i$  represents the volatile species. Components like  $\text{CO}_2$  and  $\text{CO}$  evolve in steps and cannot be described by a single reaction, but may require up to three parallel reactions depending on the observed weight loss. If each volatile component is represented by a Gaussian

distribution in the activation energy, the most sophisticated kinetic model for coal pyrolysis is obtained.

A simple model for two competing overall parallel reactions is [66]:

$$dV/dt = (k_1V_{\infty,1} + k_2V_{\infty,2})c_m \quad (2.20)$$

where  $c_m$  is the mass fraction of initial coal to be reacted. The rate constants  $k_1$  and  $k_2$  are of the Arrhenius form with  $E_1$  less than  $E_2$ . The total volatile yields are  $V_{\infty,1}$  and  $V_{\infty,2}$ . The overall volatiles yield is given by

$$V = \int_0^t (k_1V_{\infty,1} + k_2V_{\infty,2}) \exp\left[-\int_0^{t'} (k_1 + k_2) dt''\right] dt'. \quad (2.21)$$

The two step model appears to be the most realistic for combustion applications at present [54].

Per Anthony, et al. [1] the multi-reaction model offers an explanation for the low activation energies commonly encountered when using a single first-order reaction. Junk [39] compared single reaction and multireaction response models, and found the impulse response could be described as an exponential decay, regardless of model employed.

### 2.5.2 Competing reaction models

In competing reaction models the coal is assumed to decompose via one of several possible reaction paths depending on the time-temperature history [1,33,54]. Mass transfer of volatiles generated in the interior of the coal particle to the exterior surface may result in interaction with the char and secondary reactions [54].

The phenomena of mass transfer and secondary reactions are coupled and must be analyzed together. Saxena [54] states

the mass transfer process plays an important role in determining the volatile yield during pyrolysis. The secondary reactions are primarily concerned with the heavy tar molecules produced during devolatilization [54].

Tar production decreases with increased pressure and increased particle size [54]. The extent of secondary reactions is influenced by the residence time and concentration of reactive species in contact with hot surfaces [33].

A simple lumped model incorporating secondary reactions has been developed which assumes isothermal conditions and uniform concentration of the reactive species [1,33,54]. The total volatile yield,  $V^*$ , is expressed as the sum of two parts, the non-reactive ( $V_{nr}^*$ ) and the reactive ( $V_R^*$ ) parts:

$$V^* = V_{nr}^* + V_R^*. \quad (2.22)$$

In calculating the reactive part, the coupled mass transfer kinetics have to be analyzed. Mass balance for the reactive species gives:

$$V_R^* = \frac{V_{R}^{**}}{[1 + (k_i / k_C)]}. \quad (2.23)$$

$V_{R}^{**}$  is the potential ultimate yield of the reactive volatiles while  $V_R^*$  is the actual ultimate yield,  $k_i$  is the reaction rate constant for the deposition reaction, and  $k_C$  is the overall mass transfer coefficient for the reactive volatiles. The mass transfer coefficient is assumed to be proportional to the diffusion coefficient of the volatiles [33]. The ultimate yield is also a function of pressure.

Presently, the relative extent of cracking and polymerization reaction is not known and the chemistry of the

secondary reactions is not established. The nature of secondary reactions is strongly influenced by residence time and concentration of reactive species in contact with hot surfaces [1]. The escape of volatiles is a complex process involving time-dependent pore structure and hydrodynamic flow of evolving volatiles, not simple diffusion [33]. Consequently, the secondary reactions are not amenable to exact quantitative description at this time [11], although there has been effective representation of the decomposition kinetics based on the success in correlating composition and yield data [33].

Rapid devolatilization can give yields of volatiles significantly larger than the volatile matter content obtained from proximate analysis [1]. Heating rate appears to have little effect on volatiles yield [1], but yield increases significantly with decreased particle or sample size.

## 2.6 Volatiles Combustion

For small particles (less than 65  $\mu\text{m}$ ) the flame front of the evolved volatile matter has been observed at the coal surface. In this case, oxygen diffusion to the surface exceeds that required for the consumption of volatiles. In larger particles, the flame is evident at a distance from the surface, i.e., not attached to it.

In general, it appears that volatile matter is evolved into the turbulent free stream, where it burns remotely from the char. Essenhigh [25] observed that the volatile evolution was vigorous, and generally channeled by the solid matrix into irregular flaming jets which issued with some force, except with the sole possible exception of anthracite. Prins, et al. [51] did not observe flames from volatiles combustion in the dense phase of a fluidized bed. The flames they observed had different appearances, depending on the location of the

particle in the bed, i.e. on the surface, in bubbles, or above the bed.

### 2.6.1 Volatiles combustion time

Essenhigh [25], Saxena [54], and others have commonly expressed the volatiles release time,  $t_v$ , as a power of the initial particle diameter,  $d_i$ :

$$t_v = a d_i^v \quad (2.24)$$

For spherical particles, theory provides  $v$  is equal to 2 [25]. Essenhigh's experiments [25] found general agreement with this. For particles in the range of .3 to 5 mm,  $a$  was found to equal .9 s/mm<sup>2</sup>, and  $v$  equal to 2. Ragland and Weiss [52] observed both  $a$  and  $v$  to be equal to 1.5 for particles 2 to 12 mm in diameter. Other researchers [50,51,52] have found  $v$  to vary from .3 to 1.8 depending on coal type for particles less than 8 mm.

Essenhigh [25] tested 10 coals from 3/16" to 52 mesh (295  $\mu$ m) diameter one at a time in stagnant air between two heating plates. The volatiles released from particles less than 800-1000  $\mu$ m did not ignite. He attributed this to the jet effect of the volatiles evolution, such that the volatiles were distributed throughout too large a volume and the concentration was below the lower flammability limit. He used the Eq. 2.24 power law relationship, but found  $a$  to vary from 0.4 to 1.3, with a nominal value of 0.9, and  $v$  to vary from 1.02 to 2.3. He felt the square law relationship was justified, which implied diffusion control. He also found  $t_v$  to be independent of coal rank.

Ragland and Weiss [52] studied single 2-12 mm particles in a small quartz reactor at 705 and 816°C. They tested Texas lignite, Montana sub-bituminous, and Kentucky bituminous. The

devolatilization time,  $t_v$ , was based on volatile flame extinction time and was found to be independent of coal type, and only weakly dependent on temperature. Local flow velocity was reported to be similar to interstitial velocity in a fluidized bed, but no numerical values were given. They also found that the Eq. 2.24 power law relationship described the relationship between initial particle diameter and devolatilization time. From their data, both  $a$  and  $v$  were equal to 1.5. The exponent 1.5 indicated both linear heat transfer and surface area effects were important.

Prins et al. [51] studied 4-9 mm particles of brown, bituminous, and anthracite coal in a fluidized bed. The bed particles were 0.6 mm diameter and bed temperature was varied from 220 to 850°C. An O<sub>2</sub>/N<sub>2</sub> mixture was used for fluidization. Volatiles release and combustion time was also based on visible volatile flame extinction time. They found for particles less than 1 mm diameter the devolatilization rate was controlled by chemical kinetics reactions, and  $t_v$  was independent of diameter. For particles greater than 1 mm, the devolatilization rate was controlled by heat transfer to and through the particle. For the same power law relationship as used previously, they found  $v$  equal to 1.7 for their data at 680, 750, and 850°C. They stated that  $v$  equal to 1.3 implied external heat transfer control and  $v$  equal to 2 was for large particles with internal heat transfer control. Thus, with  $v$  equal to 1.7, they found both internal and external heat transfer controlled. In the temperature range they used, they found little influence of temperature on devolatilization time. Wet particles showed longer devolatilization times than dry particles.

Pillai [50] used the same power law relationship for 6-15 mm diameter particles in a 100 mm diameter fluidized bed. His bed had a relatively low 13% O<sub>2</sub> concentration at the inlet

(compared to 21% for Prins et al. [51]) with fluidizing velocity of 1.2 m/s. The bed material was 620  $\mu\text{m}$  refractory material. Devolatilization times were obtained by observing the time for volatile flame extinction. He found  $v$  equal to 1.81 for Rufford coal and equal to 0.83 for Pittsburgh #8 coal. He concluded radiation from the bed to the coal particles might be the most predominant mechanism of heat transfer. He was uncertain of the controlling mechanism.

Integrating Eq. 2.7 with  $1/\tau_v = k_v$  (where  $\tau_v$  is a characteristic time) yields:

$$V = V^* [1 - \exp(-t/\tau_v)]. \quad (2.25)$$

This suggests that 95% of the volatiles are released within three characteristic time constants and the devolatilization time can be approximated as:

$$t_v = 3\tau_v. \quad (2.26)$$

The devolatilization time  $t_v$  is on the order of a few seconds to 20 seconds and is controlled by the evolution of volatiles [26,42,54]. Final temperature, particle heating rate, and particle size can also influence the volatiles release time. Very little is known about the mechanisms of volatiles combustion [33]. The volatiles combustion time is much faster than the evolution time, and is often assumed to be instantaneous. Thus,  $t_v$  represents the time for volatiles to evolve and combust.

### 2.6.2 Volatiles combustion model

Christofides and Brown [16] showed that a bubbling fluidized bed reactor could be treated as a continuously stirred tank reactor (CSTR) and gave the  $\text{CO}_2$  concentration exiting the overall reactor,  $[\text{CO}_2]_R$ , as a mass balance:

$$v_b \frac{d[\text{CO}_2]_R}{dt} + Q[\text{CO}_2]_R = -\frac{1}{M_c} \frac{dm}{dt} \Big|_{\text{devol.}} - \frac{1}{M_c} \frac{dm}{dt} \Big|_{\text{char}} \quad (2.27)$$

where the first term on the right hand side of Eq. 2.27 is the rate volatiles are converted to  $\text{CO}_2$  and the second term is the rate the char carbon is converted to  $\text{CO}_2$ .

Assuming carbon compounds released during devolatilization are instantaneously oxidized to  $\text{CO}_2$ , the rate of  $\text{CO}_2$  formation from volatiles can be given by the first-order model [16]:

$$-\frac{1}{M_c} \frac{dm}{dt} \Big|_{\text{devol}} = N_{g_0} \exp\left(-\frac{t}{\tau_v}\right) \quad (2.28)$$

For time  $t < 3\tau_v$ , Eq. 2.28 can be integrated and arranged to yield:

$$[\text{CO}_2]_R = [\text{CO}_2]_f + ([\text{CO}_2]_i - [\text{CO}_2]_f) \exp(-t/\tau_v) \quad (2.29)$$

where

$$[\text{CO}_2]_f = N_{d_i}^2 k [\text{O}_2]_e / Q \quad (2.30)$$

is the approximately constant contribution of char combustion to the  $\text{CO}_2$  signal during devolatilization,  $[\text{CO}_2]_i$  is the combined effect of devolatilization and char burning extrapolated to the starting time [16], and

$$N_{g_0} = Q \{ [\text{CO}_2]_i - [\text{CO}_2]_f \}. \quad (2.31)$$

The quantity  $[\text{CO}_2]_i$  is given by:

$$[\text{CO}_2]_i = \frac{N}{Q} (g_o + kd_i^2 [\text{O}_2]_e) \quad (2.32)$$

Simultaneous char and volatiles combustion is assumed for Eq. 2.29. Saxena [54] and Ragland and Weiss [52] theorize that char combustion does not begin until volatiles evolution is complete, as the oxygen cannot diffuse to the coal surface while the volatiles are being expelled. On the other hand, Christofides and Brown [16] demonstrated in their experiments in a fluidized bed that char burned simultaneously with volatiles release.

Research evidence [25,52] suggests that volatile matter burns remotely from the char and the increased gas temperature due to this combustion then accelerates the char heating.

## 2.7 Char Combustion

Char combustion is a much slower process than devolatilization (up to thousands of seconds for the largest particles) and thus controls the time for complete combustion in the furnace [54].

Char burnout time is important in predicting heat release rates and in selecting the appropriate size for a combustor [5]. Burnout time depends as much on the combustion environment as on the physical and chemical properties of coal.

Once all the volatiles are released, the carbon rich residue of a pyrolyzing solid behaves in the same manner as a simple solid [66]. The combustion of a carbon particle is accompanied by high surface temperatures at which it becomes incandescent. The burning rate of simple solids depends strongly upon the rate of oxygen diffusion to the fuel surface.

According to Kanury [40], any heterogeneous reaction involves the following five steps in series:

- (i) Oxygen diffuses to the fuel surface.
- (ii) Diffused oxygen is absorbed by the surface.
- (iii) Absorbed oxygen reacts with the solid to form absorbed products.

(iv) Absorbed products desorb from the surface.

(v) Desorbed products diffuse away from the surface.

These steps occur in series, with the slowest determining the burning rate. For carbon combustion, steps (ii) and (iv) are known to be extremely fast. When the particle temperature is low, the particle is small, and the air velocity around it is slow, step (iii) is known to be much slower than step (i) or step (v), and the burning rate is controlled by chemical kinetics. When the particle and flow velocity are both large and temperature is high, step (iii) is much faster than steps (i) and (v) and the burning rate is then controlled by the diffusion rate of oxygen to the particle.

A widely used model of char combustion, called the two film theory, consists of a porous spherical char particle surrounded by a stagnant boundary layer through which oxygen must diffuse before it reacts with the char (Fig. 2.1).

Avedesian and Davidson [2] developed the two film model to explain why the burnout time,  $t_c$ , for large coal particles was proportional to the square of the particle diameter. This model assumes that all chemical reactions are very fast and the oxygen diffuses from the free stream to the particle where it reacts to form CO. The CO diffuses away from the particle and reacts with the incoming  $O_2$  to form  $CO_2$ , part of which diffuses back to the particle where it reacts to form CO, the rest diffusing to the free stream. Avedesian and Davidson [2] stated that, for particles greater than 100  $\mu m$ , the diffusion is slow in comparison to surface reaction, and that no CO is expected to escape to the free stream, as long as adequate oxygen is present.

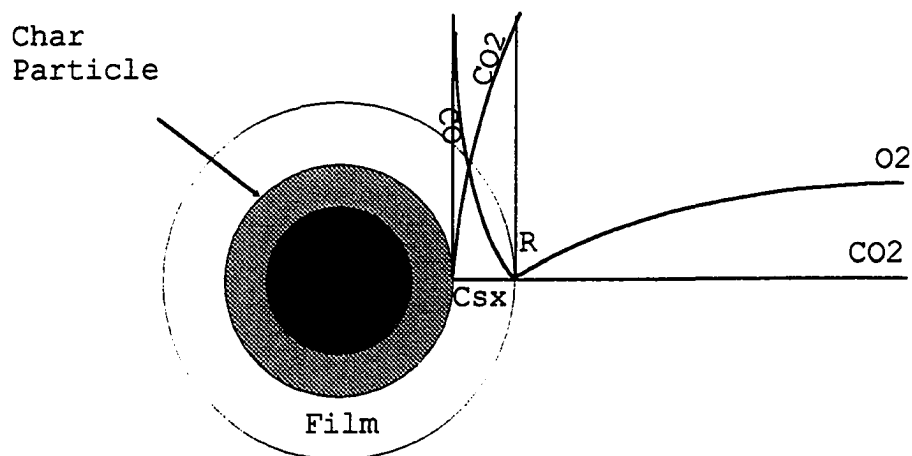
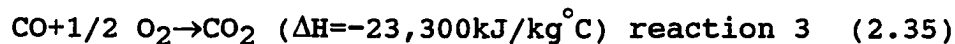


Figure 2.1. Two film model

The products of combustion between char and oxygen are CO and CO<sub>2</sub>, as represented by the following reactions [54,66]:



These reactions are exothermic and may result in the temperature of the char exceeding that of the free stream. Measured values of temperature difference are consistent with calculated differences taking combustion to CO (reaction 1) with subsequent oxidation of CO to CO<sub>2</sub> in the free stream:



Ross and Davidson [53] improved on the two film model to include the effects of chemical reaction time on burnout time. They studied 3 models for carbon and oxygen reactions of a

char particle in a fluidized bed. Model 1, a modification of the two film model, assumed the surface reaction (Eq. 2.36) occurred at a finite rate so there was a finite surface concentration of  $\text{CO}_2$ . Model 2 assumed the rate of reduction of  $\text{CO}_2$  by carbon was negligible. Reaction 3 (Eq. 2.35) was assumed to be rapid and reaction 2 (Eq. 2.34) was the overall effective reaction. Model 3 was the same as model 2, but with a slow rate for reaction 3 (Eq. 2.35). They found a process between the models 2 and 3 to be most representative of actual conditions.

Hayhurst [31] concluded CO does not burn in the interstices between bed particles in a bubbling fluidized bed, but in the bubbles or on top of the bed.

For a single char particle with conservation of oxygen in the boundary layer, the mass of carbon oxidized per unit area of particle outer surface per second,  $q$  ( $\text{kg}/\text{m}^2\text{s}$ ), can be expressed as [5,35,58,67]:

$$q = k_d(p_g - p_s) \quad (2.37)$$

Where  $p_g$  is the partial pressure of oxygen in the bulk gas,  $p_s$  is the partial pressure of oxygen on the surface, and the diffusion rate  $k_d$  ( $\text{kg}/(\text{m}^2 \text{kPa s})$ ) is constant, and is represented as:

$$k_d = \frac{12 \Phi \text{Sh} D}{d R T_m} \quad (2.38)$$

The mechanism factor  $\Phi$  equals 1 for reaction to  $\text{CO}_2$  and 2 for reaction to CO,  $D$  is the effective coefficient of molecular diffusion of oxygen in the flue gas,  $d$  is the particle diameter,  $T_m$  is the boundary layer temperature (K), 12 is the molecular weight of carbon, and  $R$  is the universal

gas constant. For a small spherical particle with small velocity  $Sh=2$ .

Basu [5] and Wall [67] describe three combustion regimes, based on whether char combustion takes place inside the pores, or on the external surface. These three regimes also depend upon the combustor operating condition. In regime I, the chemical kinetic rate is much slower than the diffusion rate, and the reaction would occur on the exterior surface of coarse non porous particles at temperatures about  $900^{\circ}C$ . The temperature is lower for porous chars. This regime typically occurs during CFB start-up when the temperature is low, and with fine particles. In regime II, the chemical reaction rate and pore diffusion rate are comparable. This occurs for medium size char. Regime III occurs when the mass transfer rate is very slow compared to the chemical reaction rate. This is referred to as diffusion-controlled combustion.

When the surface reaction rate is very high (regime III), the oxygen concentration at the surface,  $p_s$ , approaches zero, and Eq. 2.37 gives the maximum burning rate for external diffusion [5,35,58,67]:

$$q=k_d p_g \quad (2.39)$$

This is the diffusion-limiting case.

When the surface reaction is limiting (regime I), the reaction rate is given by:

$$q=k_c p_s \quad (2.40)$$

for a first order reaction; where  $k_c$  is the chemical reaction rate coefficient based on the external surface area of the char. For a limited temperature range [35,67]:

$$k_C = A_a \exp(-E_a/RT_p). \quad (2.41)$$

where  $A_a$  is the pre-exponential factor,  $E_a$  is the activation energy for regime II combustion, and  $T_p$  is the particle temperature.

For regime II, when the apparent reaction is  $n$ th order, and both surface reaction and diffusion control, the specific burning rate,  $q$ , can be expressed in the following more general semi-empirical formulation:

$$q = k_C p_S^n \quad (2.42)$$

where  $k_C$  is the reaction rate of carbon based on the external surface area of the char. Eliminating the surface concentration of oxygen,  $p_S$ , from equations 2.37 and 2.42, the reaction rate  $k_C$  can be expressed as [5,35]:

$$k_C = \frac{q}{(p_g - q/k_d)^n} \quad (2.43)$$

For a first-order reaction ( $n=1$ ) the burning rate can be simplified as:

$$q = \frac{p_g}{1/k_d + 1/k_C} \quad (2.44)$$

Char burnout is influenced by porosity, with the result that the particles may burn in one of two extreme modes, or at an intermediate point [26]. One extreme is reaction at the exterior surface, so that the particles shrink in diameter but maintain constant density. The other extreme is reaction at all the internal surfaces of the porous particle, at constant diameter but decreasing density. Experimental evidence

supports both the extreme models and the intermediate behavior at different conditions of reaction. Additionally, large particles have reactions that are modified by diffusional boundary layers [26].

### 2.7.1 Char burning times

Burning times of char particles in unchanging oxygen atmospheres can be considered to be the result of diffusion control (constant density, shrinking diameter or constant diameter) or chemical kinetics control and are functions of particle diameter.

The burning time for diffusion control (regime III) [26,35,67], constant density is

$$t_b = \frac{\rho_{p0}RT_m}{96\Phi D p_g} d_i^2 \quad (2.45)$$

where  $d_i$  is the original particle diameter,  $\rho_{p0}$  is the original particle density and  $Sh = 2$ .

If the particle is assumed to burn internally with constant diameter, decreasing density, which is unlikely for diffusion control, then [67]:

$$t_b = \frac{\rho_{p0}RT_m}{144\Phi D p_g} d_i^2. \quad (2.46)$$

The burning time obtained assuming constant size during combustion is 2/3 of the time obtained assuming constant density [26,67].

For chemical kinetics control (regime I) with the particle burning at constant density, the burning time is [67]:

$$t_{bc} = \frac{\rho_{p0}}{2k_c \rho_g} d_i \quad (2.47)$$

and for burning at constant diameter

$$t_{bd} = \frac{\rho_{p0}}{6k_c \rho_g} d_i. \quad (2.48)$$

For the general case of mixed control the burning time  $t_b$  for combustion at constant density is [67]

$$t_b = t_{bc} + t_{bd}. \quad (2.49)$$

From the above it is seen that char burning time is proportional to  $d_i$  for chemical kinetics control and to  $d_i^2$  for diffusion control. Avedesian and Davidson [2] found that chemical kinetics at the particle surface did not control the combustion of large char particles because the char burnout time was independent of mass of coal charge, and the burnout time was proportional to  $d_i^2$ .

### 2.7.2 Burning rate of single char particle

LaNauze [42] summarized the work of various authors who studied burning rates of coal. Most of them investigated the burning rate of single coal particles in fluidized beds. Chakraborty and Howard [11] developed expressions for the burning rates of single carbon particles. They showed the burning rate was proportional to  $d_i^n$ , where  $n$  is 1 for diffusion control and 2 for chemical kinetic control.

Basu [33] studied the burning of 9-15 mm electrode-carbon spheres in a 150 mm fluidized bed of 100  $\mu\text{m}$  sand. Individual carbon spheres were suspended in the fluidized bed and burned. At 300 second intervals the particles were removed and weighed. From this, the burning rate ( $dm/dt$ ) was estimated.

A plot of the burning rate vs. diameter showed a power law relationship, with the exponent varying between 1.22 and 1.55. He found the overall burning rate decreased as particle diameter decreased. The power law exponent is 2 for purely chemical kinetics control, while it is 1 for diffusion control. The exponent obtained indicated primarily diffusion control.

Chakraborty and Howard [13] studied char combustion in a shallow fluidized bed combustor. The char was high-volatile bituminous coals carbonized at about 420°C, 1.84-4.375 mm mean diameter. The experiments were performed at 800 and 900°C in a bed fluidized with air. The exhaust gas was analyzed for CO, CO<sub>2</sub>, and O<sub>2</sub> concentration. For particles greater than 1 mm:

$$-\frac{dm}{dt} = 12 \pi d^2 \left( \frac{1}{\frac{1}{k_g} + \frac{1}{k_s}} \right) c_p \quad (2.50)$$

with:  $k_g = \frac{ShD_G}{d} \quad (2.51)$

and  $k_s = \frac{q}{12 c_p} \quad (2.52)$

$C_p$  is oxygen concentration in the fluidizing air in the bed and  $q$  is the rate of consumption of carbon per unit area per unit time, kg/m<sup>2</sup>s. These equations were used to derive an equation for burnout time. Experiments were compared to these theoretical values.

They found the experimentally determined power law exponent to lie between 1 and 2, which indicated that both kinetics and mass transfer were important in the combustion

process. They found convective mass transfer to be more significant for the larger particles than the smaller. Resistance to oxygen flow appeared to be considerably reduced with larger diameter inert particles in the bed. Their results suggested that a constant  $Sh$  of 1.42, which had been suggested by Avedesian and Davidson [2], was inadequate to describe their data.

LaNauze and Jung [43] studied combustion of 6.7 - 13 mm dia single petroleum coke particles in an air fluidized bed of 0.66 mm diameter sand at 1173K at a fluidizing velocity of 0.536 m/s. The bed diameter was 102 mm, with static bed height of 160 mm. The coke was devolatilized before conducting the char combustion experiments. Particles were placed in a heated bed and burned and sampled at 30 and 60 s intervals to be weighed and measured. The burning rate was calculated from these measurements. Their particles followed a shrinking sphere model. They plotted reaction rate ( $\text{kg}/\text{m}^2\text{s}$ ) vs. initial diameter. On a log-log plot the data linearly decreased with increasing diameter.

Chakraborty and Howard [11] tested 3-12 mm diameter carbon spheres in a 71.5 mm dia bed, with sand particles of 327.5, 550, and 780  $\mu\text{m}$  dia at 1073 and 1173 K and fluidizing velocities of 25, 65, 27, and 71 cm/s. They put about 6 particles at a time into the heated bed, and removed them at 50-100 s intervals to weigh and measure. Burning rate was computed from mass loss. They determined attrition was negligible. Burning rates per particle ( $\text{kg}/\text{s}$ ) increased with increasing diameter and varied from 0.1-10  $\text{kg}/\text{s}$ . They found the power law exponent ranged from 1.8 to 1.97, indicating primarily chemical kinetic control. Burning rate increased with increase in size of bed inert particles, air flow rate, and bed temperature. Burning rates were 25% greater in shallow beds than in deeper beds. They found  $Sh$  ranged from 1 to 5.7, increasing with particle size, inert particle size,

and air flow rate. Carbon particles greater than about 4 mm burned significantly faster than predicted by the model, suggesting oxygen reached the surface faster than diffusion would predict.

### 2.7.3 Fragmentation

Fragmentation of coal particles can occur when they are rapidly heated. Breaking of coal particles into finer particles affects burning rates. Chirone et al. [15] describe three fragmentation phenomena: primary fragmentation, secondary fragmentation, and fragmentation by uniform percolation. Primary and secondary fragmentation break up the coal into relatively large pieces with negligible production of fines [15]. Fragmentation by uniform percolation takes place during the late stages of combustion when particle combustion is controlled by internal surface reaction [15].

In summarizing the work of other authors, Chirone et al. [15] suggest that primary fragmentation occurs as a result of internal stresses induced in the particle due to devolatilization and thermal shock within a few seconds of injection of the coal particles into the bed. Primary fragmentation is enhanced by the presence of air [44]. Prins et al. [51] and Marban et al. [44] observed that primary fragmentation strongly depends on coal type, with higher rank coals splitting into tens of smaller particles and low rank brown coal not splitting at all. Larger coal particles exhibit greater fragmentation than smaller particles. Particles less than 1 mm appear not to fragment.

Secondary fragmentation takes place during char combustion due to the breakage of weak intraparticle bridges connecting large parts of the char particle [44]. Sundback et al. [63] monitored the CO<sub>2</sub> concentration in the exhaust gases of a fluidized bed combustor and surmised the high frequency fluctuations recorded during char combustion were related to

the acceleration in the burning rate following secondary fragmentation. They observed from one to ten step increases in the CO<sub>2</sub> concentration and developed a fragmentation behavior model, addressing both fragment size and time of fragmentation. Marban et al. [44] found the degree of fragmentation increased with particle size. Dakic' [22] attributed the main reason for secondary fragmentation to the increase in coal porosity during char combustion. Uniform percolation fragmentation is the result of particle collapse and due to pore enlargement and coalescence [15]. Chirone et al. [15] stated uniform percolation was important when feeding with fine coal or with coals yielding chars with large porosity. In general, fragmentation increases the rate of attrition [44] and shortens the devolatilization time through primary fragmentation [22,62].

## 2.8 Fluidized Bed Combustion of Coal

As air is introduced to the base of a static bed of particles at an increasing rate, a point is reached at which the weight of the bed is wholly supported by the rising air. At this point the pressure drop through the bed is approximately equal to the bed weight per unit of cross-sectional area. The superficial air velocity (defined as volumetric flow rate divided by bed area) at this condition is termed the minimum fluidization velocity. The volume occupied by the bed increases abruptly and the bed as a whole exhibits many of the characteristics of a liquid [20,35].

As the air flow rate is increased still further, the velocity of the air rising through the fluidized particles, and the bulk density of most of the bed, remain more or less constant, the additional air rising as "bubbles" through the denser particulate, or emulsion, phase. This two phase behavior is an important feature of fluidized combustion beds, most of which operate in the bubbling mode. The upward

movement of bubbles through the emulsion phase results in rapid vertical mixing of the bed particles. Horizontal mixing is also induced, but it is significantly less than the vertical mixing. The vigorous bed mixing ensures the rapid distribution and transfer of heat released by combustion. A remarkable feature of fluidized bed combustors is the degree of uniformity of temperature throughout the bed.

The primary advantage of a fluidized bed combustor is the high coefficient of heat transfer between the bed and cooling surfaces immersed in it [20,35]. Fluidized bed heat transfer coefficients may be orders of magnitude greater than for a packed bed. Bed temperature may be closely controlled by immersed cooling tubes, making it possible to burn a range of coals (or other fuels) with widely differing properties efficiently and at a temperature below the ash softening point, thus reducing agglomeration. At these relatively low temperatures (750-959 K) excessive volatilization of alkali metals is reduced, production of  $\text{NO}_x$  is decreased, and sulfur removal using sorbents such as limestone or dolomite is favored.

Fluidized bed combustor operating temperatures are less than  $1000^\circ\text{C}$  for ballasted beds (inert sand as bed) or greater than  $1000^\circ\text{C}$  for unballasted beds (ash is the inert bed material) [27]. In both modes, heating rates are quite high ( $10^3$ - $10^4$   $^\circ\text{C}/\text{s}$ ), so mass lost as volatiles can be up to twice that of the ASTM volatile matter percentage.

The burning fuel particles in a fluidized bed generally comprise no more than a few per cent of the total bed mass. Heat is generated in and close to the surface of burning char particles, raising their temperatures above the mean bed temperatures. Thus, there is heat transfer from the burning particles to the inert bed particles and then to the various heat sinks. Excess temperatures of burning particles over

mean bed temperature are commonly in the range of 100-200°C. A commonly used heat balance for a burning particle at temperature  $T_p$  in a bed at temperature  $T_b$  is represented by a convective term and a radiative term [67]:

$$\dot{Q} = hA_p(T_p - T_b) + \sigma\epsilon_p A_p(T_p^4 - T_b^4) \quad (2.53)$$

where  $Q$  is the heat generation rate,  $h$  is a convective heat transfer coefficient,  $A_p$  is the particle external surface area,  $\epsilon_p$  the particle emissivity and  $\sigma$  the Stefan-Boltzmann radiation constant. Because particles close to the burning particle are likely to be hotter than the mean bed temperature, the radiation term probably over-estimates heat transfer.

The heat transfer coefficient depends on the thermal conductivity of the heat transfer medium which, for a fluidized bed, is a composite of gas surrounding the particle and inert bed material. The Nusselt number ( $Nu$ ) relates the gas thermal conductivity  $k_g$  to the heat transfer coefficient as:

$$Nu = hd/k_g. \quad (2.54)$$

Due to complex processes in a fluidized bed,  $Nu$  cannot be predicted from experience and has to be evaluated from experimental data.

Mass transfer of oxygen from the bubble phase to the coal particle in the emulsion is a significant influence in the combustion of a coal particle in a fluidized bed, and is expressed as the non-dimensional Sherwood number  $Sh$ , analogous to  $Nu$  for heat transfer. Where  $h_m$  is the mass flux of oxygen per unit area of surface per unit of concentration difference between that at the surface and that in the gas outside the

boundary layer,  $D$  is the diffusion coefficient of oxygen through the gas mixture surrounding the particle, and  $d$  is the particle diameter, the Sherwood number is

$$\text{Sh} = h_m d / D. \quad (2.55)$$

LaNauze [42] and Hoy and Gill [35] summarize the many relations developed for  $\text{Nu}$  and  $\text{Sh}$  numbers. It was found that early correlations did not take into account the resistance to mass transfer contributed by the inert bed particles, and thus  $\text{Nu}$  and  $\text{Sh}$  were over estimated. When bed voidage is taken into account, the correlations for a sphere are:

$$\text{Nu} = 2 + 0.69 \text{Re}^{1/2} \text{Pr}^{1/3} \quad (2.56)$$

$$\text{Sh} = 2\varepsilon + 0.69 (\text{Re}/\varepsilon)^{1/2} \text{Sc}^{1/3} \quad (2.57)$$

with  $\text{Re} = Ud\rho/\mu$ , Schmidt number  $\text{Sc} = \mu/\rho D_G$ , and  $\varepsilon$  is bed voidage. The Schmidt number is the ratio of momentum and mass diffusivities and is the mass transfer equivalent of the Prandtl number for heat transfer.

Devolatilization times in a fluidized bed have a relationship similar to Eq. 2.24 power law, but are slower. Hoy and Gill [35] summarize the work of various researchers, and report a relationship

$$t_v = \alpha d^n \quad (2.58)$$

where  $\alpha$  is 2-20 and  $n$  is 1.3-1.7. This yields a slower  $t_v$  than for the previous relationship, which was developed for small pulverized coal particles.

Ross and Davidson [53] developed a model for char burnout that includes the effects of chemical reaction on burnout time in a fluidized bed:

$$t_c = \frac{m_i}{12[O_2]_i A_b [u - (u - u_o)e^{-X}]} + \frac{\rho_c d_i}{24k_o [O_2]_i} + \frac{\rho_c d_i^2}{48ShD_m [O_2]_i} \quad (2.59)$$

The first term on the right hand side of Eq. 2.59 is the time associated with interphase mass transport of oxygen between the bubble and emulsion phases of the fluidized bed. The second and third terms are associated with chemical kinetics and film diffusion (constant Sherwood number) contributions to char burnout time, respectively. The cross-flow factor  $X$  represents the magnitude of the flow of gas through a bubble and out again into the particulate phase, which is the number of times a bubble is flushed out in passing through the bed. Eq. 2.59 indicates that both chemical kinetics and mass transfer influence char burning time in a fluidized bed. If the reaction is chemical kinetic controlled, then the burning time  $t_c$  is proportional to  $d_i$ . The burning time is proportional to  $d_i^2$  if the burning is reaction is diffusion controlled.

Basu and Halder [6] found particles exhibited low burning rates when they were at the bottom of a circulating fluidized bed, as compared to a bubbling bed. This was believed to be due to stagnant gas at the bottom of the bed for low velocity conditions.

The burning rate in a fast bed is faster than in a bubbling bed [6]. The increased rate was attributed to higher gas/coarse particle (5-9 mm) slip velocity, which enhanced the rate of oxygen transfer to the particle surface. Basu [4] found the overall burning rate of carbon spheres in a fluidized bed combustor decreased with particle diameter. Mass transfer rate was governed by gas/particle slip velocity in a fast bed, compared to superficial gas velocity in a bubbling bed [6]. Nusselt number and Sherwood number were

also found to be greater in a fast bed than in a bubbling bed [6].

Chemical kinetics and transfer of oxygen to the particle surface were both found to control combustion in a fast bed [6]. Smith [58] stated fluidized bed combustion was primarily diffusion limited. Basu [4] stated the burning rate of a single carbon sphere in a bubbling fluidized bed may be lower than that for a sphere placed in a free air stream at high velocity. He found the burning rate ( $dm/dt$ ) to be proportional to  $d_p^n$ , with  $n$  between 1.22 and 1.55. In theory  $n$  equals 2 for kinetics control and is 1 for diffusion control.

### 2.8.1 Fluidized bed combustion model

Christofides and Brown [16] developed a simple analytical model of char combustion in a bubbling fluidized bed to interpret gas emission data obtained from batching coal into a hot fluidized bed. Their model assumed that char combustion occurs in the emulsion phase and follows a first-order oxidation reaction:

$$-\frac{1}{M_c} \frac{dm}{dt} \Big|_{\text{char}} = N\pi d^2 k [O_2]_e \quad (2.60)$$

where  $[O_2]_e$  is the oxygen concentration in the emulsion phase and is influenced by the rates of oxygen consumption and the interphase transport of oxygen from bubbles to the emulsion phase. Equation 2.60 indicates that the char consumption rate equals the reaction rate. Avedesian and Davidson [2] applied the two-phase theory of fluidization and a quasi-steady assumption on the mass balance of oxygen to obtain the following expression for  $[O_2]_e$ :

$$[O_2]_e = \frac{[O_2]_i}{kN\pi d_1^2 / (A_b\Omega) + 1} \quad (2.61)$$

where  $[O_2]_i$  is the concentration of oxygen entering the fluidized bed.

The overall char reaction rate constant,  $k$ , may have contributions from both film mass transfer and chemical kinetics [16]. Christofides and Brown [16] represented  $k$  by a power law:

$$k = a_0 d^{1-n} \quad (2.62)$$

While this is a simplification of the actual dynamics, it represented several rate-limiting cases well.

Char combustion is a very nonlinear process. For  $t > 3\tau_v$  devolatilization is assumed to be complete and only char burning contributes to  $CO_2$  production. Christofides and Brown [16] applied a quasi-steady state assumption to Eq. 2.27 to get:

$$[CO_2]_R = - \frac{1}{QM_C} \frac{dm}{dt} \Big|_{char} = \frac{[O_2]_i}{Q} \left\{ \frac{kN\pi d^2}{kN\pi d_1^2 / (A_b\Omega) + 1} \right\} \quad (2.63)$$

where  $k$  depends on diameter according to Eq. 2.62.

Assuming  $N$  spherical char particles burning as shrinking cores the mass  $m$  is:

$$m = N\rho_c \pi d^3 / 6 \quad (2.64)$$

Substituting for  $m$  in Eq. 2.63, the  $CO_2$  concentration is expressed as:

$$[\text{CO}_2]_R = -\frac{1}{2} \frac{N\pi\rho_c d^2}{M_c} \frac{d(d)}{dt} \quad (2.65)$$

Integrating Eq. 2.60 yields a transcendental equation relating particle diameter to time [16]:

$$\frac{1}{3} \frac{N\pi(d_i^3 - d^3)}{A_b\Omega} + \frac{1}{a_o} \left(\frac{1}{n}\right) (d_i^n - d^n) = \frac{2}{\rho_c} M_c [\text{O}_2]_i t \quad (2.66)$$

For times much shorter than the burnout time, Eq. 2.66 can be linearized using a Taylor series expansion [16,17]:

$$\frac{d(t)}{d_i} = 1 - \frac{2M_c[\text{O}_2]_i t / \rho_c}{N\pi d_i^3 / (A_b\Omega) + d_i^2 / a_o} \approx 1 - \frac{t}{\tau_c} \quad (2.67)$$

where  $\tau_c$ , a characteristic time for char burning, is defined by [16,17]:

$$\tau_c - \tau_i = \frac{\rho_c d_i^n}{2 a_o M_c [\text{O}_2]_i} \quad (2.68)$$

This linear model can also be expressed, for short combustion times, as an exponential decay:

$$\frac{d(t)}{d_i} \cong \exp(-t / \tau_c) \quad (2.69)$$

which is convenient for some data analysis. Christofides and Brown [16] found the exponential decay model of Eq. 2.69 fit their data. The contribution of interphase mass transfer of  $\text{O}_2$  between bubble and emulsion phase ( $\tau_i$ ) to the characteristic time is defined by:

$$\tau_i \equiv \frac{3m_i}{A_b \Omega_C [O_2]_i} \quad (2.70)$$

For a circulating fluidized bed where there are no distinct bubble and emulsion phases,  $\tau_i$  is zero.

For spherical particles burning as constant density shrinking cores the diameter is related to the mass as:

$$\frac{d(t)}{d_i} = \left( \frac{m(t)}{m_i} \right)^{1/3} \quad (2.71)$$

where  $m(t)$  represents the amount of carbon mass remaining in the char at time  $t$ , and  $m_i$  is the initial mass of char carbon.

Substituting Eq. 2.71 for the diameter into Eq. 2.65, the following expression for  $CO_2$  concentration is obtained:

$$[CO_2]_R = \frac{N\pi\rho_C d_i}{2\tau_C} \exp\left(-\frac{t}{\tau_C/3}\right) \quad (2.72)$$

Combining Eq. 2.29 with Eq. 2.72 the  $CO_2$  concentration beginning at the  $CO_2$  peak during devolatilization can be modeled as:

$$[CO_2]_R = [CO_2]_{avg} + A \exp(-t/\tau_v) + B \exp(-t/(\tau_C/3)) \quad (2.73)$$

where  $[CO_2]_{avg}$  is the steady state  $CO_2$  background concentration. The coefficients  $A$  and  $B$  are expressed as:

$$A = Q\{[CO_2]_i - [CO_2]_f\} = Ng_o \quad (2.74)$$

$$B = [CO_2]_f - [CO_2]_{avg} = \frac{N\pi\rho_C d_i}{2\tau_C} \quad (2.75)$$

Avedesian and Davidson [2] found the combustion of small particles (less than 100 $\mu$ m) to be kinetically controlled, while diffusion controlled the combustion of larger particles. Ross and Davidson [53] concluded this was the result of the temperature difference between the particle and the bed: small particles would be at nearly the same temperature as the bed material, while larger particles would be up to 150 $^{\circ}$ C hotter.

Summarizing char combustion, particles larger than about 1 mm burn mainly by diffusion control at 850 $^{\circ}$ C bed temperatures for bituminous char and somewhat higher temperatures for anthracite and semi-anthracite char. When burning low rank chars, burning times for 1.5 mm particles are between 40 and 80 s, and burning times for 12 mm particles are from 1000 to 2000 s. A shrinking particle combustion model applies for all except very small particles.

The controlling mechanism is dependent on the particle size and combustion temperature. Evidence suggests that at combustion conditions typical of fluidized bed combustors, chemical reaction dominates for particles smaller than 100 $\mu$ m, while mass diffusion completely controls the overall reaction rate for particles larger than 1mm. Of course, as large particles burn they get smaller, and the controlling mechanism shifts from diffusion to chemical reaction, but most of the mass is consumed during diffusion controlled reaction. However, large coal particles can fragment during devolatilization and combustion, substantially reducing burnout time.

Starting from the definition (Eq. 2.67), which relates  $d(t)/d_i$  to  $\tau_c$  and from Avedesian and Davidson [1] and Beér [30] where the molar rate of flow of oxygen to a single particle ( $\dot{N}$ ) is:

$$\dot{N} = -\frac{\pi\rho_c d^2}{24} \frac{d(d)}{dt} = 2\pi\text{Sh}D_G d C_p \quad (2.76)$$

where  $\rho_c$  is the char density,  $d$  is particle diameter,  $Sh$  is the Sherwood number,  $D_G$  is the molecular diffusivity coefficient in the gas phase, and  $C_p$  is the oxygen concentration in the particulate phase.

Combining Eq. 2.67 and 2.76, it can be shown:

$$\frac{1}{\tau_c} \exp\left(-\frac{3t}{\tau_c}\right) = \frac{48ShD_G C_p}{\rho_c d_i^2} \quad (2.77)$$

For  $t \ll \tau_c$ :

$$\tau_c \approx \frac{\rho_c d_i^2}{48ShD_G C_p} \quad (2.78)$$

This would indicate, for constant  $Sh$  and diffusion control, that  $\tau_c$  varies as the square of the initial diameter. Pillai [50] and Basu [4] observed char burning-initial particle diameter power laws between 1 and 2. They attributed this behavior to the combined effects of chemical kinetics and mass transfer.

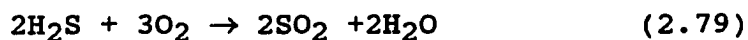
## 2.9 Pollutants

Fluidized bed combustion of coal has the advantages of lower temperature than pulverized coal combustion, reducing production of oxides of nitrogen, and capability for sulfur capture with sorbents introduced into the bed.

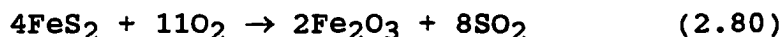
### 2.9.1 Sulfur dioxide, SO<sub>2</sub>

Sulfur is found in coal as either organic or inorganic compounds [66]. The organic sulfur is evolved with the volatiles, while the inorganic sulfur, mainly  $FeS_2$ , is burned with the char [66]. Verweyen, et. al. [66] state the primary

sulfur compound in the volatiles is H<sub>2</sub>S and is converted to SO<sub>2</sub> per the following reaction:



During char combustion the reaction which governs the sulfur release as SO<sub>2</sub> is [66]:



The SO<sub>2</sub> is then captured by limestone to form CaSO<sub>4</sub>. The Fe<sub>2</sub>O<sub>3</sub> and CaSO<sub>4</sub> then are disposed of with the ash.

### 2.9.2 Oxides of nitrogen

The nitrogen oxide compounds of interest are nitric oxide (NO), nitrous oxide (N<sub>2</sub>O), and nitrogen dioxide (NO<sub>2</sub>). NO<sub>x</sub> compounds result from oxidation of fuel or air nitrogen [67]. The predominant product is NO, with less than 5% NO<sub>2</sub> [67]. According to Beér [8], 90% of the NO<sub>x</sub> formation is from fuel nitrogen. Bramer, et. al. [19] state 2/3 of N<sub>2</sub>O is produced from the volatiles and 1/3 from the char. Wang, et. al. [68] found volatile nitrogen preferentially reacted to NO rather than N<sub>2</sub>O.

In general the volatiles nitrogen react to form NO, while the char nitrogen reacts to form N<sub>2</sub>O [8,45,68]. The formation of NO is described by the Zeldovich or modified Zeldovich mechanisms [67]. High temperatures and adequate oxygen concentration are necessary to produce NO. Its formation is dependent on combustion temperature and stoichiometry, but is considered insignificant at less than 1800°F. Beér [8] found NO to be preferentially formed near the coal inlet point where the oxygen concentration was high.

According to Lohuis, et al., [49]  $N_2O$  is formed by homogeneous gas phase reactions in which HCN is the main precursor. They also found  $N_2O$  formation to be significant in the temperature window 1050-1400°F found in fluidized bed combustors.  $N_2O$  formation increases with temperature [45,49] and as coal rank decreases [49]. Bramer, et. al. [9] found  $N_2O$  production to decrease and  $NO_x$  production to increase with temperature, and more  $N_2O$  to be produced at higher recycle ratios, and as the primary air ratio increased. This temperature relationship, obtained in a circulating fluidized bed combustor, contradicts other results obtained in bubbling fluidized beds.

Staged combustion has been found to be a positive factor in decreasing oxides of nitrogen [9,68]. Bramer, et. al., [9] found both  $N_2O$  and  $NO_x$  decrease with staged combustion. Wang, et. al. [68] found combustion to precede in the whole combustion system of a circulating fluidized bed combustor, including cyclones. In the unstaged condition, NO concentration was found to be fairly constant along the axial length, while  $N_2O$  increased with height for both staged and unstaged conditions. With staging, the NO concentration decreased with height, and was much higher in the lower part of the bed than in the unstaged condition. NO was sensitive to secondary air ration, while  $N_2O$  was not.

### 3. FTIR THEORY

Although the basic components and theory of Fourier transform infrared (FTIR) spectrometers were originally developed in the early 19<sup>th</sup> century, they did not come into commercially viable general use until the early 1970's [34,37]. Infrared spectroscopy has the advantages of continuous (near real-time) operation and low maintenance compared to gas chromatography and low cost and more specific definition of spectral structure compared to mass spectroscopy [24]. The availability of low-cost, high-power personal computers has been closely tied to the development of FTIR spectroscopy.

#### 3.1 Origins of Theory of Light

Until the early 19<sup>th</sup> century Newton's "corpuscular" theory of light was predominant among scientists. However, it failed to explain why a prism produced colors from a beam of light or why glass bent a light beam. In 1802 Thomas Young passed a beam of light through a pair of closely spaced slits onto a wall beyond [24,38]. This produced a pattern of bright and dark bands, indicating light added to light produced dark. He explained this in terms of interference of light waves and concluded there was a close similarity between the nature of sound and the nature of light. However, this theory did not explain common characteristics of light such as reflection, refraction, and dispersion and was widely disregarded at the time.

About two decades later Augustin Fresnel began to independently study the theories of light [38]. His experiments led to the rediscovery of the wave theory of light. In 1819 the Academy of Sciences in Paris awarded him a prize for his work. In 1822 he published an elementary treatise on the theory, but pointed out that other elementary

effects, such as the absorption of light by materials, remained unexplained. Fresnel's explanations were convincing, and the corpuscular theory of light was rapidly abandoned.

When light from a single source is divided into two parts and recombined after the two parts travel different distances, bright and dark areas in the combined beam can be seen. The bright and dark interference bands, or "fringes", are created by the constructive and destructive interferences of the peaks and valleys of the light waves. When the peaks coincide a bright pattern is produced, and a dark fringe is produced when the path difference is a half-wavelength (Fig. 3.1). With a light source having more than one wavelength present, each individual wavelength interferes with itself, producing multiple, overlapping interference patterns. This often creates a white smear.

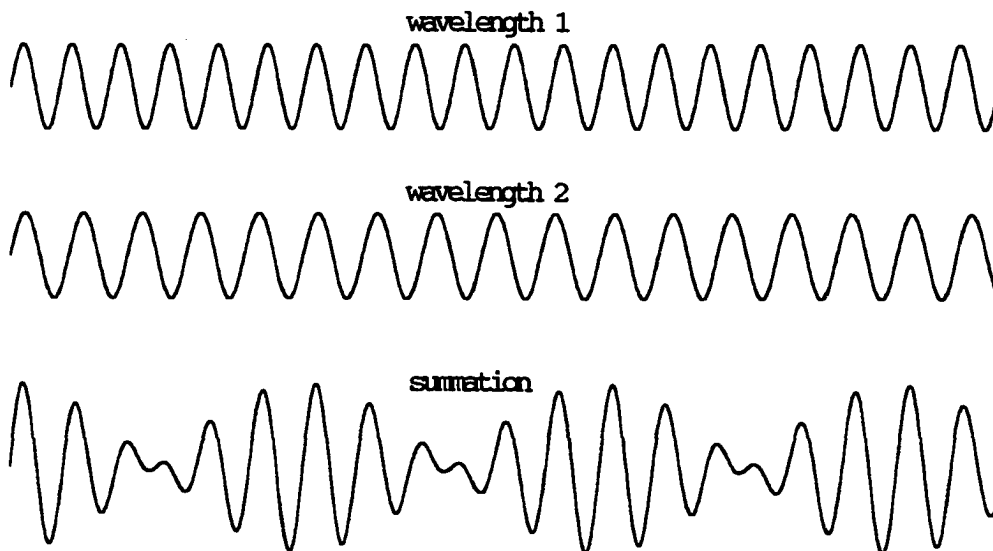


Figure 3.1: Light wave addition to create maximum and minimum intensities. Ratio of wavelength 1 to wavelength 2 is 5:6

### 3.2 Optical Spectroscopy

In the early 19<sup>th</sup> century researchers sought a source of monochromatic light for their experiments in optics [37]. Wollatson, in 1802, developed a simple, but crude, instrument consisting of a light source, a narrow slit through which the light was passed, a prism positioned such that the light was bent at right angles to the slit, and a viewing screen [37]. Despite overlapping images, weak color bands, and wash-out by room light, Wollatson was able to observe that the spectrum of sunlight was crossed by four or five dark bands, not a continuous band as Newton had thought [37].

In 1814 Joseph Fraunhofer replaced the viewing screen with a telescope to view the light directly and was able to observe brighter images in greater detail. He found the spectrum of sunlight had hundreds of narrow lines, not just the few seen by Wollatson [23,34,37]. These spectral lines, named after Fraunhofer [34], were found to correspond to specific colors which were absent from the light. Similar lines were found in the light from bright stars and planets. The positions of the lines never changed, although they were different for different stars and planets.

Sir John Herschel, in 1823, and then Brewster 10 years later [37], found dark bands in light passed through colored glass or gases. Brewster realized the "absorption spectra" of some of these gases were similar to those in the solar spectrum. He related the absorption spectra of the sun to particular materials, apparently the first person to do so.

The final essential improvement to the spectroscope came in 1839 when Simms and Swan independently introduced a lens, called a collimator, to make the light rays emerging from the slit parallel before they reached the prism [23], which improved the clarity of the spectrum.

In the middle of the nineteenth century most scientists were not much interested in the origin or characteristic

pattern of the "line spectra" for different substances identified by the spectroscope. Most experiments dealt with the monochromatic emissions of various substances.

Chemical analysis by use of emission spectra was demonstrated in the late 1850's by Robert Bunsen and Gustav Kirchoff [23,37]. They demonstrated that bright lines of the spectrum for materials heated in a flame occupied the same positions, regardless of flame temperature. They stated the general principle that every spectrum was representative of a particular kind of matter, and no other [23]. They also noted that line positions were not altered by different combinations of the same materials in the flames. The science of optical spectroscopy was born, providing an alternative to the tedious analytical methods of the day.

Two types of spectroscopy exist: emission and absorption [37]. Emission spectroscopy deals with the study of light emitted by heated substances. Absorption spectroscopy is the study of frequencies of a continuous incident radiation spectrum absorbed by a substance, such as a gas.

### 3.3 The Interferometer

The heart of the FTIR is the Michelson interferometer, originally designed in 1891 by Albert Abraham Michelson [14,24,29,37] as part of an unsuccessful search for interplanetary "ether". Thomas Young's screen with double slit amounted to an interferometer with fixed path length [37]. The interferometer (Fig. 3.2) is a device used to generate and control an interference pattern [37]. It consists of a source of radiation energy (s), a beamsplitter (b) to divide the light beam into two parts, a fixed mirror (M1) to reflect one of the two beams back to the beamsplitter, a moving mirror (M2) perpendicular to the fixed mirror to reflect the other beam back to the beamsplitter, and a sample chamber (sc) to hold the sample being investigated

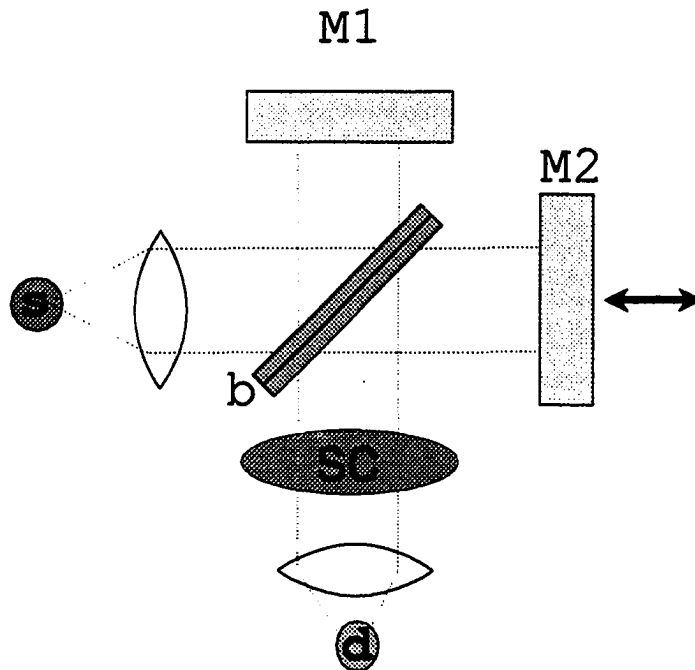


Figure 3.2: Schematic of Michelson interferometer

[13,23,28,36]. To produce the output interference pattern a light, or radiation, source (s), a detector (d) (which was the eye in early experiments), and a mechanism to displace the moving mirror are needed. The Michelson interferometer divides a radiation beam into two paths and then recombines the two beams after a path difference has been introduced by changing the position of the moving mirror. A movement of the moving mirror by  $1/4$  wavelength changes the optical path difference by  $1/2$  wavelength. The beamsplitter reflects part of the incident radiation to the fixed mirror, and transmits part of the radiation to the movable mirror. After the beam is reflected off the two mirrors, it is again partially reflected and partially passed by the beamsplitter [29]. The

portion of the beam passed or reflected back to the source is ignored, as it is the combined beam that is of interest.

The presence of a gas which absorbs infrared radiation in the sample chamber will cause some of the radiation passing through the chamber to be absorbed. The amount of radiation absorbed, and the frequencies at which it is absorbed, depends on the molecular structure of the gas and its concentration.

There are two basic presentations of the FTIR spectrum: transmittance and absorbance. Transmittance,  $T$ , (Eq. 3.1) is the ratio of the radiant power transmitted by a sample to the radiant power incident on the sample [20].

$$T = I_S/I_B \quad (3.1)$$

The intensity of the infrared energy through the sample is  $I_S$  while  $I_B$  is the intensity of the energy without the sample in place, that is, the background.

Absorbance,  $A$ , is directly related to transmittance and is calculated as logarithm to the base 10 of the reciprocal of the transmittance:

$$A = \log_{10}(1/T) \quad (3.2)$$

Quantitative analysis is performed on absorbance spectra. The maximum absorbance unit is 6, but values over 1.5 are very non-linear and not used in quantitative analysis. In this work all FTIR spectra shown are in units of absorbance.

A process called baseline correct is used to correct for sloping, curving, and other undesirable baselines. This correction is usually not required for gases.

A detector measures the radiation intensity variations as a function of path difference of the beam emerging from the interferometer, which is a combination of the beam reflected off the fixed mirror and passing through the beamsplitter and

of the beam reflected off the moving mirror and then again reflected off the beamsplitter. This gives rise to a time (or moving mirror displacement) dependent variation in transmitted optical intensity [24,29]. If the source beam is a broad infrared spectrum, the interferometer output corresponds to the superposition of an infinite number of sine waves having different periods, but common zero phase points which occur when the lengths of the two interferometer arms are equal.

### 3.4 Interferogram

The curve of the output intensity from an interferometer versus the optical path difference (OPD) of the two beams is called the interferogram [37]. Figure 3.3 is an example of a typical interferogram. Initially, consider a monochromatic light source with the fixed and moving mirrors of the interferometer the same distance from the beamsplitter. The beam will be divided in two at the beamsplitter, travel down both arms to the mirrors, be reflected off the mirrors, and recombine at the beamsplitter exactly in phase. As a result, the recombined beam will be at maximum intensity [37]. If the moving mirror is moved by  $1/4$  wavelength, the forward and reflected path will be an extra  $1/2$  wavelength long, and the recombined beams will be  $180^\circ$  out of phase and at minimum intensity. As the moving mirror is displaced, this pattern of maximum and minimum intensities, and all intermediate intensities, will be repeated.

If the source has multiple wavelengths, each will be modulated in this manner, and the output of the interferometer will be a superposition of these wavelengths. Only when the mirrors are equidistant from the beamsplitter, the zero path difference (ZPD), will all the wavelengths combine to be a maximum. Away from the ZPD the various components of the wavelengths fall out of step and the intensity settles down to

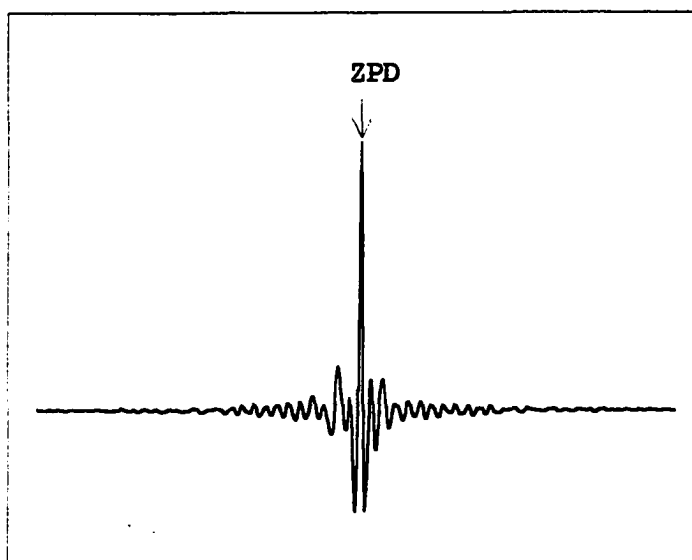


Figure 3.3: Typical interferogram

an average value. The exact shape of the interferogram is closely connected with the wavelength distribution of the source.

Since the interferogram is recorded on a computer in a digitized form the samples must be taken at equal spacing of path difference and the absolute value of the spacing must be known. This is accomplished on modern FTIR's with a helium-neon laser and a second reference interferometer [29,37]. The moving mirror of the reference mirror is connected to the moving mirror of the interferometer and the interferogram is sampled at the zero-crossings of the reference helium-neon laser interferometer. These zero-crossings occur at exact spacing, which establish the path difference for the interferometer.

Fourier transform spectroscopy (FTS) is the technique used to determine a spectrum from the interferometer output power (radiation intensity). Taking the Fourier transform of the interferogram produces a spectrum, which relates

interferometer output power to the frequency, which is converted to wavenumber [14,37]. The interferogram and infrared spectrum of the sample contain the same information, just rearranged. The power of the combined beams in the interferometer is recorded as a function of the phase delay and shows functions that are basically periodic.

An ideal interferogram is symmetric about the zero path position of the mirror and can theoretically be decomposed into a series of cosine waves. The Fourier transform of such a function has a real part only, relating amplitude of each frequency of cosine wave to a frequency in the spectrum [37]. In reality, because of imperfections in the interferometer, the interferogram is not symmetric and the Fourier transform will have an imaginary part as well as real. Three general methods have been developed for phase correction: magnitude calculation, Mertz technique, and Forman technique [14,37]. Johnston [37] and Chamberlain [14] describe these methods in detail.

A spectrum is a graphical representation of the intensity of the infrared region reaching the detector at each frequency or wavelength measured. This spectrum (called a single-beam spectrum) is used for qualitative and quantitative analysis. The intensity at a given frequency is determined by the characteristics of the optical bench and the sample, if any.

### 3.5 Apodization

Ideally, the interferogram should be measured to infinite optical path difference to yield a spectrum in which all the frequencies comprising the radiation source can be properly recorded [37]. When the interferogram is truncated (which it necessarily is because the data set is finite), the sudden cut-off of data results in oscillations around sharp spectral features. The incomplete data is compensated for by a

mathematical compromise known as apodization, which is accomplished automatically before the Fourier transform is performed. Apodization removes the spurious sidelobes around spectral features by gradually smoothing the interferogram at zero intensity as the measurement comes to an end [29,37]. Excessive apodization reduces the resolution of the data and broadens spectral peaks.

Because apodization reduces the relative contribution of points far from the ZPD, it "dilutes" the maximum path difference and has the drawback of worsening the spectral resolution. Thus, there is a trade-off between the reduction in spectral distortion and the decrease in resolution [29,37]. Smoothing only the last few points of the spectrum will alter the resolution and sidelobes little, while smoothing points near the ZPD will have drastic effects.

Any function which has a value of 1 near the ZPD and decreases with increasing retardation will serve as an apodization function [29]. Common apodization functions are boxcar truncation, trapezoidal, triangular, triangular squared, Bessel, and cosine [29,39]. Triangular apodization mathematically weights the interferogram data in a linear relationship to reduce the side lobes. The Happ-Genzel apodization function is similar to a triangular function and is a popular function for commercial FTIR's. It suppresses side lobes more effectively than triangular apodization, with less reduction in resolution.

The line shape of a spectrum can be improved by adding data points between the collected points, called zero filling. It does not improve the true resolution and takes more time per spectrum. However, it can be beneficial in identifying unknown compounds.

### 3.6 Resolution

Resolution is the ability of the FTIR to meaningfully discern two closely spaced spectral features [14,29,37]. The higher the resolution (i.e., the smaller the resolution number, expressed in  $\text{cm}^{-1}$ ) the more closely spaced peaks can be revealed. Increasing the resolution requires that the distance traveled by the moving mirror be increased. This is important for the study of gases because some of the fine line structures for certain gases have widths as little as  $0.2 \text{ cm}^{-1}$ . If the resolving power of the instrument is less than the spacing of the spectrum being observed, a series of fine lines will be seen only as a smooth hump [34,69]. Figure 3.4 is an example of the CO spectral region at  $2 \text{ cm}^{-1}$  and  $8 \text{ cm}^{-1}$  resolution. The fine line structure seen at  $2$  resolution is not seen at  $8$  resolution.

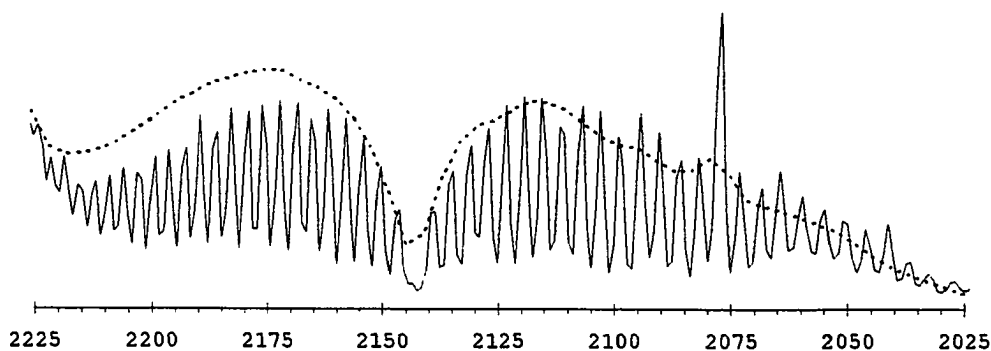


Figure 3.4: Comparison of CO spectral region at 2 resolution (solid line) and 8 resolution (dashed line)

Resolution is commonly measured in wavenumbers as the minimum distance between two spectral lines that can be distinguished. The resolving power of most modern FTIRs is adjustable to as low as  $0.125\text{ cm}^{-1}$ . In practice, gases are commonly observed with the FTIR set at  $0.5\text{ cm}^{-1}$  resolution.

### 3.7 FTIR Advantages

Three developments which significantly improved the performance of interferential spectroscopy (of which an FTIR is a specific case) are the Fellgett, or multiplex, advantage the Jacquinot, or throughput, advantage, and the Connes' advantage [14,24,29,30,37,64]. All three act to increase the signal to noise ratio. The multiplex advantage, the most important of the three, results from the fact an interferometer observes the whole spectral band at once, as opposed to having to observe each spectral element for short periods of time.

The throughput advantage results from the circular symmetry of the interferometer, as opposed to the slits of a conventional dispersive spectrometer, which restrict the wavelengths reaching the detector. To increase spectral resolution the slits must be narrowed, further reducing the throughput. The resolution of an interferometer, with an unobstructed circular aperture, depends on optical path difference, which does not significantly change the amount of radiation passing through it [14,29,30,37].

The use of a He-Ne laser interferometer to reference the position of the moving mirror, making possible accurate frequency determination is the Connes' advantage [30].

### 3.8 System Components

The various components of an FTIR instrument are housed in a unit called the optical bench, or bench for short. An

interface card in the computer controls communication between the computer and the bench.

### 3.8.1 The source

The best broad-band infrared radiation sources for FTIR spectroscopy approximate "black-body" or ideal thermal radiators [19,37]. The two types of source materials used are ceramics heated to glowing temperature and nichrome wire heated to incandescence. The ceramic units are Globars (a heated bar of sintered silicon carbide) or Nernst glowers (usually an electrically heated hollow tube of zirconium and yttrium oxides) [19]. The Nernst glower has the highest operating temperature of the three, but many of its advantages are offset by its poor emissivity at high wavenumbers. The nichrome wire sources are less expensive and have good emissivity across the mid-infrared spectrum, but have low operating temperature and poor thermal stability, limiting their use in research-grade instruments. Globars are used in most research-grade instruments. Their operating temperature and sensitivity are slightly higher than the nichrome wire and have fairly high emissivity down to  $80\text{ cm}^{-1}$  [29].

### 3.8.2 The detector

The detector converts the optical intensity exiting the interferometer into an electrical signal [37]. Detectors are designed to reduce distortion and electrical noise. There are two basic types of detectors in use: thermal and quantum [29,37].

Thermal detectors operate by sensing the change of temperature of an absorbing material [29,37]. A bolometer is simply a temperature sensing resistor [19,29,37]. A thermocouple senses the change in electromotive force due to temperature change. A Golay detector senses the thermal expansion of a gas in a gas-filled sac which changes the

position of a Moire' movement-detection system. Thermocouples and simple bolometers are rarely used in FTIRs.

A now commonly-used form of bolometer is based on ferroelectric materials [37]. Deuterated Triglycine Sulphate (DTGS) can operate at room temperature and is commonly used in FTIRs. Thermal detectors can respond to a broad range of frequencies, but are relatively slow: 10-100 msec being typical.

Quantum detectors employ a more direct means of converting optical energy into an electrical signal. They depend on the interaction of radiation with the electrons in a solid, which are excited to a higher energy state [29,37]. A semiconductor produces a photo-emission effect such as employed in phototubes when a photon having a large amount of energy strikes the material and boosts the electron energy sufficiently to free it from the material [37]. Mercury cadmium telluride (MCT) detectors make use of the properties of a mixture of two semiconductors [29]. While quantum detectors are more efficient than thermal detectors, the electrical characteristics of their materials are temperature dependent, and they must be operated at temperatures below room temperature [29,37]. MCT detectors must be cooled to liquid nitrogen temperatures (77 K) to operate properly.

### 3.8.3 The cell

The sampling of gases is done in gas cells. The simplest cells are glass or metal cylinders with halide windows for the infrared beam to pass through and fittings for the entrance and exit of the gas [19]. The infrared beam passing from the beamsplitter to the detector is directed through the cell to interact with the gaseous sample in the cell. Gas cells are classified as short path or long path, the path length being the length of the infrared beam in the cell which passes through the gas [19,24]. Path lengths vary

from 5 cm to tens of meters. Short path length cells are used for high concentration gases flowing through a process pipe [24], while lower concentration gases require a long path length cell [19,24].

The most common type of long path cell is a White cell (Fig. 3.5) [24]. A White cell uses a set of three mirrors to reflect the infrared beam back and forth through a fixed volume of gas. Because the White cell steps the beam back and forth between the mirrors, it has a high path length to volume ratio. One of the limitations of the White cell can be slow response to changes in gas composition, in part due to the lack of uniform overlap between the gas volume and optical path, and in part due to turbulent mixing in the large diameter cell [24]. The larger the cell, the greater this problem.

### 3.9 Quantum Mechanics

FTIR spectroscopy is inseparable from quantum mechanics. Spectroscopy is the study of transitions of a system (usually an atom or a molecule) between its states of defined energy [34]. FTIR use is based on the response of matter to electromagnetic energy in the infrared region (wavelength 500 $\mu\text{m}$  to 1  $\mu\text{m}$ ). Electromagnetic wavelength, the distance from one node to the next, is measured in angstroms ( $\text{\AA}$ ), micrometers ( $\mu\text{m}$ ), and centimeters (cm) [63]. The wavenumber (reciprocal centimeter,  $\text{cm}^{-1}$ ) is used more frequently in spectroscopy practice than frequency. A wavenumber can also be expressed as a unit of energy, 1  $\text{cm}^{-1}$  equaling  $1.9855 \times 10^{-16}$  erg/molecule. Both frequency and wavelength are dependent upon energy according to the fundamental Planck equation:

$$E = h\nu = hc/\lambda \quad (3.3)$$

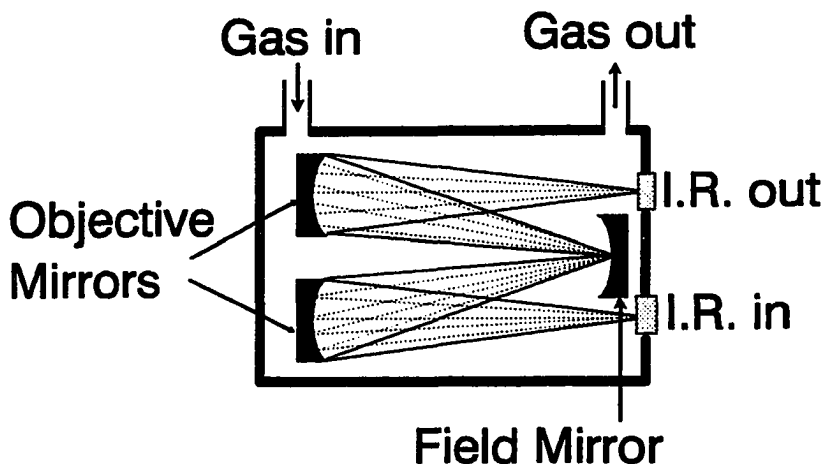


Figure 3.5: White gas cell

where  $E$  is energy,  $h$  is Planck's constant ( $6.62391 \times 10^{-27}$ ),  $c$  is the velocity of light ( $3 \times 10^{10}$  cm/sec),  $\nu$  is the frequency, and  $\lambda$  is the wavelength. The mid-infrared region,  $400 \text{ cm}^{-1}$  to  $4000 \text{ cm}^{-1}$ , contains molecular vibrations of chemical significance and is attractive for chemical analysis.

Radiation is viewed as having a dualistic nature - the wave properties of frequency and wavelength and the particle property of momentum. In 1923 de Broglie postulated that matter also possesses a similar dualistic nature. He postulated that, for an electron of mass  $m$  and velocity  $V$ , the wavelength is given by

$$\lambda = \frac{h}{mV}. \quad (3.4)$$

In 1926 Schrödinger described de Broglie's matter waves using the differential wave equation. The wave function  $\Psi$ , which solves the Schrödinger equation, has the characteristics of a probability function. Solutions to this equation exist only for discrete quantum energy levels [61].

As matter absorbs energy, it is absorbed only in discrete, quantum amounts, as opposed to continuous amounts. From de Broglie's equation (Eq. 3.4) this means the wavelengths also exhibit discrete behavior.

Molecular energy is separable into three modes: translation, rigid rotator (rotation), and harmonic oscillator (vibration) [61]. All polyatomic and hetero-nuclear diatomic molecules absorb infrared radiation. Monatomic gaseous molecules exhibit only a translational energy mode [19]. These monatomic gases, such as radon, and homonuclear diatomic molecules such as oxygen and nitrogen do not have infrared bands and must be measured by non-infrared means. Infrared and Raman spectroscopy use the vibrational modes of energy [34].

Changes in the energy of molecular vibration are produced by absorption of radiation energy. The pattern of absorption depends on the physical properties of the molecule, such as the number, type, and bond characteristics of atoms. The energy differences found in vibrational spectra are approximately one hundred times greater than those in rotational spectra. The type of energy mode excited and the amount of energy absorbed lead to the unique spectral features found in FTIR spectroscopy for different species.

A molecule containing  $n$  atoms will exhibit  $3n-6$  normal vibrations ( $3n-5$  for linear molecules) [19,61]. Because of this, larger polyatomic molecules (such as heavy hydrocarbons) will have more numerous and complex spectral features than diatomic or triatomic molecules, which are largely studied in this research.

Diatomic molecules, such as NO and CO, have a single major band that is an array of individual lines, each with a width of about  $0.2 \text{ cm}^{-1}$ . Linear polyatomic molecules like CO<sub>2</sub> and N<sub>2</sub>O also show arrays of individual lines. Non-linear polyatomic molecules like SO<sub>2</sub>, CH<sub>4</sub>, and H<sub>2</sub>O have many apparent

"lines" that are actually small bundles of lines, with the widths of the bundles varying from  $0.2 \text{ cm}^{-1}$  to many  $\text{cm}^{-1}$ .

Analysis of oxides of nitrogen with infrared is made more difficult because their rates of formation are functions of temperature and because they react with oxygen and alkali halides [70]. Nitrous oxide,  $\text{N}_2\text{O}$ , is rather stable, but nitric oxide,  $\text{NO}$ , is very reactive and toxic. Nitric oxide is a main component of smog. Nitrogen dioxide,  $\text{NO}_2$ , is also poisonous and reacts with water vapor to form nitric acid. It is thus understandable that it is desirable to reduce the emissions of these gases. Unlike NDIR instruments, which typically measure total  $\text{NO}_x$ , an FTIR can independently identify and quantify each of the oxides of nitrogen.

### 3.10 Calibration

Because of the high wavenumber and intensity precision of FTIR's [37], they have become widely used in the quantitative analysis of chemical mixtures [19,24,29]. Quantitative analysis of a specific component in a mixture is accomplished by comparison of the intensity of a unique absorption band with the same infrared band from the pure component of known concentration [19].

Of concern is the interference of strongly absorbing water vapor with other species. Water vapor can be dealt with by condensing it out of the gas sample, removing it by non-condensing methods, establishing a calibration curve for it, or subtracting out the water vapor from the spectrum being quantified. Condensing out the water vapor is not suitable for this research as it absorbs gases, such as  $\text{SO}_2$ , as it condenses.

For absorption spectrometry, the law relating spectral band intensity to concentration is the Bouguer-Beer-Lambert law, more commonly known simply as Beer's law [18,29,37]. An infinite dilution of a liquid sample or a gas at a very low

pressure in an instrument working ideally must exist for strict adherence to the law. The IR spectrum of a multicomponent mixture is the additive summation of absorption frequencies for all the species present [18]. The presence of a unique, reasonably strong absorption band for each component that is not interfered with by other components [19] is required to establish quantitative analysis.

For a single solute in a nonabsorbing solvent, Beer's law can be expressed as [19,29]:

$$A=abc \quad (3.5)$$

where A is the absorbance (Eq. 3.2), a is the absorptivity, b is the pathlength, and c is the concentration. For a multiple component mixture, a series of such equations is obtained for each substance. Beer's law becomes inaccurate above 1.5 absorbance units due to non-linearities [18]. Tall spikes in spectra above 1.5 absorbance units are typically artifacts. Good quantitative analysis can be achieved in the infrared region by keeping absorbance A less than 1.5 absorbance units (and preferably less than 0.7), using broad spectral bands rather than narrow bands, using bands not sensitive to the environment, checking calibration frequently, and watching for temperature effects [18].

Quantitative infrared analysis routines in common use are all based on Beer's law [21]. The simplest applications typically use peak heights or peak areas and a graph of concentration versus absorbance or a linear least squares regression [21]. Two methods of solving the set of simultaneous Beer's law equations for a multiple component mixture have been developed, the P-matrix method and the K-matrix method.

The K-matrix method (Eq. 3.6), also called classical least squares (CLS), is mathematically straightforward, but

$$\mathbf{A}=\mathbf{K}\mathbf{C} \quad (3.6)$$

can lead to indeterminate results for concentration in some circumstances, and the standard spectra recorded to determine the absorptivity must be entirely free of impurities, or the impurities concentrations must be known and used in the calculation [21,37].  $\mathbf{A}$  is the matrix of absorbances at several frequencies of the spectra of the samples used for calibration,  $\mathbf{K}$  is the absorptivity matrix, and  $\mathbf{C}$  is the concentration matrix. When the concentration matrix  $\mathbf{C}$  is known, the absorbance matrix  $\mathbf{A}$  is found by experiment, and  $\mathbf{K}$  is calculated. Since  $\mathbf{C}$  is not square, both sides of the equation are multiplied by the transpose of  $\mathbf{C}$  ( $\mathbf{C}'$ ), Eq. 3.7. This method is the best for gas analysis, when no

$$\mathbf{A}\mathbf{C}'=\mathbf{K}\mathbf{C}\mathbf{C}' \quad (3.7)$$

molecular interaction is present and is typically used when pure components are present.  $\mathbf{K}$  is the least squares fit between the observed and calculated absorbances and is often called the calibration matrix.

$$\mathbf{K}=\mathbf{A}\mathbf{C}'(\mathbf{C}\mathbf{C}')^{-1} \quad (3.8)$$

In the quantification process the absorbance  $\mathbf{A}$  of the unknown sample is measured at the same frequencies as the calibration was established, and the concentrations of the components are calculated from Eq. 3.9

$$\mathbf{C}=(\mathbf{K}'\mathbf{K})^{-1}\mathbf{K}'\mathbf{A} \quad (3.9)$$

The concentration is done in this manner, rather than directly inverting  $\mathbf{C}$  and  $\mathbf{K}$  because these matrices will be square if no overdetermination is done.

The **K**-matrix method does have some limitations [21]. The concentration matrix, **C**, must be inverted during the operations and, therefore, must be non-singular. This matrix will be singular if the standard components all have the same ratio to each other in each of the standard mixtures. This is avoided by mixing the various species in random proportions in each known sample. The concentration of each species in each standard must be known. If the real sample contains impurities not contained in the standards the method can fail, therefore all potential components must be included in the analyses [21]. It does perform quite well for non-reacting gases, however.

The **P**-matrix method,

$$\mathbf{C}=\mathbf{P}\mathbf{A} \quad (3.10)$$

also known as inverse least squares, can treat the effects of deviation from Beer's law and can be solved in terms of the absorbance matrix **A** and the known reference concentrations **C** [37]. The principle drawback of this method is that more reference mixtures are required to properly define the **P** matrix [21]. This method is also better when molecular interaction is involved. The **P**-matrix is calculated from

$$\mathbf{P}=\mathbf{C}\mathbf{A}'(\mathbf{A}\mathbf{A}')^{-1} \quad (3.11)$$

The concentration of an unknown sample is calculated directly from Eq. 3.11.

Most modern FTIR spectrometers are provided with software to develop quantification methods. The calibration process consists basically of recording calibration standard spectra of known mixture concentrations, then using the software to calculate the **P** or **K** matrices. When an unknown sample is

quantified, the absorbance is measured, then the **K** or **P** matrix is used to calculate the concentration.

#### 4. SPECTRAL ANALYSIS THEORY

The investigation of the dynamic response of a system can be conveniently tested with spectral analysis [36]. Spectral analysis is frequently used in designing and analyzing automatic control systems and has potential as a powerful tool in evaluating fundamental physical processes occurring in a system, including coal combustion in a boiler.

Characterization of fuels in a fluidized bed boiler by this method is complicated as it depends on the ability to approximate specific, complex physical processes with low-order, linear models and on the sensitivity of the signal processing equipment algorithms and the data analysis. However, systems operating close to steady-state, for which only a single input variable is perturbed, can often be represented by a linear, ordinary differential equation of low order [57].

The theory that spectral analysis of  $\text{CO}_2$  and  $\text{CO}$  concentrations at the outlet of a combustor could be used to evaluate the devolatilization and char burnout times was tested. Characteristic times were compared to combustion parameters employed in a computer model of coal combustion to determine if the characteristic times were, in fact, the devolatilization and char burnout times.

##### 4.1 Signal Identification

Graupe [29] states that the characteristics of a system can be identified using Fourier transform techniques by measuring the response of the system to a specific input. He lists three types of inputs used in system identification: step, sinusoidal, and impulse.

The system response  $y(t)$  of a dynamic system  $g(t)$  to an impulse input function  $u(t)$ , can be represented by the block diagram of Fig. 4.1.

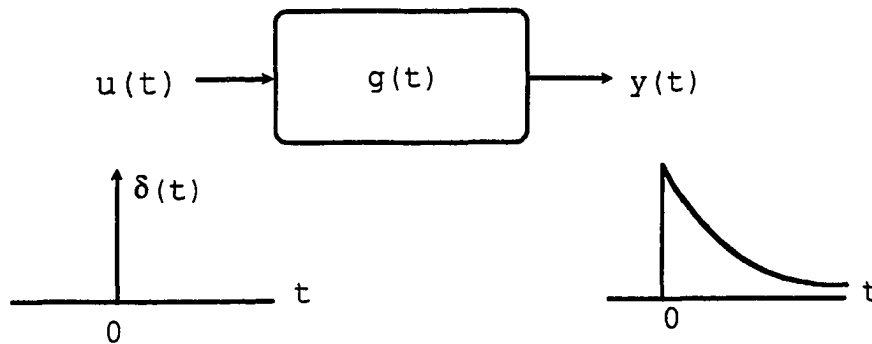


Figure 4.1: Block diagram of system input and response to impulse input

The transfer function of a first order linear process is given by Eq. 4.1 [28,36,48]:

$$G(i\omega) = \frac{K}{\tau i\omega + 1} \quad (4.1)$$

where  $\tau$  is the characteristic time of the system and  $K$  is the system gain. Consequently, the system response to an impulse input is [28,36]:

$$g(t) = \mathfrak{F}^{-1}G(i\omega) = \frac{K}{\tau} e^{-t/\tau} \quad (4.2)$$

The transfer function and impulse response function of a linear time-invariant system both contain the same information about system dynamics [48]. The transfer function of a system may be derived by applying the Fourier transformation to the response to an impulse input [28]. It is possible to obtain complete information about the dynamic characteristics of the system by exciting it and measuring the response [28].

The Fourier transform of the impulse response  $y(t)$  is given by:

$$Y(j\omega) = G(i\omega) \cdot U(i\omega) = G(i\omega) \cdot 1 \quad (4.3)$$

where  $Y(i\omega)$ ,  $G(i\omega)$ , and  $U(i\omega)$  are the Fourier transforms of  $y(t)$ ,  $g(t)$ , and  $u(t)$  respectively, and the input function is an impulse. If  $Y(i\omega)$  is plotted versus frequency  $\omega$ , the frequency response  $G(i\omega)$  of the system is obtained [28].  $G(s)$  may now be derived from  $G(i\omega)$  by employing Bode diagram techniques. On a Bode diagram,  $20 \log_{10} |G(i\omega)|$  vs.  $\log_{10}(\omega)$ , the asymptote is horizontal for  $\omega < 1/\tau$ , and has a slope of -20db/decade at  $\omega > 1/\tau$  [28,48].

Junk [39] applied control theory techniques to the study of coal combustion and developed a transfer function (Eq. 4.4)

$$Y(s) = \frac{b_1 s + b_0}{s^2 + a_1 s + a_0} \quad (4.4)$$

to describe the impulse response of the combustion process for large coal particles (about 5 mm diameter). This transfer function represents the Laplace transform of two concurrent first order processes (Eq. 4.5) with A and B being process

$$y(t) = A \exp(-t / \tau_v) + B \exp(-t / \tau_c) \quad (4.5)$$

gains and  $\tau_v$  and  $\tau_c$  characteristic times, with  $\tau_v$  less than  $\tau_c$ . In Eq. 4.4 the coefficients  $a_i$  and  $b_i$  are:

$$a_0 = \tau_v \tau_c \quad (4.6)$$

$$a_1 = \tau_v + \tau_c \quad (4.7)$$

$$b_0 = A \tau_v + B \tau_c \quad (4.8)$$

$$b_1 = A+B \quad (4.9)$$

For small particles the transfer function Junk [39] obtained (Eq. 4.10) contained second order numerator dynamics

$$Y(s) = \frac{b_2s^2 + b_1s + b_0}{s^3 + a_2s^2 + a_1s + a_0} \quad (4.10)$$

and third order denominator dynamics because it modeled the inflection contained in the char burnout at longer times due to the end of burning of the smallest particles in the batch prior to the other particles. For this work, the combustion model Eq. 2.73 is similar to Junk's [39] large particle model as it applies to short times only.

#### 4.2 Autocorrelation Function

A white noise input is one which is an uncorrelated random input having an infinite flat frequency spectrum and zero mean [28]. If  $n(t)$  is the white noise input, then

$$E\{n(t)n(t + \tau)\} = \sigma^2\delta(t) \quad (4.11)$$

where  $E$  is the expected value operator.

If a white noise forcing function is put on the system input  $u(t)$ , the output  $y(t)$  is correlated noise which can be characterized by the autocorrelation function,  $R_{yy}(t_1, t_2)$ , defined [10,14,41] as

$$R_{yy}(t_1, t_2) \stackrel{\Delta}{=} E\{y(t_1)y(t_2)\} \quad (4.12)$$

All processes have an expected value of zero when it is assumed the means have been subtracted out. The autocorrelation function indicates how well the value of  $y(t_2)$

can be determined given  $y(t_1)$ . If a process is stationary (i.e., all transients have died out and statistical properties are invariant [9,15,42]) then the autocorrelation function is

$$R_{yy}(\tau) = E\{y(t)y(t + \tau)\} \quad (4.13)$$

where  $\tau$  is the time shift between any two points. The larger the time shift  $\tau$ , the lower the correlation.

### 4.3 Power Spectral Density

Classical Fourier analyses fail when applied to time series because the variance does not decrease as the length of the time series increases [36]. The power spectral density (PSD) of a random process describes the distribution of power with frequency [10,41]. For wide sense stationary processes (i.e., the probability density functions describing the process are dependent only on time differences  $t_2 - t_1$  [10]), the Wiener-Kinchine theorem [10,14,41] states the PSD,  $S_{yy}(i\omega)$ , is:

$$S_{yy}(i\omega) = \mathcal{F}\{R_{yy}(\tau)\} = \int_{-\infty}^{\infty} R_{yy}(\tau) e^{-i\omega\tau} d\tau \quad (4.14)$$

where  $\mathcal{F}\{\cdot\}$  is the Fourier transform, and  $\omega$  is frequency. The PSD of white noise is simply the variance squared,  $\sigma^2$ , for all  $\omega$ . For linear systems with random inputs, the following relationship applies:

$$S_{yy}(i\omega) = G(i\omega)G^*(-i\omega)S_{xx}(i\omega) \quad (4.15)$$

where  $G^*$  denotes complex conjugate of the coefficients of  $G$  and  $S_{xx}(i\omega)$  is the PSD of the input function. For white noise input  $S_{xx}(i\omega) = \sigma^2$ , and using Eq. 4.15:

$$S_{yy}(i\omega) = |G(i\omega)|^2 \sigma^2 \quad (4.16)$$

A log-log plot of  $10\log_{10}(S_{yy})$  vs.  $\log_{10}(\omega)$  is a Bode plot. Direct measurement of the input function is not needed.

#### 4.4 The Periodogram

The PSD depends on an infinite number of autocorrelation function values, therefore it is almost impossible to calculate in practice because actual data sets are finite. It is necessary to resort to a good estimate [41]. In many cases, the autocorrelation function  $R_{yy}$  used in Eq. 4.14 is not available, but a finite, zero-mean data set does exist. The PSD of that data set can be estimated [10,41] as

$$S_{yy}(i\omega) \approx \lim_{T \rightarrow \infty} E \left\{ \frac{1}{T} |\mathfrak{F}(y(t))|^2 \right\} \quad (4.17)$$

where  $y(t)$  is defined over the limits  $[0, T]$ . The quantity  $E \left\{ \frac{1}{T} |\mathfrak{F}(y(t))|^2 \right\}$  is defined as the average periodogram. Thus, the PSD is estimated by the average periodogram. The periodogram is a spectral concept in the usual sense of being related to the Fourier transform of a time signal [10]. Using this relationship, the ordinate of the Bode plot becomes

$$10\log_{10}[(1/T)\mathfrak{F}(y(t))\mathfrak{F}^*(y(t))] \quad (4.18)$$

This function is easily calculated using modern computers and mathematical analysis programs.

More experimental data than might be intuitively expected is required for reliable determination of the autocorrelation function [10]. The PSD for a given sample signal may be estimated by taking the Fourier transform of the experimentally determined autocorrelation function [10]. The

periodogram of the sample signal may also be used to directly estimate the spectral function [10]. The square of the Fourier transform of the output signal (the average periodogram) is proportional to the spectral density for large  $T$ . However, a pitfall of this technique is the problem of high-frequency components being introduced because of the truncation of a finite data string [10]. Thus, a long time record relative to the typical time variations of the signal is required, regardless of the method used to analyze the data. Some form of averaging is essential when analyzing noise [10]. In summary, this method must be treated with care, as it can be fraught with pitfalls and subtleties [10].

#### **4.5 Pseudo-Random Binary Input**

This technique utilizes a deliberate disturbance introduced to the input of a process [28]. This disturbance has the appearance of being random, but is not truly random [10], and can be a string of random pulses or a single pulse. Either has the effect of exciting multiple harmonics at the output of the process [28]. In this research, the disturbance is a simulated impulse input of coal into the steady-state coal feed rate. The input pulse must be large enough to produce a signal detectable above the steady-state background signal, but small enough not to significantly disturb the steady-state operation of the system (boiler). A frequency spectrum can be obtained from a fast Fourier transform (FFT) of the output. For example, a pulse input in the coal feed rate to fluidized bed combustor yields Bode plot asymptotes

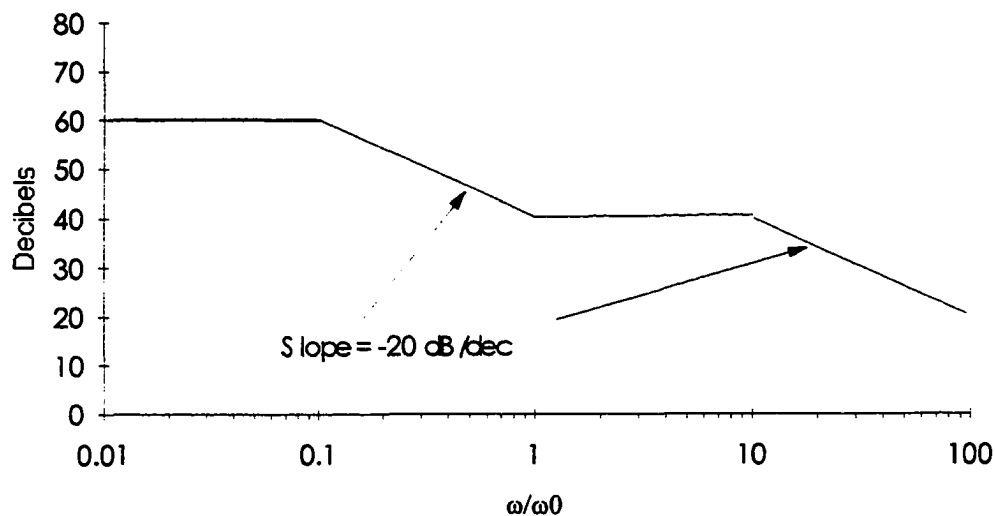


Figure 4.5: First order system Bode plot asymptotes

resembling the diagram in Fig. 4.5, representing two first-order systems in series.

#### 4.6 Limitations of Spectral Analysis

The frequency  $\omega$  of the spectrum is calculated [28] as:

$$\omega = \frac{2\pi k}{N\Delta t}, \text{ where } k=1,2,\dots,N/2 \quad (4.17)$$

where  $N$  is the total number of points in the FFT and  $\Delta t$  is the time increment. The lowest frequency term is  $2\pi/N\Delta t$  and the highest frequency term is  $2\pi N/2N\Delta t = \pi/\Delta t$ .

For the low frequency cornering frequency ( $\omega_c$ ) to be visible, enough data must be collected for the lowest frequency term to be included, or  $N\Delta t = 2\pi/\omega_c$ . The low frequency term won't be as clear unless there are frequency components smaller than this to give a horizontal portion at

frequencies lower than  $\omega_c$ . Ogato [48] shows that the true curve of a first order system bode plot is 3 dB below the straight line asymptotes at the cornering frequencies, 1 dB below at  $\omega_c/2$ , and 0.5 dB below at  $\omega_c/3$ . Choosing to keep the error at 0.5 dB, this now gives:

$$N\Delta t = \frac{6\pi}{\omega_c} \quad (4.18)$$

as the minimum length of data ( $N\Delta t$ ) required to give a clearly discernible low frequency term.

For example, when  $\omega_c = 1/30$ , on the low end of the scale seen, then  $N\Delta t = 565$  s total data time, about 9 minutes. But, when  $\omega_c = 1/500$ , then  $N\Delta t = 9420$  s, = 157 minutes, about 2 1/2 hours, a very long time to record data. Time domain analysis does not have this limitation.

## 5. EXPERIMENTAL APPARATUS AND METHODS

A primary objective of this research is to translate methodology and models developed in the laboratory [16,38] to an industrial-scale circulating fluidized bed boiler and to demonstrate that coal characteristics could be determined during normal operation of an industrial-scale boiler. Thus, this investigation was carried out in two phases.

In the first phase a laboratory scale bubbling fluidized bed combustor was used to validate FTIR calibration and sample handling techniques and to compare results with previous work performed with non-dispersive infrared instruments to prove the concept. In the second phase the FTIR system was moved to the Iowa State University physical plant and sampled combustion emissions from number 2 circulating fluidized bed boiler.

### 5.1 FTIR System

The FTIR system (Fig. 5.1) is a Nicolet Instrument Systems, Inc. Magna 550 FTIR with MCT detector and Infrared Analysis, Inc. model G-2-4-H-BA-Au 20 pass gas cell with 1.7 m pathlength. The volume of this cell is 275 ml, permitting rapid gas exchange and the detection of rapid gas transients. However, since detection sensitivity is dependent on pathlength, the relatively short pathlength (compared to 10-20 m used in most gas analysis systems) has reduced sensitivity. For example, this cell lacks adequate sensitivity to detect 150 ppm of HCl, so this gas was not detected. This was a compromise made in order to detect rapid gas transients during devolatilization.

The FTIR runs Nicolet OMNIC software with series collect option for data collection and analysis. Nicolet Quantir software was used to develop the quantification methods.

The gas sample is drawn through the sampling system by a

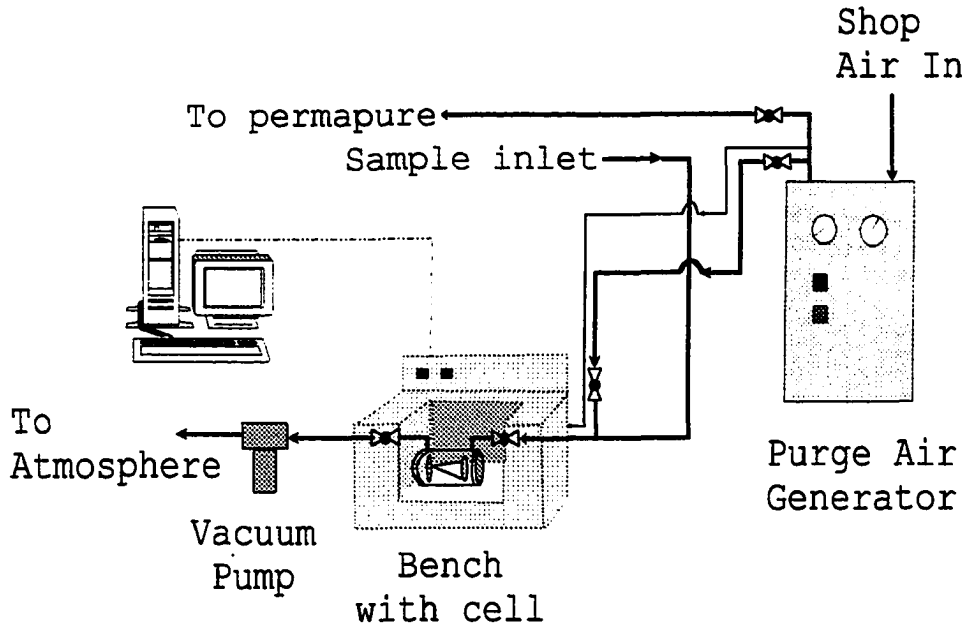


Figure 5.1: Nicolet Magna 550 FTIR system with gas cell and purge air generator

Thomas model 2737-CM vacuum pump rated at  $1.416 \times 10^{-3} \text{ m}^3/\text{sec}$  (3 scfm) at 10" Hg. A Purimetrix model KLDW purge air generator supplies dry, oil-free purge air to the bench to protect the hygroscopic optics, background gas to the cell in lieu of nitrogen due to ready availability, and dry air for the Perma-Pure membrane air dryer at the power plant. The purge air generator takes shop air at 786 kPa (100 psig) nominal and less than  $37.8^\circ\text{C}$  and produces  $1.416 \times 10^{-3} \text{ m}^3/\text{sec}$  (3 scfm) dry air at  $-73.3^\circ\text{C}$  dew point and less than 20 ppm  $\text{CO}_2$ .

## 5.2 FTIR Calibration

Quantification methods were developed using the CLS (K-matrix) method for  $\text{CO}_2$ ,  $\text{CO}$ ,  $\text{SO}_2$ ,  $\text{NO}$ ,  $\text{NO}_2$ , and  $\text{N}_2\text{O}$ . Determination of gas concentrations is performed on absorbance spectra. Calibration standards are gas mixture spectra of

known concentration. The standards were prepared from Air Products, Inc. blended mix certified gas cylinders. The accuracy of the certified standards is  $\pm 5\%$  of component for 1-99 ppm concentration,  $\pm 2\%$  of component for 100 ppm - 0.99% concentration and  $\pm 1\%$  of component for 1-49% concentration.

The standards were prepared by mixing various known amounts of different gases in the cell and calculating the concentration of each gas using partial pressures. An MKS model 121 pressure transducer with model 250 controller was used to measure pressure. From 5-12 standards of each gas were prepared, spanning the range of concentrations of that gas found in the flue gas. From the set of standards, Quantir calculated the absorptivity K matrix using a regression analysis routine. A separate quantification method was prepared for each gas using a region to single or two-point baseline method. The spectral ranges used for calibration are given in Table 5.1.

Validation of the quantification method is accomplished by Quantir by calculating the percent difference between the concentration predicted from the regression line and the actual known concentration of the sample. All methods had percentage errors less than 5%, except for NO, which had two

Table 5.1: Spectral Ranges

GAS	RANGE ( $\text{cm}^{-1}$ )
CO <sub>2</sub>	767.0 - 736.0
SO <sub>2</sub>	1368.2 - 1342.2
CO	2186.6 - 2133.9
NO <sub>2</sub>	1612.3 - 1582.0
NO	1919.0 - 1837.0
N <sub>2</sub> O	1259.0 - 1248.0

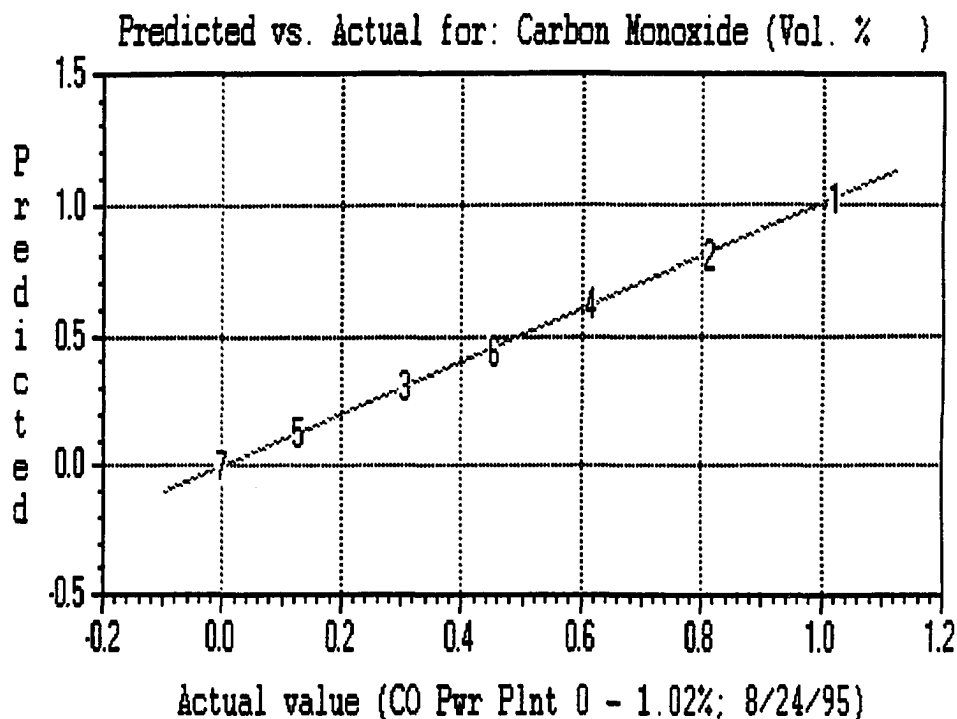


Figure 5.2: Sample plot of quantification validation showing predicted vs. actual concentrations

standards between 14% and 15% errors. Figure 5.2 is a sample plot of the predicted versus actual values for CO.

Figure 5.3 is a reference spectrum of the six gases which were quantified, with the water vapor present to show its impact. The spectral ranges used for calibration were chosen to avoid overlap between gases, avoid interfering water vapor peaks, to keep the absorbance level below 1.5 absorbance units for CO<sub>2</sub>, and to include sharp spectral features, which are better for quantification than smooth slopes. For highly absorbing species, especially CO<sub>2</sub>, shoulders of the spectral features were chosen rather than the large main feature. Figure 5.3 shows how the water vapor impacts identification and quantification, especially for NO, NO<sub>2</sub>, and SO<sub>2</sub>.

Figure 5.4 is the same spectrum with water vapor removed,

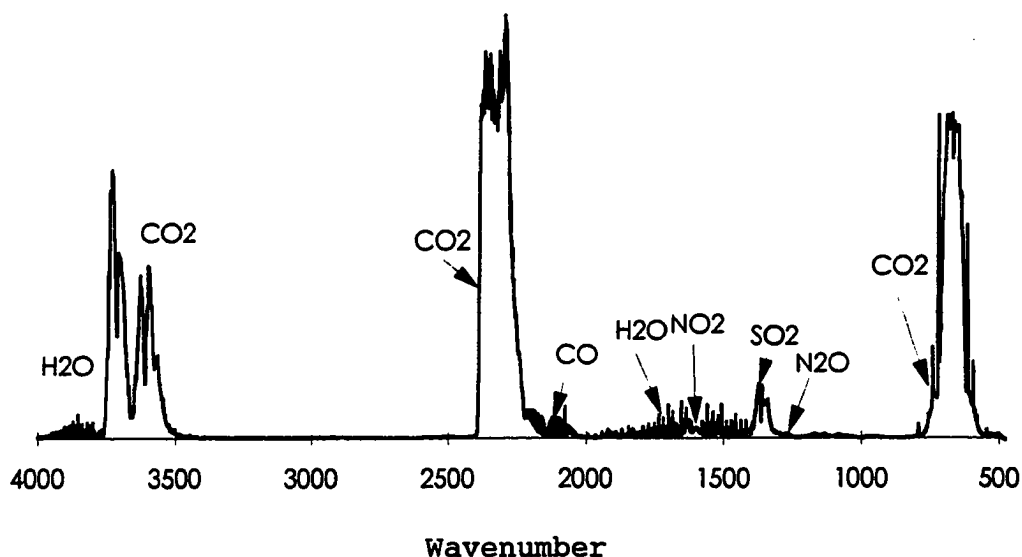


Figure 5.3: Spectrum of 6 quantified gases and water vapor

spectral range shortened to  $2200 - 450 \text{ cm}^{-1}$ , and y-axis scale decreased to 1.0 absorbance units, to better reveal the features of slightly absorbing species. This is the portion of the spectrum where all quantification regions are located. In Fig. 5.4, the overlap between  $\text{SO}_2$  and  $\text{N}_2\text{O}$ , and  $\text{CO}$  and  $\text{CO}_2$  is clearly seen, as well as the features obscured by water vapor in Fig. 5.3.

### 5.3 Bubbling Fluidized Bed Combustor

Laboratory experiments were carried out in a 0.2 m dia. bubbling fluidized bed combustor, shown schematically in Fig. 5.5. Air is introduced into the bed through a 12.7 mm thick stainless steel plate at the bottom of the bed and perforated with 250 2.4 mm evenly spaced orifices. An 80-mesh stainless steel screen is welded to the top of the distributor plate to prevent material flow into the plenum and to act as a flame

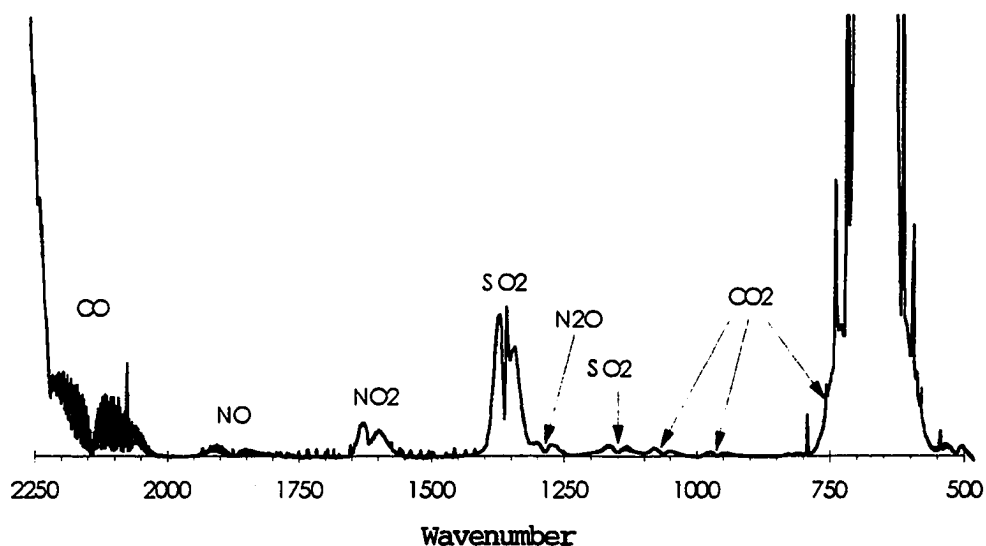


Figure 5.4: Spectrum of 6 gases with water vapor removed and x-axis range reduced to reveal gases

arrester. The large number of orifices prevent gas channeling and provide uniform fluidization within the bed. A plenum below the distributor plate serves as a mixing chamber for the air and natural gas.

The main body of the combustor consists of a 3.2 mm thick stainless steel wall lined with 25 mm Kaocast RFT refractory and surrounded by a cooling water jacket. All components other than the distributor plate and combustor wall are mild steel.

Above the combustion chamber flue gases pass through a 1.22 m long uninsulated freeboard which serves as an afterburner for elutriated fines to improve combustion efficiency and as a muffler. The gases leave the top of the freeboard and are ducted to a roof mounted exhaust fan. A high-efficiency cyclone in the exhaust duct removes 90% of entrained particles greater than 10  $\mu\text{m}$ .

Two 10 cm long electrodes connected to a 10 kV

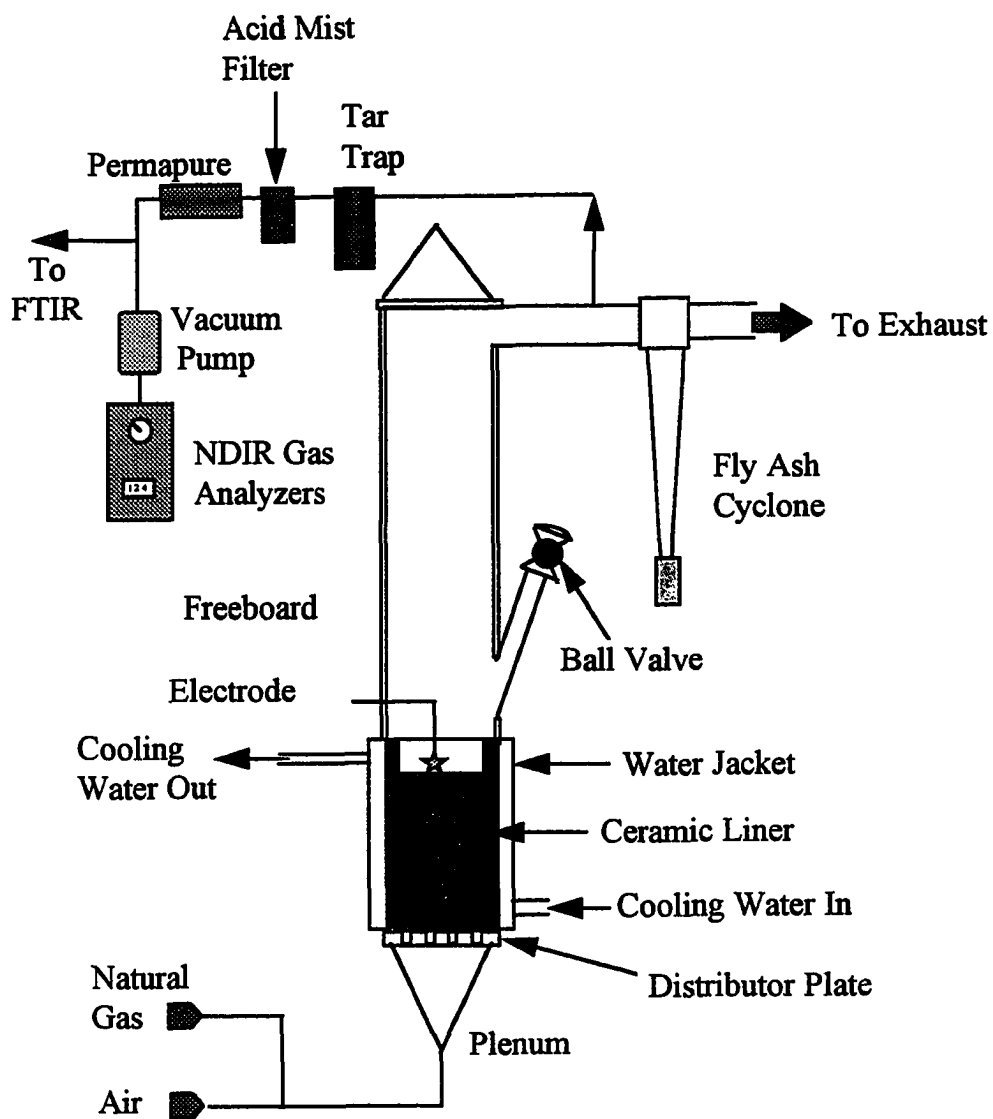


Figure 5.5: Bubbling fluidized bed combustor schematic

transformer ignite the preheat gas. The electrodes are bent downward so the tips are near the bed surface.

The bed material used during experiments was a mixture of 2.5 liters of 16x20 mesh and 2.5 liters of 20x30 mesh river sand. The bed was fluidized with air at atmospheric pressure. In all tests, the air flow rate was set to produce a superficial velocity of 1.2 m/s at a bed temperature of 842°C.

#### **5.4 Combustor Fuel Feeding Systems**

A mixture of air and natural gas was used for preheating the bed and maintaining bed temperature during batch tests. Coal batches were fed to the bed via a 63 mm dia. slanted port on the side of the freeboard. A ball valve was used to close the port while pre-weighted samples were loaded in. The valve was opened to instantaneously dump the sample into the combustor when the data acquisition system was ready.

#### **5.5 Power Plant Sampling System**

The number 2 circulating fluidized bed boiler at Iowa State University power plant was instrumented to conduct industrial-scale boiler experiments. Figure 5.6 is a schematic of the boiler. The boiler is one of two Ahlstrom Pyropower, Inc. boilers installed at the power plant. At full load each of the two CFB boilers is rated at 77110.7 kg/hr (170,000 lb/hr) steam flow, 2895.5 kPa (420 psig), 399°C (750°F), 11,339.8 kg/hr (25,000 lb/hr coal flow rate), and 3,660.5 kg/hr (8,070 lb/hr) limestone flow rate. The bed material is limestone and ash, no sand is used. Normal operating condition is about 60% full load.

Coal is fed into the boiler at two points on opposite sides of the boiler combustion chamber. Mechanical drag conveyors transport the coal to feed pipes which enter the boilers. One point enters the loop seal about 3.05 m

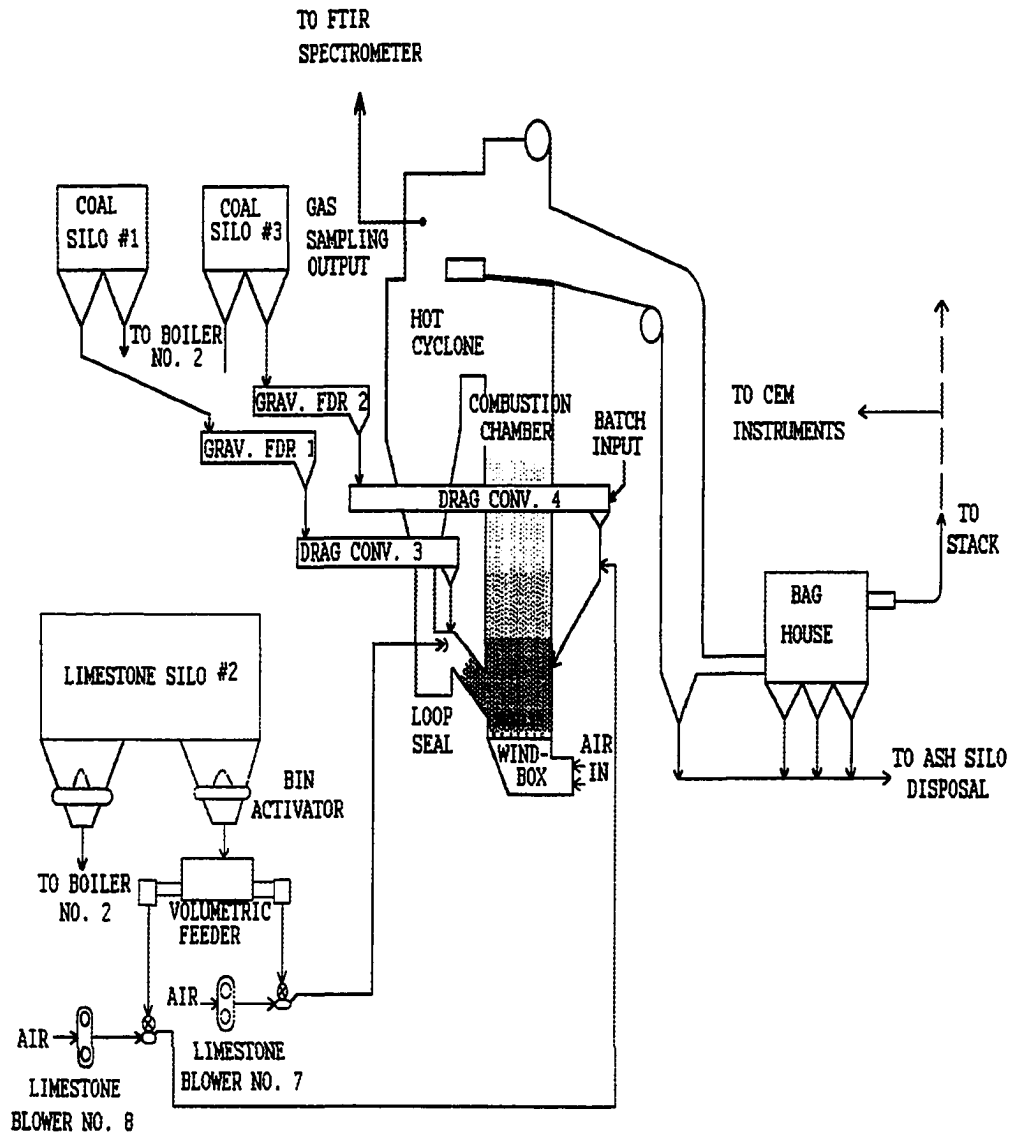


Figure 5.6: Iowa State University Power Plant CFB boiler schematic

from the boiler, the other through a dedicated coal feed point on the opposite side. Both feed points have centerlines about 1.52 m above the nozzles. The two pneumatic limestone feed lines merge with the coal feed lines, and the coal and limestone are fed together. Coal feed rate varied from 5778.8 to 8337 kg/hr (12,740 to 18,380 lb/hr), while total air flow varied from 61,974.3 kg/hr (136,630 lb/hr) to 86,182.5 kg/hr (191,000 lb/hr). The primary to secondary air ratio varied from 1.04 to 1.58. Figure 5.7 shows how the primary to secondary air ratios and total air flow to coal flow ratio varied with total coal feed rate. The general trend is for both ratios to decrease with increased coal feed rate.

The stoichiometric molar air to fuel ratio for the Illinois washed coal was calculated as 3.77. The average molar primary air flow to average fuel feed rate ratio was 3.37, with a low of 3.08 and high of 3.46. Thus, at least initially, the combustion process took place in a condition of slightly less than stoichiometric air flow. The percent change from low to average was 17%, which is significant and could impact the combustion process of the coal batched into the part of the bed below the secondary air inlet.

Devolatilization and char time constants were compared to total air flow and coal feed rate for each test. No direct correlation between air or coal feed rate and time constant could be identified for each size coal. Although one particle size did indicate that time constants were proportional to air or coal feed rates, the trend for another size was inversely proportional. In yet other cases, the relations were totally random. While varying air flow and coal feed rates may influence time constants, there is inadequate data in this work to support any definitive conclusions.

Staged combustion is used in the boilers. Primary air is used in the nozzles and to fluidize the coal feed. Secondary air enters through 4 inlet pipes (two on each side) about

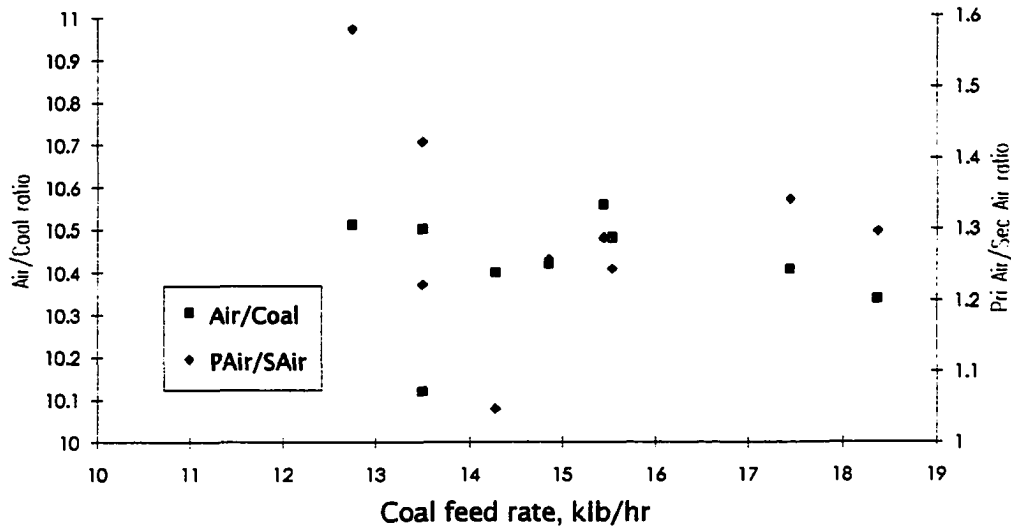


Figure 5.7: Air flow ratios and mass ratio of air flow to coal feed rate

2.74 m above the nozzles, and is also used for the limestone pneumatic feed.

During these tests the boiler was fired with either Illinois washed coal or Kentucky coal, depending on availability.

A sample collection probe (Fig. 5.8) was inserted in a 8.89 cm dia. port installed in the hot cyclone outlet duct. The probe was a 1.22 m long 1.27 cm dia. 316 stainless steel tube surrounded by a 1.588 cm dia. 316 stainless steel pipe for rigidity and erosion protection. The tube and pipe were welded to a 15.24 cm dia. standard flange bolted to the port. The end of the probe was about a third of the way across the cyclone outlet duct and 30.48 cm from the top.

The sample tubing from the probe to the FTIR gas cell is 0.952 cm dia. stainless steel. In-line are a Balston model 30/12 in-line filter with DH element (F1), and two Balston 95S6 miniature T-type filter housings in series, the first

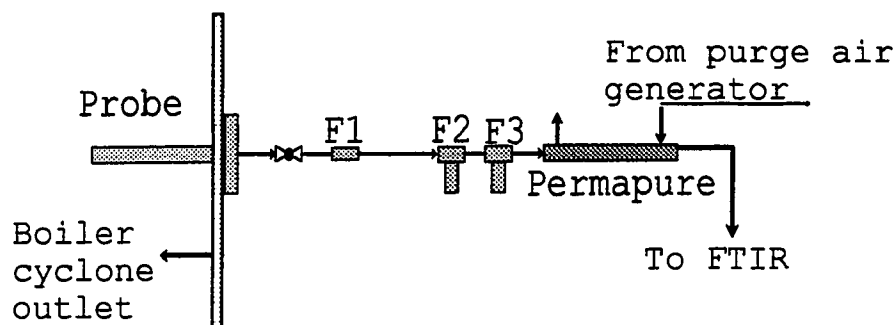


Figure 5.8: FTIR sampling system on Nr. 2 CFB at Iowa State University power plant

with a DH element (F2) and the second with a BH element (F3). The DH elements are rated to remove 93% of 0.1  $\mu\text{m}$  particles and the BH element removes 99.99% of 0.1  $\mu\text{m}$  particles. The filters remove flyash in the sample gas to protect the cell optics and prevent infrared absorption by the flyash particles. Also in-line is a Perma-Pure model PD-1000-48SS membrane air dryer to remove water vapor from the gas sample. The membrane dryer was used rather than condensing out the water vapor to prevent removal of  $\text{SO}_2$  with the water.

A heating unit around the cell is controlled by a Barnant model 621-8600 temperature controller with type J thermocouple and maintains temperature at  $82.2^\circ\text{C} \pm 0.5^\circ$ . A needle valve on the pump inlet is manually adjusted to maintain cell pressure at  $600 \text{ mm Hg} \pm 6 \text{ mm}$ .

The FTIR optical bench, computer, pressure controller, and temperature controllers are housed in a NEMA-12 cabinet with 5000 BTU air conditioning system to maintain temperature about  $21^\circ\text{C}$  and provide a dust free environment.

### 5.6 Coal Feed

The coal batch is introduced into the boiler through a hopper (Fig. 5.9) installed on the outlet end of the coal drag conveyor which dumps into the lower part of the bed opposite

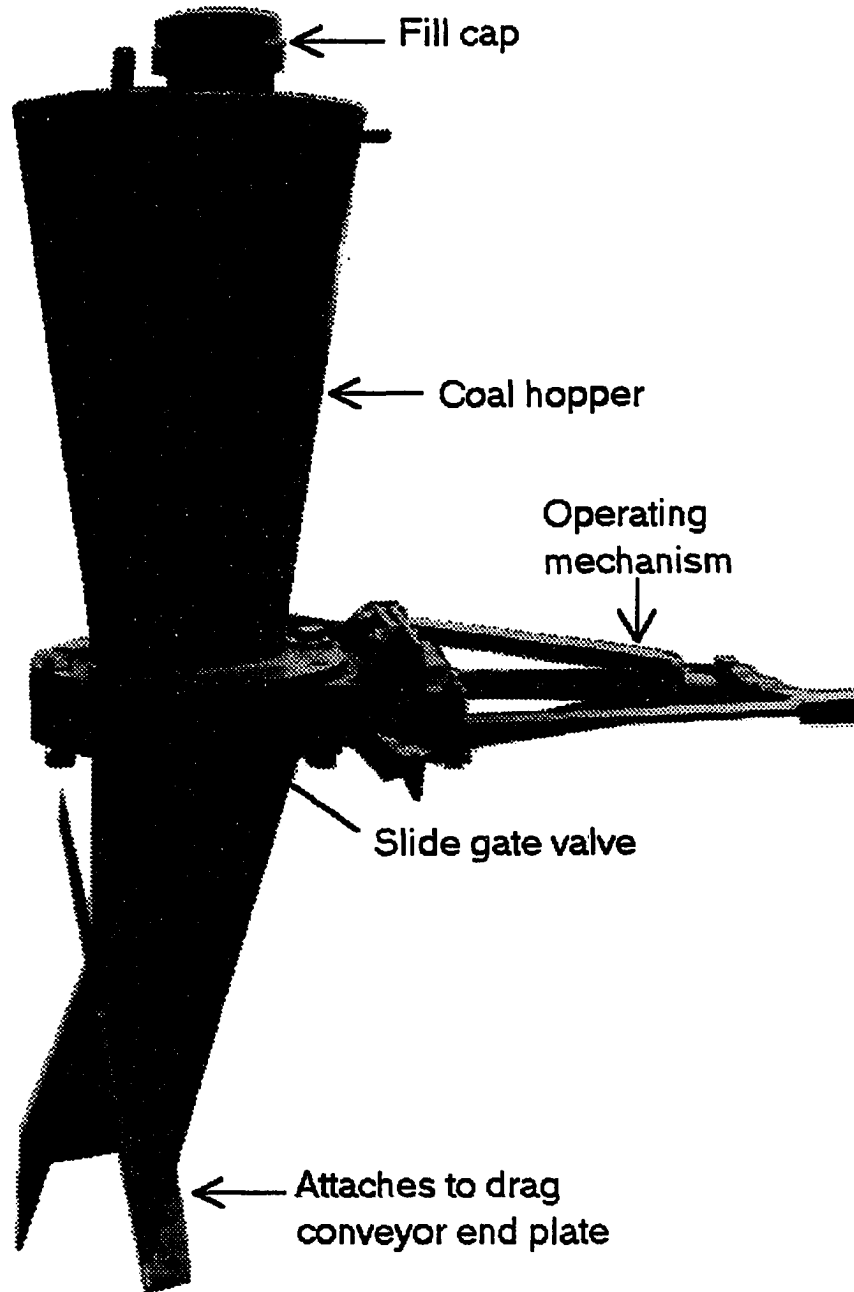


Figure 5.9: Rapid dump coal hopper

the loop seal. The hopper was custom designed to fit the existing coal drag conveyor and dump a batch of coal as fast as the valve could be opened. The hopper is an inverted, truncated conical cylinder on top of a Zurick, Inc. 20.3 cm diameter slide gate valve. The valve has a manual operating mechanism which permits the valve to be opened in less than two seconds. Ducting below the valve directs the coal into the coal feed pipe below the conveyor in such a manner that it is not impeded by the chain of the drag conveyor. Experiments confirmed the coal was dumped as fast as the valve was opened, simulating an impulse input. The hopper was sized to hold up to 13.6 kg (30 lb) of coal, but all tests were performed with 10.9 to 12.7 kg (24 to 28 pounds) of coal, depending on size. The coal was weighed with a Hanson dairy scale, accurate to within 0.11 kg (1/4 pound).

### 5.7 Coal Tested

The types of coal tested were determined primarily by availability. Kentucky coal was used for the laboratory tests, while Illinois washed coal and lignite were tested in the power plant. Table 5.2 lists the proximate and ultimate analyses of these coals. The lignite was provided by Ahlstrom Pyropower. Only 100 kg (220 pounds) was provided, so the number of tests which could be conducted was limited.

As was used by Christofides and Brown [16] and Christofides [17], the laboratory bubbling bed tests were each 5g batches. The following double screened Tyler standard mesh sizes were tested: 3.5x4, 4x5, 5x6, 6x7, 7x8, 8x10, 10x12, 14x16, 16x18, and 18x20.

The particle sizes tested in the CFB boiler at the power plant were chosen to span the range of coal sizes typically burned. The coal is crushed to 0.952 cm (3/8 in.) top size, so that was chosen as the upper limit. The lower limit was chosen as 20 mesh, as this was near the smallest size

Table 5.2, Coal analyses

## Proximate Analysis %

SAMPLE	MOISTURE	ASH	VOLATILE MATTER	FIXED CARBON
Illinois washed coal	3.84	18.67	30.29	47.20
	0.00	19.41	31.50	49.09
Kentucky Coal	6.05	17.24	33.69	43.02
	0.00	18.35	35.86	45.79
Lignite	34.45	30.20	24.16	11.19
	0.00	46.07	36.86	17.07

## Ultimate Analysis %

SAMPLE	SULFUR	C	H	N	O
Illinois washed coal	3.16	61.95	4.07	1.05	11.10
	3.29	64.42	3.79	1.09	8.00
Kentucky Coal	2.82	61.21	4.43	0.97	13.95
	3.00	65.15	3.99	1.03	7.45
Lignite	0.38	24.38	2.36	0.20	42.48
	0.58	37.19	2.28	0.31	13.57

particles (1.0 mm) tested by Christofides and Brown [16].  
Double screened mesh sizes were 3/8"x4, 4x6, 6x8, 8x10, 10x14,  
14x16, 16x18, and 18x20.

## 5.8 Data Acquisition

Gas concentrations were recorded on an Intel 80486  
DXII/66 microcomputer operating with the FTIR optical bench.  
The computer is configured with 8 MB of RAM memory, an SVGA  
monitor, a 420 MB hard drive, and a Colorado Jumbo 250 tape

backup system. The interface to the FTIR bench was through a Nicolet provided bench driver card.

A direct relation exists between number of scans averaged into one spectrum, the resolution, and the time interval between spectra. The higher the resolution, or the more scans recorded, the greater the time interval between spectra. Resolution was set to  $2\text{ cm}^{-1}$  with 2 scans per spectrum, giving a data point every 1.03 seconds using the Nicolet OMNIC series record function. Data was recorded in interferogram format for more rapid recording. GC/IR data collection type was used with no zero fill, and Happ-Genzel apodization. The spectral range recorded was  $4000\text{--}450\text{ cm}^{-1}$ .

A special spectrum, the background spectrum (Fig. 5.10), eliminates signals due to the spectrometer and its environment from the sample. It is a single-beam spectrum obtained without a sample in place and with inert gas or solvent in the

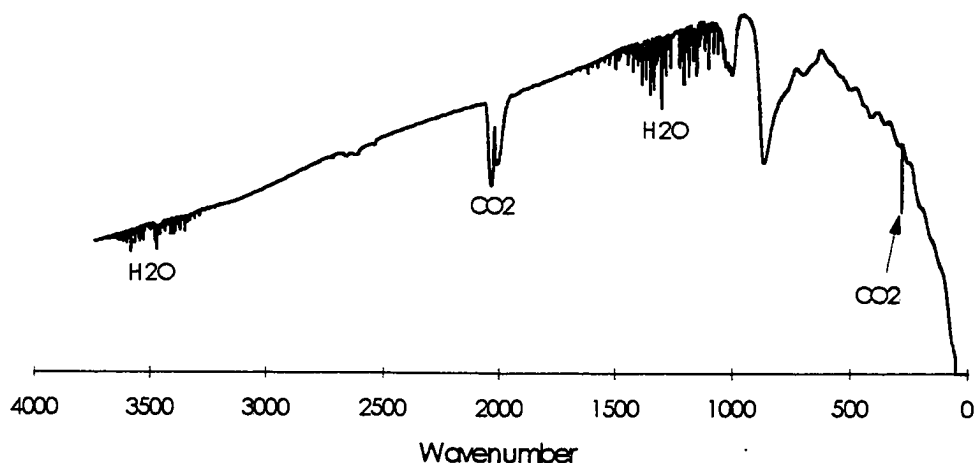


Figure 5.10: Typical single-beam background

cell. The background spectrum is the result of the output of the source; the response of the beamsplitter, optics, and detector; and any atmospheric gases inside the optical bench. Each sample single-beam spectrum is ratioed against the background single-beam spectrum so that the absorptions in the final spectrum are due solely to the sample.

The background spectrum accounts for any CO<sub>2</sub> or water vapor within the IR path inside the bench and for solvent/inert in the cell contained in a sample mixture. The background is automatically subtracted from the sample spectrum when it is taken to remove any artifacts. A background was taken using purge air at 600 mm Hg and 82.2°C prior to each series of tests. This same background was used for all tests in the series, usually 4-5 in a series. Only FTIR spectra were recorded with the computer. Other parameters, such as boiler temperature, average air flow, and average coal feed rate were obtained manually from the power plant Bailey control system following the completion of all test runs. Because of the inability to directly interface with the power plant control system, this data could not be recorded on a real time basis with the FTIR computer. The air flow was measured from a heated foil across the inlet duct to the primary air fan. Coal feed rate was recorded by a mass feed rate instrument.

Tests were run with the master boiler control, oxygen trim, and limestone feed controls in manual. In manual, the air flow, coal feed, and limestone feed rate control signals were fixed and the feeders or fans did not receive any signals to respond to changes in boiler conditions.

After the boiler controls were set, appropriate data was input into the computer and recording was started. Approximately three minutes of steady state background data were recorded before the coal was dumped. Twenty four to

twenty eight pounds of coal, depending on particle size, were put into the hopper and then dumped by rapidly opening and closing the hopper valve. Data was recorded for 8 to 15 minutes, depending on the particle size of the batch.

When recording was completed, the data was reprocessed from interferogram to absorbance format and saved as Nicolet series (\*.SRS) format. A Visual Basic program using Nicolet MACROS/PRO utility (Appendix A) calculated gas concentrations from the series data set. The concentration calculations involved sequentially taking each individual spectrum, subtracting out any water vapor present, performing automatic baseline correct, and using the Quantir quantification methods to quantify the spectra for each of the 6 gases. The concentration and time data were saved in text format. This data was analyzed off-line with Excel, Matlab, or Mathcad, depending on the application.

### 5.9 Data Analysis

Data analysis consisted primarily of taking the CO<sub>2</sub> concentration data and calculating the devolatilization and char time constants. Analysis was conducted in both time and frequency domain, depending on data characteristics. Spectral analysis, applied in the frequency domain, was developed as a tool to evaluate fundamental combustion processes occurring in the combustion system. In applying spectral analysis, it was assumed the combustion processes of devolatilization and char burnout could be modeled as first order linear processes. The basic theory of spectral analysis was developed in Chapter 4.

The calculation of devolatilization and char time constants was based on the assumption that, for short times, the CO<sub>2</sub> profiles for both devolatilization and char burnout regions can be expressed as exponential decays, as expressed in Eq. 2.73.

### 5.10 Time Domain Analysis

Figure 5.11 is a typical batch test in the laboratory bubbling fluidized bed combustor of 5g 7x8 mesh Kentucky coal. The initial rise of the CO<sub>2</sub> signal from the steady state background level to a peak is associated with flow of gas through the system and has a constant equal to the instrument lag time,  $\tau_I$ , measured as 3.02 sec. The devolatilization region is a rapid exponential decay following the peak which transitions smoothly to a slower exponential decay in the char burnout region.  $[CO_2]_i$  is the linear extension of the devolatilization region back to the time  $t_0$  of the CO<sub>2</sub> peak during devolatilization.  $[CO_2]_f$  is the linear extension of the char burnout region back to CO<sub>2</sub> peak time  $t_0$ , and represents the approximately constant contribution of char burnout to the CO<sub>2</sub> signal during devolatilization.

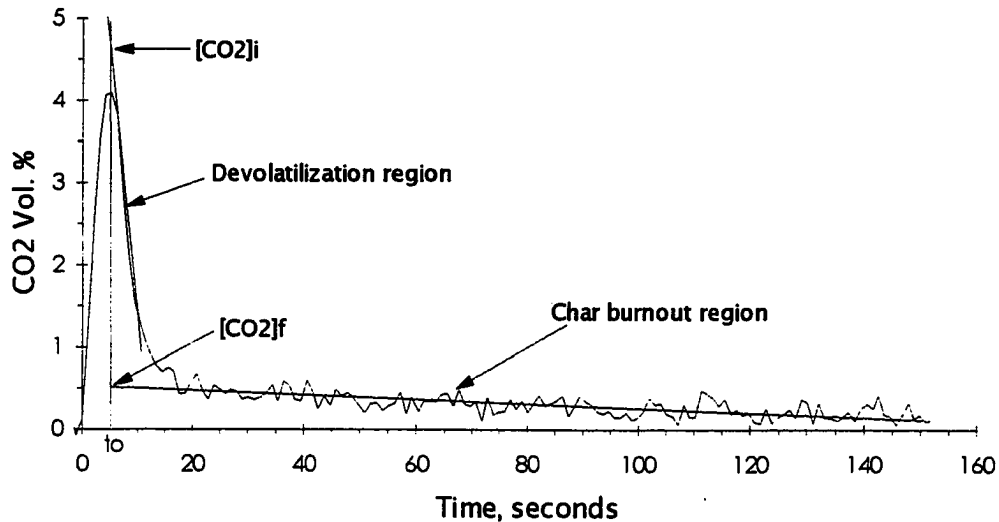


Figure 5.11: Typical CO<sub>2</sub> plot indicating devolatilization calculating parameters

### 5.10.1 Devolatilization time constant

When a batch of coal is introduced into the combustor the CO<sub>2</sub> concentration rises to a peak during devolatilization, followed by a rapid exponential decay, as modeled by Eq. 2.29. Plotting the left hand side of Eq. 5.1 vs. time yields a

$$\ln \frac{[\text{CO}_2]_R - [\text{CO}_2]_f}{[\text{CO}_2]_i - [\text{CO}_2]_f} = -t / \tau_v \quad (5.1)$$

straight line with slope equal to the negative reciprocal of  $\tau_v$ . This assumes the char contribution to the CO<sub>2</sub> concentration is constant  $[\text{CO}_2]_f$  during devolatilization. Figure 5.12 is a typical plot of Eq. 5.1 vs. time for the 5g 7x8 mesh Kentucky coal batch test, showing the linear region over which the slope was calculated. This demonstrates the linearity of the data as plotted, and indicates the data does fit the exponential model for short times, as expected.

The behavior of the CO<sub>2</sub> emissions in the CFB boiler was slightly different than the bubbling bed combustor in the laboratory and necessitated modifying the calculations. As seen in Fig. 5.13, the devolatilization decay does not smoothly blend to the slower char exponential decay, but decays to the background level prior to increasing during char burnout. The background CO<sub>2</sub> concentration has not been corrected to a mean value of zero, as with the laboratory data, due to the larger fluctuations in the background level so as to avoid negative values. It appears from Fig. 5.13 that the char contribution to the CO<sub>2</sub> concentration during devolatilization is negligible, meaning  $[\text{CO}_2]_f$  is zero. Thus the devolatilization equation (Eq. 5.1) becomes:

$$\ln\{[\text{CO}_2]_R / [[\text{CO}_2]_i]\} = -t / \tau_v \quad (5.2)$$

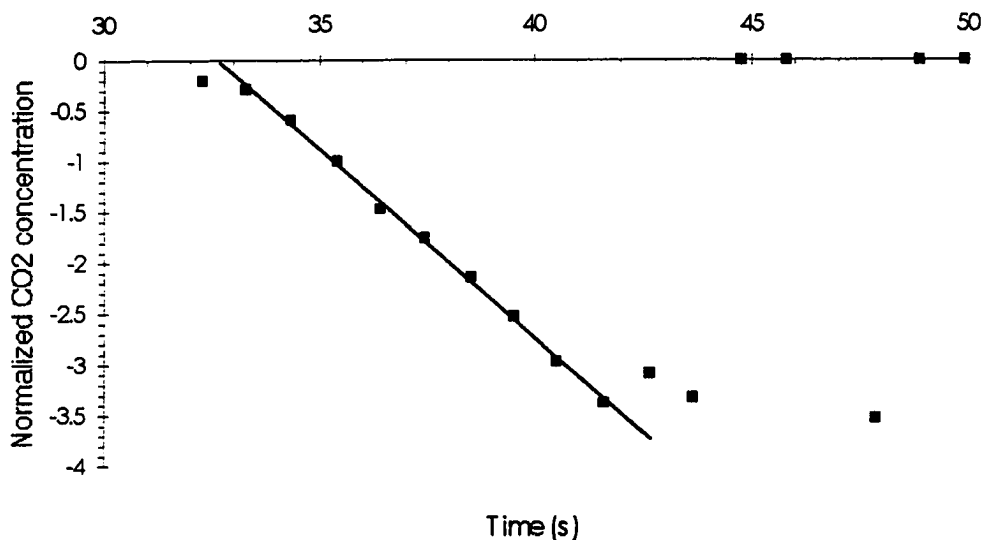


Figure 5.12: Typical plot of normalized CO<sub>2</sub> concentration vs. time, showing region of linearity for calculation of  $\tau_v$

The steady state background CO<sub>2</sub> average for the 60 seconds immediately prior to the batch dump was used as the mean background concentration for determination of [CO<sub>2</sub>]<sub>i</sub> and [CO<sub>2</sub>]<sub>R</sub>. This assumed that char combustion did not begin until devolatilization was complete.

The data was first corrected for pressure deviation from 600.0 mm during the test. For a given gas concentration, pressure variation in the cell can cause variations in absorbance and alter concentration calculations. Due to flyash collection in the sampling line filters, the pressure drop through the system increased slightly during the time of a test, causing the cell pressure to drop. Typically, cell pressure dropped from about 605 mm to 595 mm at the end. Although this variation was less than 1% of the total pressure, CO<sub>2</sub> is sensitive to it because it is so highly

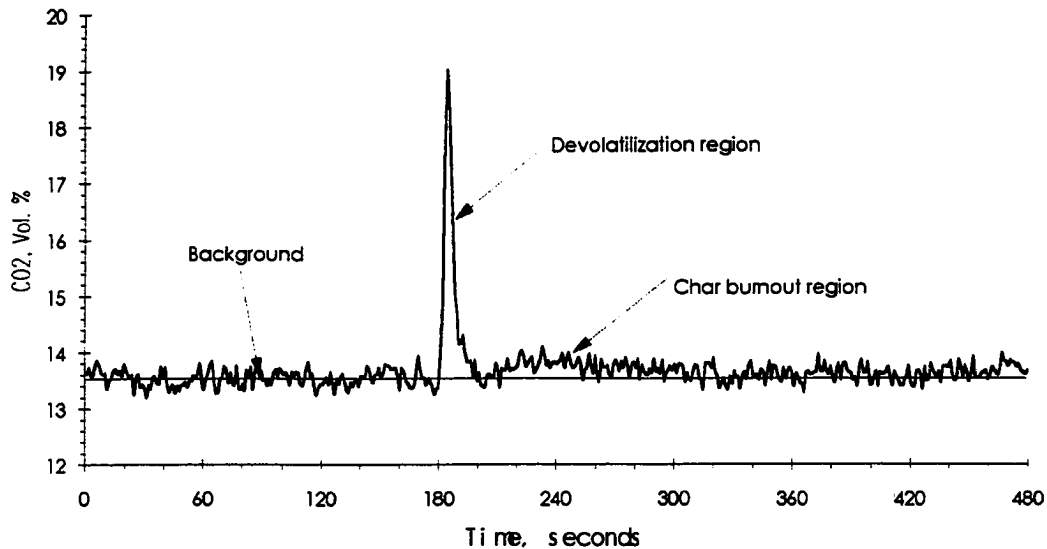


Figure 5.13: Typical profile of CO<sub>2</sub> batch test of 25 lb of 16x18 mesh Illinois washed coal in Iowa State University CFB boiler

absorbing, and the concentration was linearly corrected to a 600 mm Hg value.

Similar to the data from the bubbling bed combustor, Eq. 5.2 was plotted vs. time, giving a plot similar to Fig. 5.12. The negative reciprocal slope of this plot is  $\tau_v$ . This plot for the CFB data was also linear for short times, indicating the exponential model for devolatilization is also valid for the CFB.

#### 5.10.2 Char time constant

Given that for  $t > 3\tau_v$  the char burnout obeys the exponential decay as given by Eq. 2.72 and 2.73, a semilog plot of  $\ln[\text{CO}_2]_R$  vs.  $t$  has a slope of the negative reciprocal of  $\tau_c/3$ . However, this method is very sensitive to any noise in the CO<sub>2</sub> profile since the decay is so slow, and minor fluctuations in the char decay plot can cause sizable

differences in  $\tau_c$  depending on exact points used for the beginning and end of slope calculation. This problem can be decreased by integrating under the  $\text{CO}_2$  curve to give a mass plot, which tends to smooth the fluctuations.

Assuming the particles are spherical and burn with shrinking diameter and constant density, the relationship between particle mass and diameter is represented by Eq. 5.3:

$$\frac{d(t)}{d_i} = \left( \frac{m(t)}{m_i} \right)^{1/3} \quad (5.3)$$

where:

$$\frac{d(t)}{d_i} \approx \exp\left(-\frac{t}{\tau_c}\right) \quad (5.4)$$

Thus, plotting the following relationships should yield a straight line:

$$\ln[(m(t)/m_i)^{1/3}] = -t/\tau_c \quad (5.5)$$

with negative reciprocal slope of  $\tau_c$  for short times.

From Christofides and Brown [16]  $m(t)$  is estimated by:

$$\frac{m(t)}{m_i} = 1 - \frac{Q_{MC}}{m_i} \int_{t=0}^t \left\{ [\text{CO}_2]_R - ([\text{CO}_2]_i - [\text{CO}_2]_f) \exp\left(\frac{-t}{\tau_v}\right) \right\} dt \quad (5.6)$$

This time-integrated approach reduces the impact of noise in the analysis. The total carbon mass from proximate/ultimate analysis minus carbon released during devolatilization from a total mass consumption plot was used as the initial mass of char,  $m_i$ . Figure 5.15 shows a typical plot of  $\ln(m(t)/m_i)^{1/3}$  versus time for a 5g 7x8 mesh coal batch test in the bubbling

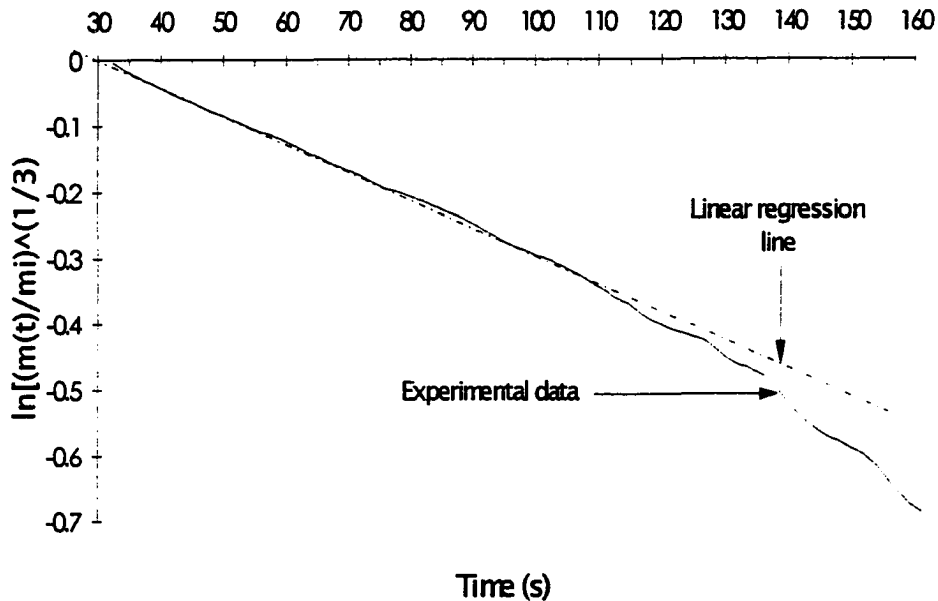


Figure 5.15: Typical plot of  $\ln[(m(t)/m_i)^{1/3}]$  vs. time showing linear region used for calculation of  $\tau_c$

bed combustor, showing the linear region over which  $\tau_c$  was calculated. This figure indicates the assumption of exponential decay for short times of the char burning is valid.

The calculation had to be slightly modified for the CFB boiler data. Because char burnout did not begin until after the completion of devolatilization, Eq. 5.6 was modified to delete the contribution of devolatilization  $\text{CO}_2$  to the total  $\text{CO}_2$  emissions, as shown in Eq. 5.7 and the calculation of  $m(t)$  was not begun until the  $\text{CO}_2$  concentration started to rise at the start of char burnout. In the case of Fig. 5.13,

$$\frac{m(t)}{m_i} = 1 - \frac{QM_C}{m_i} \int_{t=0}^t \{ [\text{CO}_2]_R - [\text{CO}_2]_S \} dt \quad (5.7)$$

the calculation started at time 205 seconds. A plot similar to Fig. 5.15 was obtained, from which  $\tau_c$  was calculated as the negative reciprocal of the slope. This also supports the exponential decay assumption of char burnout for short times in the CFB boiler.

### 5.10.3 Burning rate calculation

Integrating the  $\text{CO}_2$  profile and converting  $\text{CO}_2$  concentration to mass of carbon combusted yields a cumulative carbon consumption curve. This curve, Fig. 5.16, plots amount of carbon (whether from volatiles or char) reacted,  $m_c$ , versus time.

$$m_c = m_t - m(t) \quad (5.8)$$

where  $m_t$  is the total amount of carbon in the sample, and  $m(t)$  is the amount of carbon remaining at time  $t$ .

Figure 5.16 shows three distinct fairly linear regions. The first with the very steep slope is the devolatilization region. The second, immediately following the devolatilization, is the initial char burnout region at times  $t \ll \tau_c$  where the  $\text{CO}_2$  decay is considered exponential. The last region is the latter part of char burnout where the non-linearities exist.

The dashed straight line superimposed upon the initial char burnout region is the region over which  $dm_c/dt$  was calculated. This value, for the entire batch, was divided by the number of particles,  $N$  (Eq. 5.9), to obtain a per particle burning rate.

$$N = 6m_i / \pi \rho_c d_i^3 \quad (5.9)$$

where  $m_i$  is the mass of char at the start of the test and  $\rho_c$  is the density of the coal.

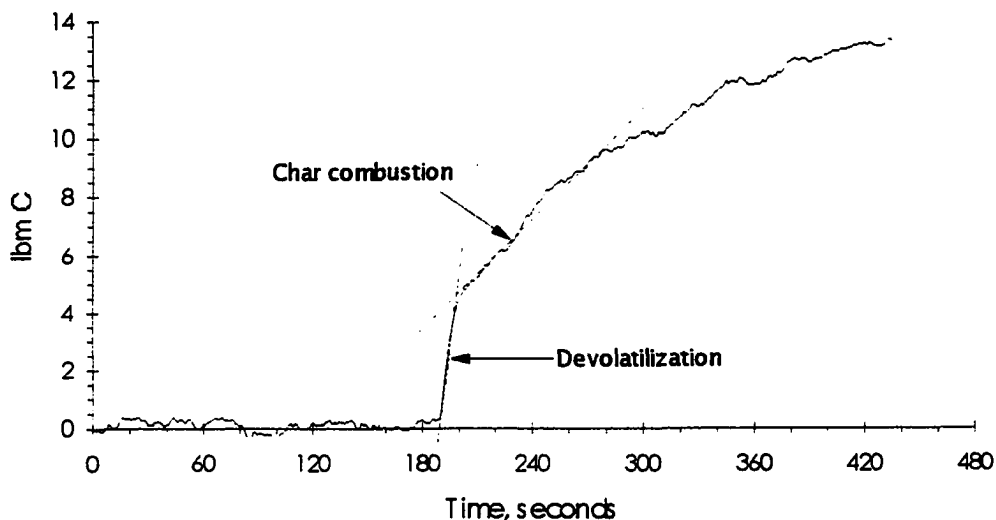


Figure 5.16: Example cumulative carbon consumption plot for 25 lb of 16x18 mesh Illinois washed coal in Iowa State University power plant batch test

From Eq. 5.4 and letting  $\frac{d(t)}{d_i} \approx 1 - \frac{t}{\tau_c}$  and combining with Eq. 5.3, it can be shown:

$$\tau_c = -3m_i / (dm_c/dt) \quad (5.10)$$

With this relationship,  $\tau_c$  can also be simply calculated from the burning rate.

### 5.11 Frequency Domain Analysis

The CO<sub>2</sub> emissions resulting from the dump of a batch of coal into a hot fluidized bed are represented by Eq. 2.73. This takes the form of two first order processes in series. Plotting the PSD as decibels (Eq. 4.16) vs. frequency, calculated as Eq. 4.17, gives a Bode plot. Figure 5.17 is a typical Bode plot for a batch test of 5g 14x16 mesh Kentucky

coal. The cornering frequencies were determined by graphically fitting horizontal and -20 dB/decade asymptotes to the plot, shown as dashed straight lines on the bode plot. The time constants,  $\tau_v$  and  $\tau_c/3$ , are the reciprocals of the cornering frequencies.

Junk [39] used parametric analysis to fit a transfer function to describe the combustion process. His transfer function for large particles is similar in form to what would be obtained if a Fourier transform was applied to the concurrent exponential model, Eq. 2.73, and would have a Bode plot similar to Fig. 5.17.

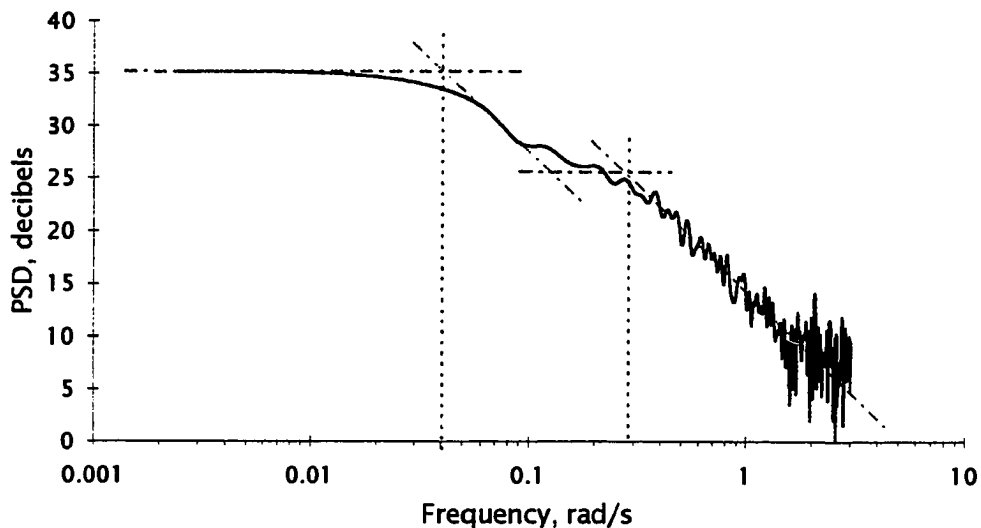


Figure 5.17: Example Bode plot of 5g 14x16 laboratory batch test in a bubbling fluidized bed combustor

## 6. RESULTS

### 6.1 Tests in Laboratory Scale Fluidized Bed

The purpose of the laboratory tests was to verify that the FTIR could duplicate previously run tests and to develop operating procedures for the system. Of specific concern was verification of the ability of the system to sample fast transients.

#### 6.1.1 Spectral features

The FTIR provides the capability to detect all gas species which are visible in the infrared spectrum. Figure 6.1 is a spectrum of the CO<sub>2</sub> peak during devolatilization of a batch test of 5g 8x10 mesh Kentucky coal, with the water vapor subtracted out. This spectrum is typical of the laboratory scale tests. Noticeable amounts of methane (CH<sub>4</sub>), acetylene (C<sub>2</sub>H<sub>2</sub>), and ethylene (C<sub>2</sub>H<sub>4</sub>) are present, in addition to the 6 gases quantified, although the NO<sub>2</sub> is barely perceptible and

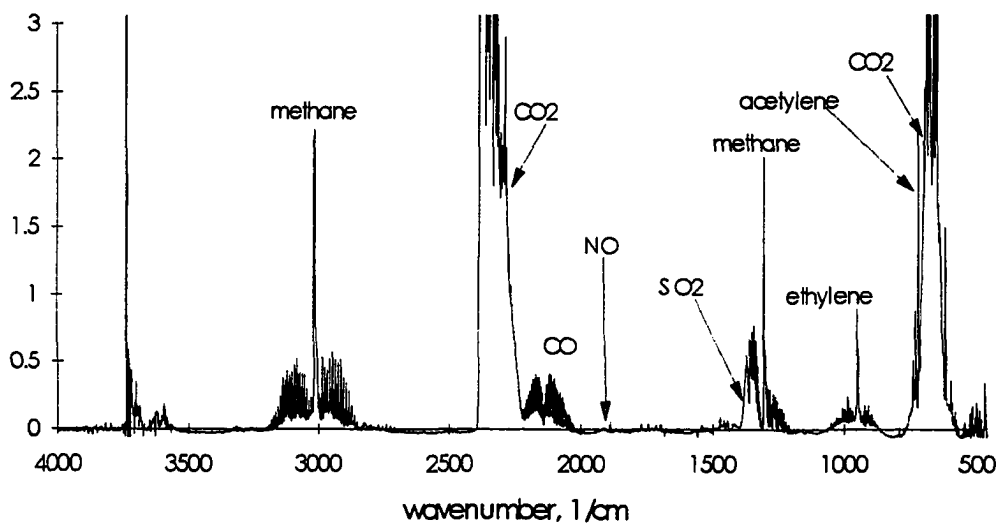


Figure 6.1: Typical spectrum at devolatilization peak

$\text{N}_2\text{O}$  is obscured by methane. Acetylene, a sharp spike at  $720\text{ cm}^{-1}$ , is not clearly visible in this spectrum due to the scale, but is clearly seen if the wavenumber scale is narrowed. No heavy hydrocarbons or tars are visible, only the above mentioned light hydrocarbons. Spectral features of hydrocarbons (primarily methane, acetylene, and ethylene) in the region  $1550\text{-}1200\text{ cm}^{-1}$  obscure  $\text{SO}_2$ ,  $\text{N}_2\text{O}$ , and, to a lesser degree,  $\text{NO}_2$ .

The presence of the hydrocarbons and increased amounts of CO during devolatilization indicate oxygen starvation, at least locally to the coal particles. The increased amounts of hydrocarbons, CO, and  $\text{SO}_2$  were noticed only during the devolatilization region, not during char burnout.

#### 6.1.2 Devolatilization results

Figure 5.11 showed a typical  $\text{CO}_2$  profile from a batch test in the laboratory scale bubbling fluidized bed combustor. Rapid devolatilization decay which smoothly transitioned to a slower char burning decay was clearly seen, as had previously been described by Christofides [17], Christofides and Brown [16], and Junk [39].

It has been shown that devolatilization can be modeled as a fast exponential decay (Eq. 2.29). Various researchers [16,17,25,50,51,52,54] have shown that the devolatilization time,  $t_v$ , can be expressed as a power law relationship with initial diameter, Eq. 2.58.

Figure 6.2 shows a plot of devolatilization time  $t_v$  vs initial particle diameter  $d_i$  for the laboratory scale bubbling bed tests. The devolatilization time  $t_v$  is  $3\tau_v$ , where  $\tau_v$  was calculated using Eq. 5.1. The devolatilization time obeys a power law relationship  $t_v = \alpha d_i^n$  (Eq. 2.58) for particles greater than 3.0 mm initial diameter, which corresponds to the work of previous researchers [16,17,25,50,51,52,54]. For



for comparison. As seen from Fig. 6.2, the devolatilization times of this work closely approximate those of Christofides and Brown [16] and are slightly larger than those of Ragland and Weiss [52] for particles larger than 3 mm. Christofides and Brown [16] attributed differences in particle preparation and shape as reason they and Essenhigh [25] got power law exponents of 2 while Ragland and Weiss got 1.5. Ragland and Weiss [52] used approximately spherical particles, while Christofides and Brown [16] and Essenhigh [25] used crushed and screened coal, which was more cubic or wedged shaped. The coal for this work was prepared similarly to that of Christofides and Brown, so particle shape cannot account for the differences in the power law relationship for this work.

The work of Essenhigh [25] and Ragland and Weiss [52] tested single particles in hot stagnant or flowing air streams, respectively. Pillai [50] and Prins et al. [51] studied devolatilization in a fluidized bed and found  $n$  to vary from 0.83 [50] to 1.7 [51]. Stubington and Linjewile [62] stated that devolatilization rate is predominantly controlled by internal heat transfer, and that fragmentation could cause shorter than expected devolatilization times. Each of the above researchers concluded devolatilization time was independent of coal rank. Prins et al. [51] stated a power law exponent of 1.3 indicated external heat transfer control. The power law exponents determined from studies in fluidized beds tended to be lower than those of Essenhigh [25] and Ragland and Weiss [52] who used single particles in air. The wide variation of values for  $n$  among the noted researchers indicates that many parameters come into play, including the environment in which the parameters were determined.

This work does not exactly duplicate that of Christofides and Brown [16] as the system had been modified in the interim time. The bed material is a mix of 16x20 and 20x30 mesh sand fluidized at 1.2 m/s and heated with natural gas for this

work, as opposed to single size 20x30 mesh fluidized at 1.0 m/s heated with propane for Christofides and Brown [16]. Christofides and Brown [16] used an Indiana V bituminous coal, while this work used Kentucky coal.

It is believed that this work differs slightly from that of Christofides and Brown [16] primarily due to different operating conditions and different coal. The power law exponent of 1.75 is consistent with that obtained by other researchers who did their investigations in fluidized beds.

### 6.1.3 Char burnout results

Char burnout is an order of magnitude slower than devolatilization. Basu [4] and Pillai [50] found the characteristic char burnout time to be proportional to initial diameter squared for diffusion control, and proportional to initial diameter for chemical kinetic control.

The interphase mass transfer time  $\tau_i$  (Eq. 2.70) was determined by testing a range of initial masses (from 2 to 7 g) of the same size particles and plotting the calculated char time constants vs time. Based on Eq. 2.69 and 2.70,  $\tau_i$  is the  $\tau_c$  (calculated from variable mass tests) vs time line extrapolated to  $m_i = 0.0$ . For this work  $\tau_i$  was found to be 20 s.

Normalized char characteristic time ( $\tau_c - \tau_i$ ) was calculated using Eq. 5.5 and then plotted vs initial diameter, Fig. 6.3. The data was found to obey a power law relationship with the exponent  $n$  equal to 1.88 (correlation coefficient 0.914). The regression line of the work of Christofides and Brown [16] is also plotted on Fig. 6.3 for comparison.

This work, using Kentucky coal, is about 30% below that of Christofides and Brown [16] with their Indiana V coal for the smallest size particles tested, and of comparable value for the largest particles. Christofides and Brown [16] determined the power law exponent to be 1.32 for  $\tau_c - \tau_i$ . They

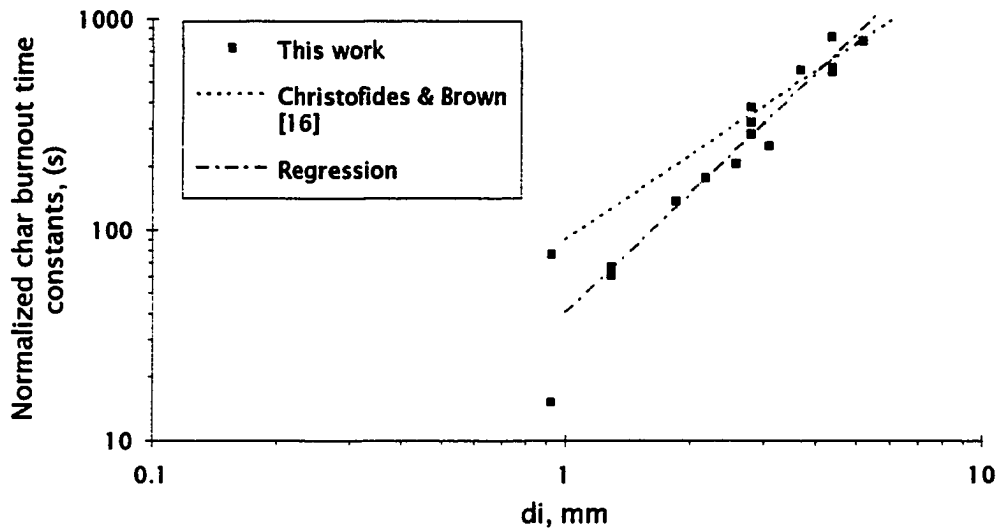


Figure 6.3: Normalized char burnout time vs diameter for laboratory bubbling fluidized bed combustor

theorized this lower than anticipated value was caused by primary fragmentation. The value of 1.88 for this work indicates diffusion control dominates the combustion process, with some primary fragmentation.

## 6.2 Circulating Fluidized Bed Boiler Results

### 6.2.1 Steady state background

Characterization of coal by determination of char and devolatilization time constants assumes the background  $\text{CO}_2$  concentration is invariant with time. In the laboratory scale bubbling fluidized bed combustor operating on natural gas this was true. However, in the on-line power plant CFB boiler this was not the case. Figure 6.4 is a plot of the  $\text{CO}_2$  concentration during steady state operation, with boiler master control,  $\text{SO}_2$  control, and oxygen trim control in manual.

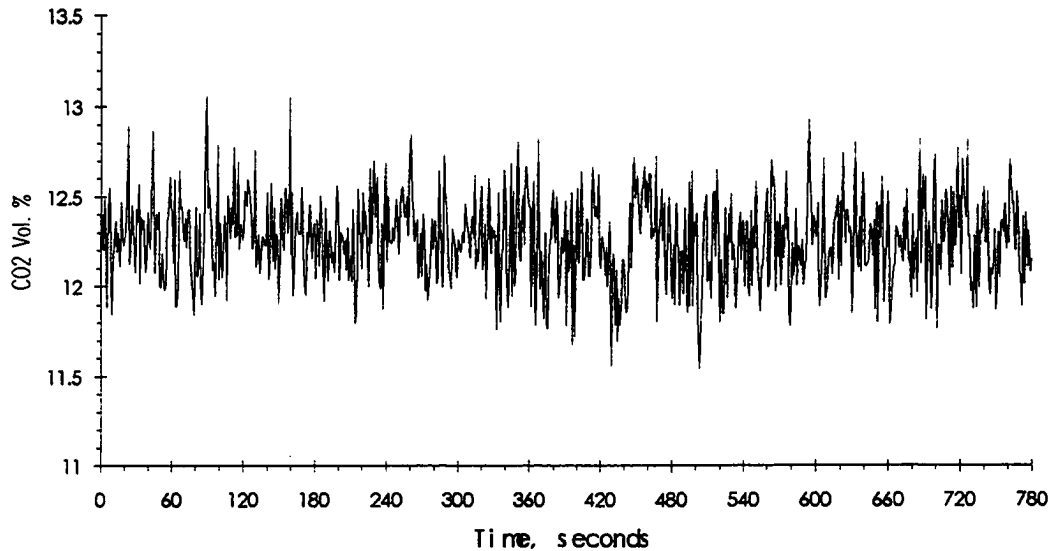


Figure 6.4: Steady state background CO<sub>2</sub> emissions with boiler in manual of Iowa State University number 2 CFB

Fluctuations in CO<sub>2</sub> of approximately 1% molar (peak to peak) are noted. While it appears these fluctuations are white noise, it was shown through flow tests with calibration gas that these fluctuations were not due to system or flow noise, but due primarily to actual fluctuations of CO<sub>2</sub> concentration in the boiler. Dividing the data set in half, and comparing the FFT of the two halves showed a different frequency content for each half. Splitting the data set into three parts and comparing the FFT's of the three parts also showed different frequency content for each part. This showed the fluctuations varied in both amplitude and frequency over time, and thus were not random white noise which would have found no differences in FFT when split into two or three parts. Because these fluctuations were not white noise, averaging and spectral methods, which would be expected to

reduce the affects of noise, were not successful in analyzing the data.

Figure 6.5 shows the plot of the residuals R of the CO<sub>2</sub> concentration (Eq. 6.1) to further demonstrate the magnitude of the fluctuations. The residual fractions of Eq. 6.1 mostly are  $\pm 4\%$ , with a few spikes as large as  $\pm 7\%$ . These fluctuations are not insignificant and influenced calculation of the characteristic times, especially for the largest particles.

$$R = ([CO_2]_R - [CO_2]_{avg}) / [CO_2]_{avg} \quad (6.1)$$

It is believed these background fluctuations are caused primarily by slight variations in the mechanical feed of coal to the boiler and secondarily due to slight fluctuations in air pressure. The mechanical drag conveyor consists of steel plates 5 cm high by 45 cm wide which are pulled by a chain

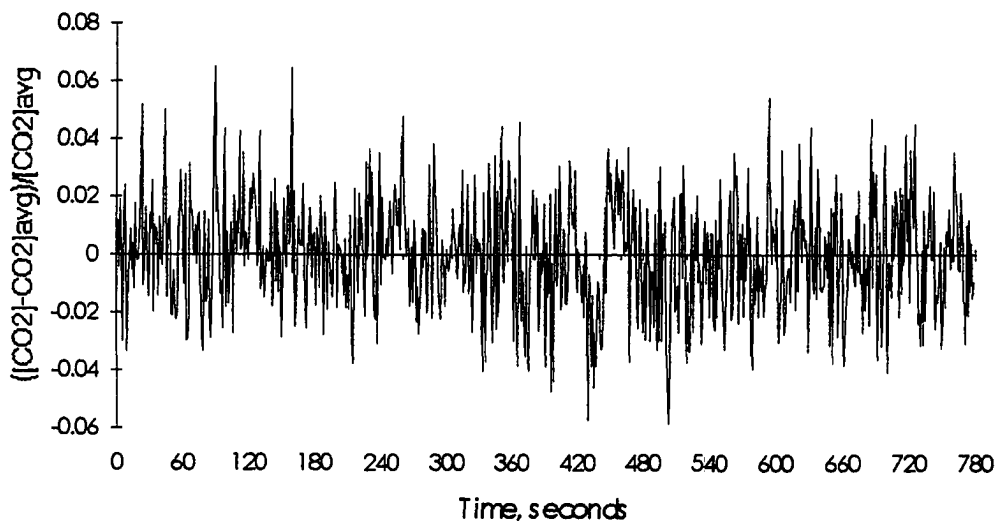


Figure 6.5: Iowa State university power plant CFB boiler steady state CO<sub>2</sub> residuals

through the rectangular trough conveyor. The speed of the conveyor is such that a plate passes over the end opening where coal is dumped every 2-4 seconds, which approximately corresponds to the frequency of the fluctuations. It is theorized the coal falls into the opening as discrete batches or particles, rather than continuous smooth flow. Sundback et al. [63] noted high frequency fluctuations in the CO<sub>2</sub> emissions burning char. They attributed these fluctuations to secondary fragmentation of the char. It is believed the steady state CO<sub>2</sub> concentration fluctuations are primarily caused by the mechanical coal feed, with a lesser influence from secondary fragmentation of the burning char.

#### 6.2.2 Spectral features

As with the laboratory scale results, the spectral features are very informative. Fig. 6.6 is a spectrum at the CO<sub>2</sub> peak during devolatilization of an 11.34 kg (25 lb) batch of 16x18 mesh Illinois washed coal in the Iowa State University CFB boiler. The only hydrocarbon seen in this spectrum is methane, as opposed to methane, acetylene, and ethylene in the bubbling bed combustor. The methane, CO, and SO<sub>2</sub>, peaked only during the devolatilization region. Methane and CO were present only during devolatilization of the smaller particles, and were not present at all (except for very small background level of CO) in tests of the larger particles. The lack of methane and CO peaks during devolatilization for the larger particles is attributed to the slower devolatilization for them and less demand for O<sub>2</sub>. The batches were kept as small as possible, consistent with getting a significant CO<sub>2</sub> peak during devolatilization, to reduce the interference between methane and SO<sub>2</sub>. This would indicate, that at least locally to the particles, there was inadequate oxygen present for complete combustion during devolatilization of the smaller particle sizes.

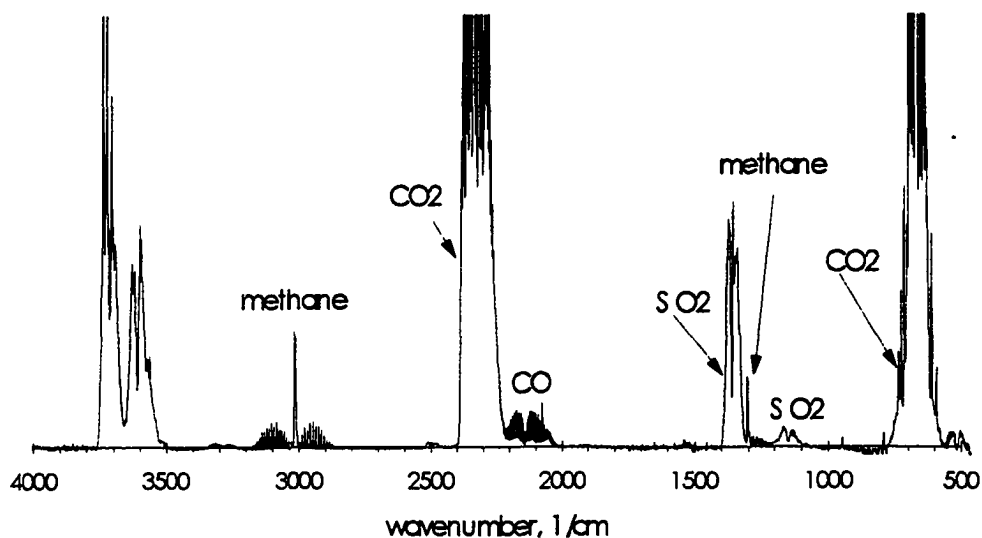


Figure 6.6: Spectrum of the  $\text{CO}_2$  peak during devolatilization of a batch test of 25 lb 16x18 mesh Illinois wash coal in the Iowa State University power plant Nr. 2 CFB boiler

After completion of these tests, the boiler was opened by plant maintenance personnel for inspection. It was noted that there was an area of about 10 cm thick "sintered coal" in a 1.2 m diameter circle around the coal inlet pipe where the test coal entered the boiler. This sintered coal was easily brushed off and appeared to have no adverse affects upon the boiler or its operation. Unfortunately, plant personnel did not save any of this material for closer examination. This material had not been seen prior to any of these tests during the life of the boiler. It is theorized that local reducing conditions around the coal inlet point from the batches dumped in during normal operation caused this material.

Methane release occurred during a very short period (no more than 10 seconds) of the devolatilization region, as shown in the Fig. 6.7 chemigram of the methane spectral region for a batch test of 11.34 kg (25 lb) of 16x18 mesh coal. A

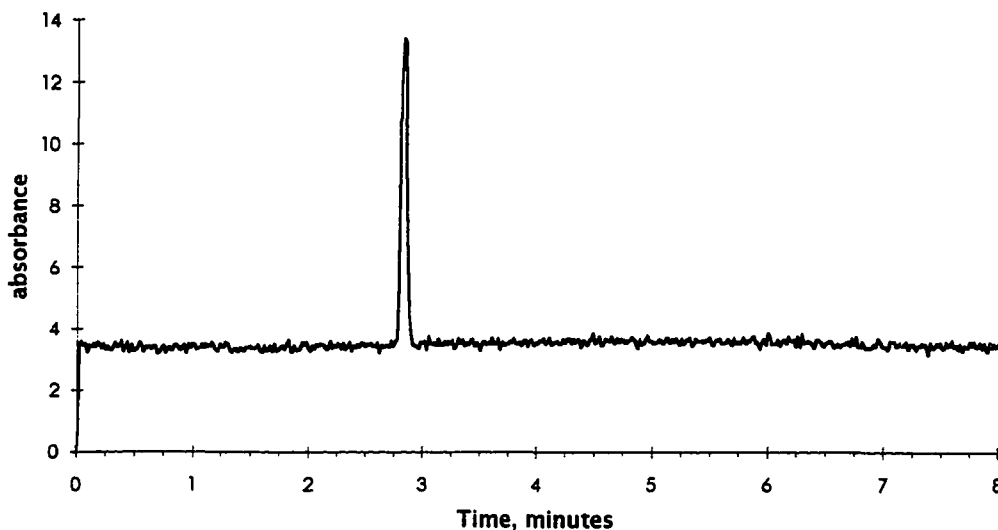


Figure 6.7: Chemigram of methane spectral region of batch test of 25 lb of 16x18 mesh Illinois washed coal in ISU power plant CFB boiler

chemigram is a special reconstruction showing the infrared response over a specified spectral region as a function of time. This figure is typical of the cases where methane was generated. The y-axis scale is arbitrary and has no physical meaning, other than comparing relative amplitudes within the same chemigram.

### 6.2.3 Devolatilization results

A rapid devolatilization decay profile following a fast rise during heating, similar to that seen in the laboratory scale bubbling bed, was seen for all batch tests. Figure 5.13 is a typical  $\text{CO}_2$  profile obtained for a batch test of 11.34 kg (25 lb) of 16x18 coal in the Iowa State University CFB.

Devolatilization time  $t_v$  ( $3\tau_v$ ) was plotted vs initial particle diameter (Fig. 6.8). A power law dependence upon diameter was evident for all particle sizes. The exponent was

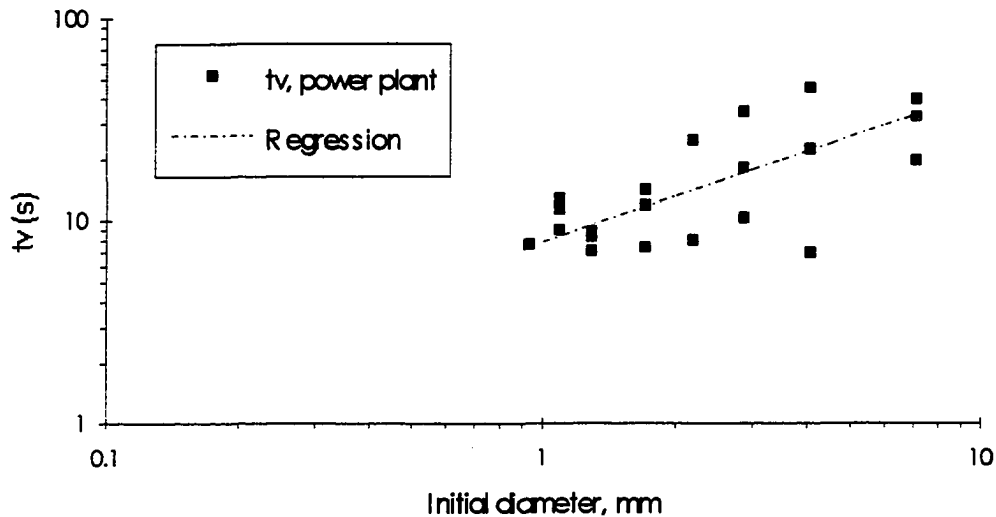


Figure 6.8: Plot of devolatilization time  $t_v$  vs dia for Iowa State University CFB data

calculated to be 0.73 (correlation coefficient 0.527). The lower limit of 9 s seen on  $t_v$  in the bubbling bed data caused by the system lag time is not seen with the CFB data due to a shorter system lag time, calculated as less than one second from step tests of tracer gas. More scatter in the plot is evident than what was seen from the laboratory data, especially for the larger particles. This is believed to be caused by the influence of the background fluctuations upon  $t_v$  calculations, and explains the rather poor correlation coefficient. In Appendix C the uncertainty of  $t_v$  for the CFB data is calculated to be 38%, due largely to the background fluctuations.

All data points in Fig. 6.8 fall within the uncertainty, except for the largest  $t_v$  values measured for particle diameters 2.19, 2.87, and 4.04 mm, and the lowest  $t_v$  for particle diameter 4.04 mm. However, the high and low data points at 2.19, 2.87, and 4.04 mm diameter are approximately

equidistant from the regression line. For the largest particles the ratio of the CO<sub>2</sub> peak during devolatilization, [CO<sub>2</sub>]<sub>i</sub>, compared to the steady state CO<sub>2</sub> background level, [CO<sub>2</sub>]<sub>avg</sub>, ( $[\text{CO}_2]_i/[\text{CO}_2]_{\text{avg}}$ ) is of the same order of magnitude as the residuals, Eq. 6.1.

### 6.2.3 Char results

Both CO<sub>2</sub> profiles and cumulative carbon consumption plots indicated that char burning did not start until the completion of devolatilization. This is in concurrence with Saxena [54] and Ragland and Weiss [52], but disagrees with Christofides and Brown [16], who deduced that devolatilization and char burning occurred simultaneously in a bubbling fluidized bed. The laboratory scale results for this coal also seem to indicate simultaneous devolatilization and char burnout in the bubbling fluidized bed. Decay of CO<sub>2</sub> concentration to background level prior to rising slightly a few seconds later was the prime indicator of the delay of the beginning of char burnout. This is believed to be the result of slower heating of the char particle in the CFB as opposed to the bubbling bed since the heat transfer coefficient is lower in a CFB.

Figure 6.9 compares the results of batch tests of 4x6 mesh Illinois washed coal in the bubbling bed (solid line) and the CFB boiler. In Fig. 6.9 the gradual transition from devolatilization to char burnout for the bubbling bed test is clearly seen, while the CFB CO<sub>2</sub> devolatilization goes to the background level prior to rising slightly for char burnout. While a region of char burnout is clearly seen for the bubbling bed profile, it is less distinct for the CFB.

From a qualitative viewpoint, it appears from this result that the devolatilization process is rapid in both cases, but that char burnout is significantly slower in the CFB than in the bubbling bed and does not begin until devolatilization is complete.

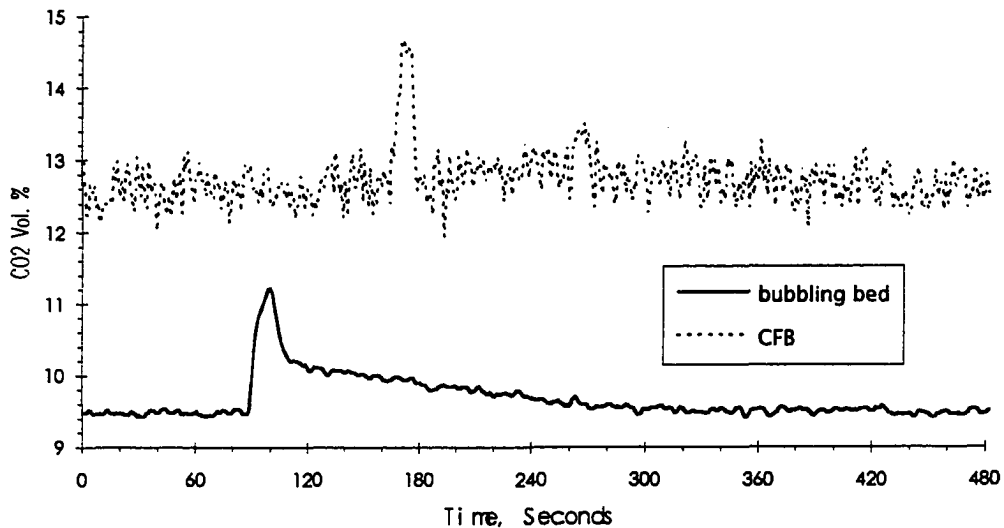


Figure 6.9: Comparison of 4x6 mesh Illinois washed coal batch tests in bubbling bed combustor and CFB boiler

While the ratio  $[CO_2]_f/[CO_2]_i$  for the laboratory data was as large as 0.5 for the smallest particles, it was never greater than about 0.125 for any batch tests in the power plant CFB boiler. All the combustion air for the bubbling bed enters at to bottom, while the combustion air in the CFB enters in two stages: 50-60% as primary air mainly through nozzles at the bottom of the boiler, and the rest as secondary air at points above the coal injection point. In the range of primary to secondary air flow ratios at which these tests were conducted, no definitive trend could be established regarding influence of air staging upon combustion dynamics because only one sampling point at the cyclone outlet was available.

For short times a plot of  $\ln(m(t)/m_i)^{1/3}$  vs time was a straight line, indicating the exponential model was valid over these time intervals. Both burning rate per particle and char time constant  $\tau_c$  were plotted against initial diameter,  $d_i$ .

Figure 6.10 shows  $\tau_c$  plotted vs  $d_i$ , indicating an increase in  $\tau_c$  with diameter. The large degree of scatter of  $\tau_c$  for the two largest particle sizes is believed due to the size of the background fluctuations compared to  $[\text{CO}_2]_f$  as well as to the very slow exponential decay of char burnout. A power law relationship for  $\tau_c$  as a function of diameter gives the exponent  $n = 0.54$  (calculated as  $\ln(m(t)/m_i)^{1/3}$ ), correlation coefficient 0.317) or 0.55 (calculated as  $-3m_i/(dm_c/dt)$ , correlation coefficient 0.369). The poor correlation coefficients are indicative of the influence of the fluctuating background upon the calculation of  $\tau_c$ , although the uncertainty analysis of Appendix C shows the uncertainty in  $\tau_c$  was expected to be only 9.8%.

Christofides and Brown [16] showed that the characteristic time  $\tau_c$  is representative of the char burning time  $t_b$ . The characteristic time will be proportional to  $d_i^2$  for diffusion control and proportional to initial diameter  $d_i$

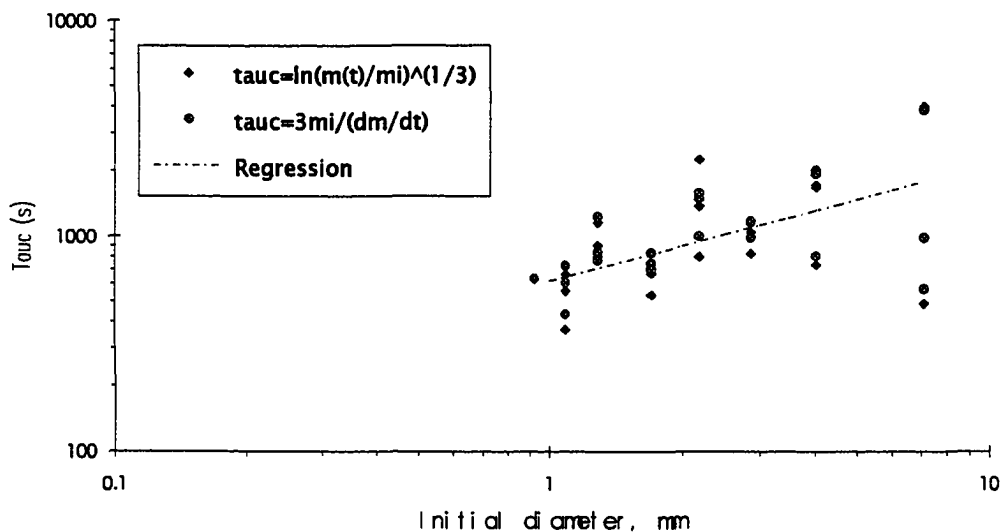


Figure 6.10: Characteristic char time constant vs initial diameter for power plant data

for chemical kinetics control [2,35,67]. A power law exponent less than 1 indicates other factors are present.

Following the analysis of Christofides and Brown [16], the power law found in the present study can be shown to be consistent with fragmentation of particles under chemical rate-limited char combustion. Fragmentation is assumed to produce  $N_f$  spherical fragments of diameter  $d_f$ , which is a simplification of the fragmentation process, but follows the data of Chirone et al. [15]. The number of fragments is expected to increase with particle size. The diameter of the fragmented particles can be related to the initial diameter of the particles by:

$$\frac{d_f}{d_i} = \left( \frac{1}{N_f} \right)^{\frac{1}{3}} \quad (6.2)$$

If a linear dependence of  $N_f$  upon  $d_i$  is assumed in Eq. 6.2, then [15,25,62]:

$$d_f \propto d_i^{2/3} \quad (6.3)$$

For chemical kinetics control with constant Sherwood number  $\tau_c \propto d_i$ . Considering char burning under chemical kinetics control with fragmentation, the apparent power law is:

$$\tau_c \propto d_i^{2/3} \cong d_i^{0.67} \quad (6.4)$$

This result is in agreement with the power law exponent of 0.54 to 0.55 found in the present study. The burning rate calculation is the change in carbon mass per unit time as the particle burns. A log-log plot of burning rate per particle vs initial diameter is shown in Fig. 6.11.

The results of Basu [4], for 4-10 mm particles, are shown for comparison. For this range of particle sizes, this work and the work of Basu [4] are the same order of magnitude. A linear relationship is clearly evident, indicating a power law relationship between burning rate per particle and initial particle diameter applies. The power law exponent is 2.58 (correlation coefficient 0.965). Basu [4] studied the burning rate of carbon spheres in fluidized bed of sand at 800°C and found a power law exponent of 1.52 to apply. He concluded the burning rate was primarily diffusion controlled for his 4-10 mm particles.

Applying the same analysis for fragmentation as was done for the char time constant and assuming chemical kinetic control, the power law exponent is found to be 2.33:

$$dm_C/dt \propto d_i^{7/3} \cong d_i^{2.33} \quad (6.5)$$

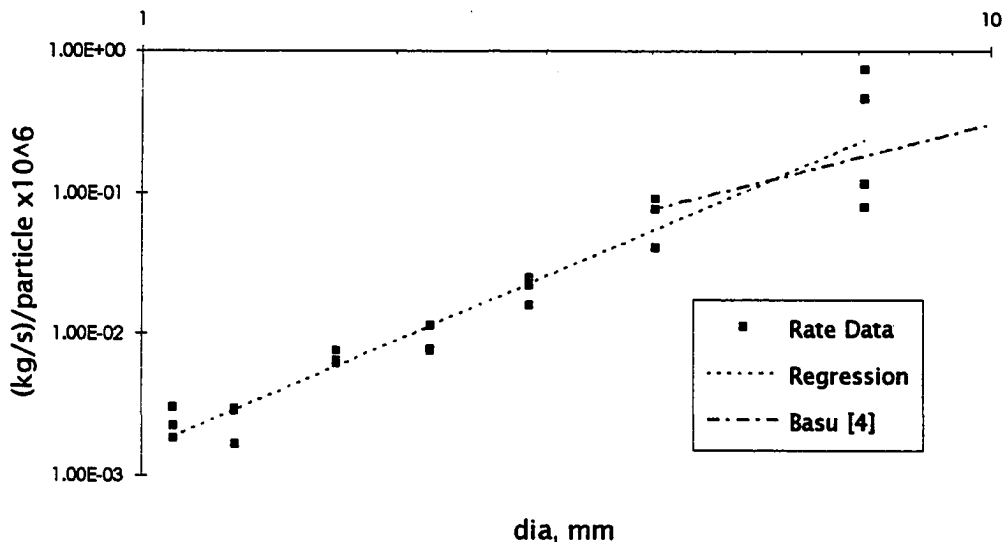


Figure 6.11: Burning rate  $dm_C/dt$  per particle vs initial particle diameter

This suggests that the burning rate for this work is chemically kinetic controlled with primary fragmentation, as was found for the characteristic char time.

#### 6.2.4 Lignite tests

A limited amount of lignite was available for testing. Due to the limited amount of lignite provided, the batch sizes were smaller than desired, and the screen size differences wider than desired. The amounts and size ranges tested were: 6.8 kg (15 lb) of 14x20 mesh, 9.4 kg (20.7 lb) of 8x14 mesh, 11.3 kg (25.0 lb) of 4x8 mesh, and 10.5 kg (23.25 lb) of greater than 4 mesh. As noted from table 5.2, the lignite has considerably more ash, less volatile matter, and less fixed carbon than the Illinois washed coal. Accordingly, it was expected that the devolatilization peak would be smaller and the char burnout even less visible than the Illinois washed coal. Also, the lignite particles were not spherical for any particle size intervals, in contrast to the roughly spherical Illinois washed coal. Although smallest lignite particles were roughly spherical, those greater than 4 mesh tended to consist of many long, thin, flat plates. With greater surface area per volume, the particles are expected to devolatilize and burn faster than the more spherical particles.

Figure 6.12 is a plot of the CO<sub>2</sub> concentration vs time for the 4x8 mesh batch test of lignite. A distinct devolatilization peak is evident, but it is quite small and there is no visible char burnout above the background CO<sub>2</sub> concentration following the devolatilization. With smaller than optimum batch sizes and less volatile matter than the Illinois washed coal (24.16% vice 30.29%) the small devolatilization peak was not surprising. Because there was no distinct evolution of CO<sub>2</sub> above the background level during the expected char region, no calculation of char time constants was possible.

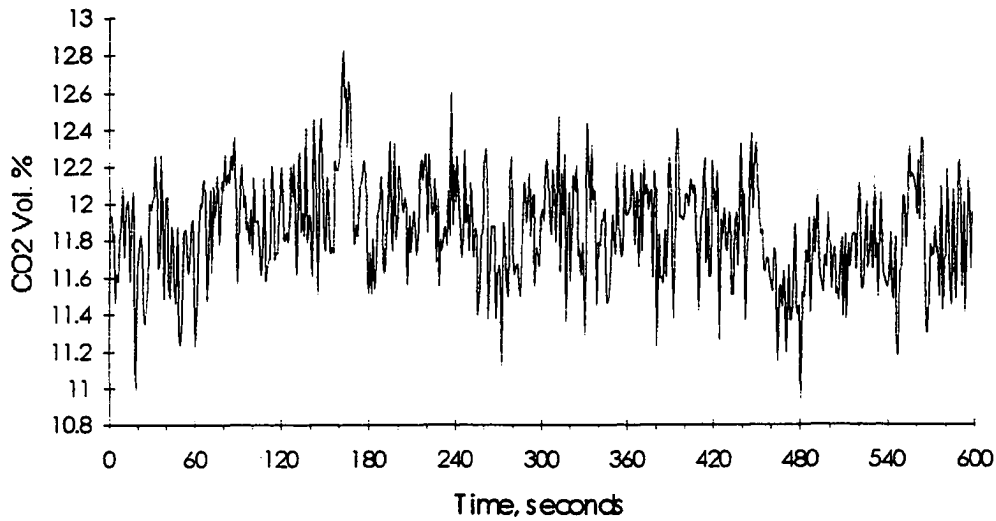


Figure 6.12: CFB boiler CO<sub>2</sub> concentration vs time for 25 lb 4x8 mesh lignite coal batch test

Devolatilization time constants  $\tau_v$  were calculated and devolatilization times ( $3\tau_v$ ) are plotted vs initial diameter in Fig. 6.13. The linear regression line of the Illinois washed coal devolatilization time vs diameter is shown as a dashed line. There is a trend for  $t_v$  to increase with initial diameter, with power law exponent  $n=0.423$  (correlation coefficient 0.902). This is an excellent correlation, although based on only a limited number of data points. The fact that the Illinois washed coal and the lignite have similar  $t_v$ , even though the lignite has less volatile matter, suggests that heat and mass transfer determine the rate of devolatilization.

### 6.3 Spectral Analysis

#### 6.3.1 Laboratory scale bubbling fluidized bed

Spectral analysis was developed as a new method to analyze the CO<sub>2</sub> concentration data and calculate the devolatilization and char time constants. Figure 6.14 is a



Bode plot of a batch test in the bubbling bed combustor test of 5g of 14x16 coal. This Bode plot is consistent with a dynamic system consisting of two linear processes in series.

This plot supports the validity of the combustion model of Eq. 2.73 with the two concurrent exponential decays. The cornering frequencies as shown give  $\tau_v = 1/0.29 = 3.4$  sec, and  $\tau_c = 3/0.040 = 75.0$  sec. These values differ from values calculated in the time domain by only 6%. Appendix A contains the Matlab program used to perform the calculations and plot the data.

Figures 6.15 and 6.16 plot the devolatilization times,  $t_v$ , and char time constants,  $\tau_c$ , vs initial diameter, respectively for the bubbling fluidized bed data as calculated using spectral analysis. Also plotted on these figures are the linear regression lines for  $t_v$  and  $\tau_c$  calculated using time domain methods and discussed earlier. As had been noted with the time domain analysis, the devolatilization time for diameters less than 3.0 mm are independent of diameter, and are constrained by the system lag time,  $\tau_l$ . For initial particle diameters less than 4 mm, there seems to be good correlation between the spectral analysis and time domain calculations. At larger diameters the time constants calculated with spectral methods are about 2/3 of the time domain values.

The char time constants calculated with spectral methods correspond fairly well with time domain methods for diameters less than about 2 mm, but fall further below the time domain values as diameter increases. Chapter 4 discussed the limitations with spectral analysis that a data set of minimum length must be taken before performing spectral analysis, or erroneous results could be obtained. For the bubbling bed tests of this work all tests were approximately 2-3 minutes in length, which is adequate for time domain analysis. The time

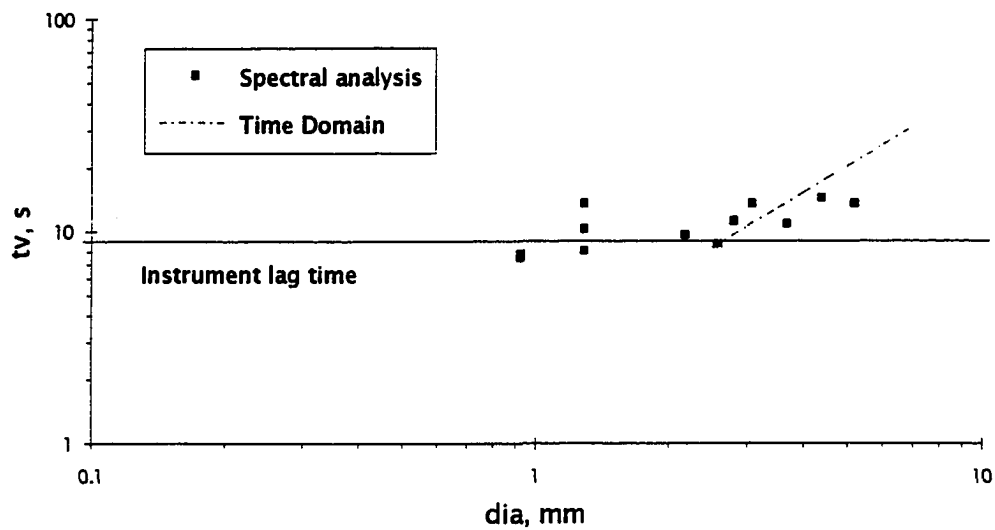


Figure 6.15: Plot of devolatilization time  $t_v$  obtained by spectral analysis for bubbling bed batch tests

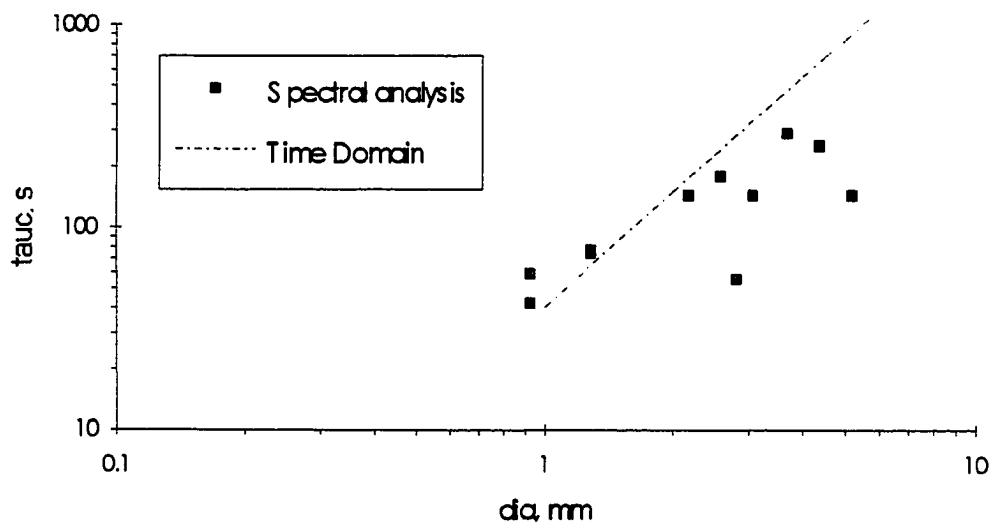


Figure 6.16: Plot of char time constant vs diameter as calculated with spectral methods

interval for the smallest particles was adequate for proper spectral analysis, but proved too short for larger particles.

Figure 6.17 is a Bode plot of a 5g 6x7 mesh coal batch test in the bubbling bed combustor. From the cornering frequencies,  $\tau_v = 1/0.34 = 2.9$  (compared to 2.69 from time domain analysis) and  $\tau_c = 3/0.017 = 176.5$  (compared to 238 from time domain analysis). This clearly shows that despite the distinct cornering frequencies, the char time constant calculated is significantly less than that calculated from time domain analysis.

Spectral analysis of all batch tests were not as successful as the example of Fig. 6.14 because not all data sets had an adequate length to ensure proper determination of  $\tau_c$ , as demonstrated by Fig. 6.17. However, the results obtained in this work demonstrate that spectral analysis will yield results comparable to time domain results when the data set time length is adequate.

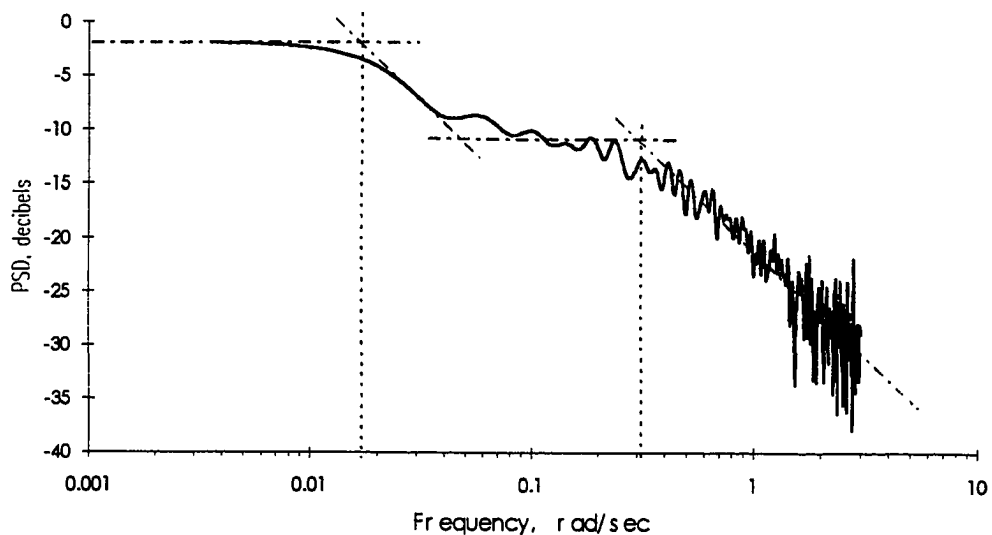


Figure 6.17: Bode plot of 5g 6x7 mesh batch test in the bubbling bed

### 6.3.2 Industrial scale CFB boiler

The CFB boiler batch test data was analyzed using spectral methods in the same manner as the laboratory scale combustor data. Figure 6.18 is a typical Bode plot for a 25 lb batch test of 14x16 mesh coal. There is an excessive amount of "noise" at the higher frequencies due to the background fluctuations. Because of this the transition from horizontal to the -20dB/decade slope of devolatilization region is very difficult to observe. From the asymptotes of Fig. 6.18  $\tau_v = 1/0.31 = 3.2$  (compared to 5.97 for time domain analysis) and  $\tau_c = 1/0.0057 = 175$  (compared to 987 for time domain analysis). It is believed the high frequency fluctuations and shorter than optimum time interval are primarily responsible for the low characteristic times calculated from spectral analysis.

Digital filtering, windowing, and averaging techniques were unsuccessful in reducing the noise to improve the visibility of the cornering frequency. Because the effects

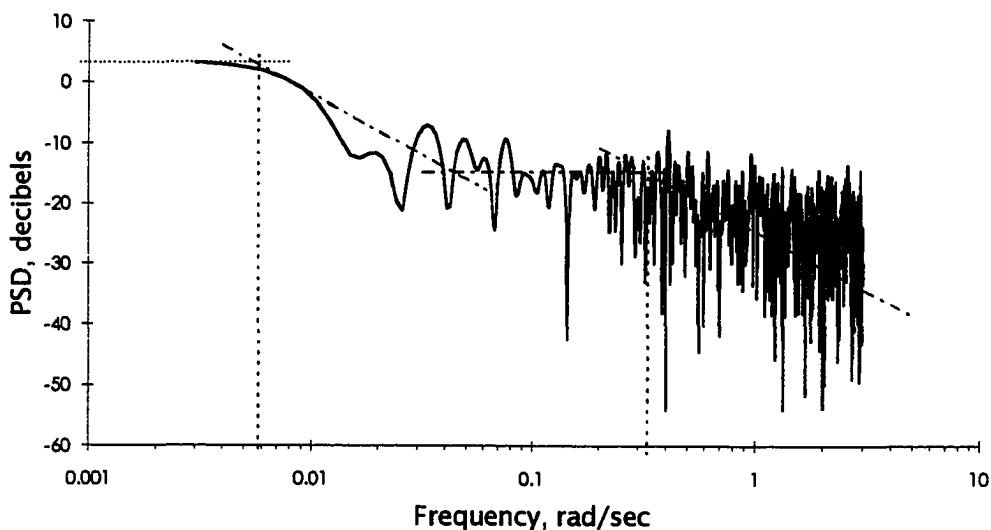


Figure 6.18: Bode plot of 26 lb 6x8 batch test in CFB boiler

of the background fluctuations could not be removed from the analysis, meaningful analysis of the CFB boiler data using spectral analysis was not possible. Had the background fluctuations been more ergodic, it is believed spectral analysis would have been as successful with the CFB data as with the bubbling bed data.

#### **6.4 Pollutant Formation**

The focus on this research was evaluation of coal combustion properties based upon analysis of CO<sub>2</sub> emissions. While rigorous quantitative studies of pollutant gases (CO, SO<sub>2</sub>, NO, NO<sub>2</sub>, and N<sub>2</sub>O) were not undertaken, limited qualitative evaluations were performed for these gases during transient tests.

##### **6.4.1 Carbon monoxide**

Carbon monoxide emissions result from incomplete combustion of coal. Carbon monoxide levels were quite low during steady state operation, but increased rapidly to a peak and then rapidly decayed to the background level during devolatilization of small particles. Figure 6.19 shows the CO profile for a typical 11.34 kg (25 lb) batch test of 16x18 mesh coal. The 16x18 and 18x20 mesh tests all showed a transient profile similar to Fig. 6.19. Tests of particles larger than 4x6 all had insignificant CO deviations from background levels. For the intermediate size particles, some tests had a CO spike similar to Fig. 6.12, but others had none. The presence or absence of this CO spike could not be positively correlated with air flow rate or ratio of primary to secondary air flow.

The presence of CO during devolatilization indicates inadequate oxygen for complete combustion of hydrocarbons, at least locally to the particles. While oxygen concentration could not be recorded with the FTIR system, power plant

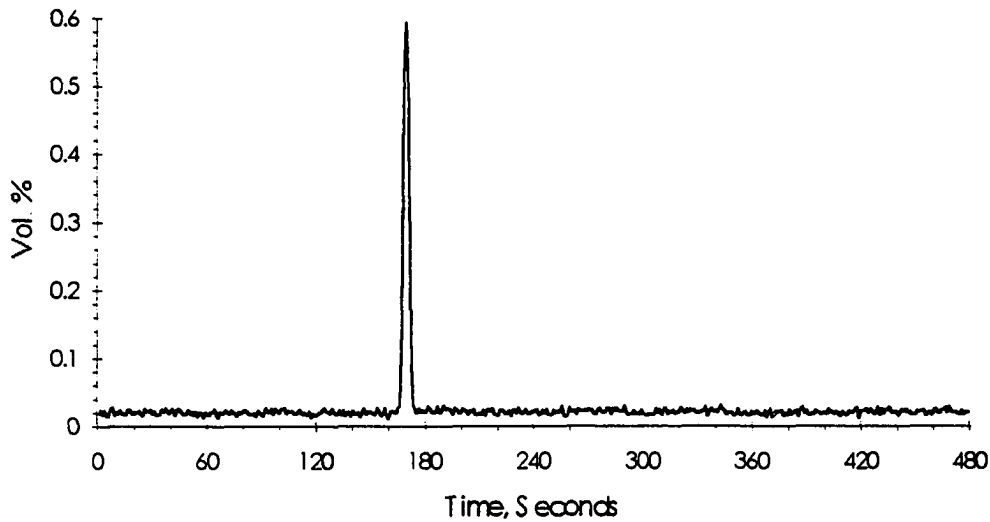


Figure 6.19: Typical CO profile for a batch test of 11.43 kg of 16x18 mesh coal

instrumentation indicated the oxygen concentration decreased during devolatilization to levels as low as 1%.

#### 6.4.2 Sulfur dioxide

Christofides [17] stated that sulfur in coal is released predominantly as  $\text{SO}_2$  during devolatilization, with smaller quantities released at the end of char burnout. Figure 6.20 is a plot of  $\text{SO}_2$  release with time for a batch test with 11.34 kg (25 lb) of 16x18 mesh coal. The  $\text{SO}_2$  release during devolatilization is very prominent, but a smaller peak towards the end of char burning, as described by Christofides [17], is indistinct. Small peaks do exist at about 240 and 300 seconds, but it is uncertain whether these are from char burning or are background fluctuations. Steady state background levels of  $\text{SO}_2$  varied from 250 to 500 ppm during normal operation. This variation in  $\text{SO}_2$  level at steady state was caused primarily by upper and lower limits on control limits (reduced during testing when the  $\text{SO}_2$  control was put in

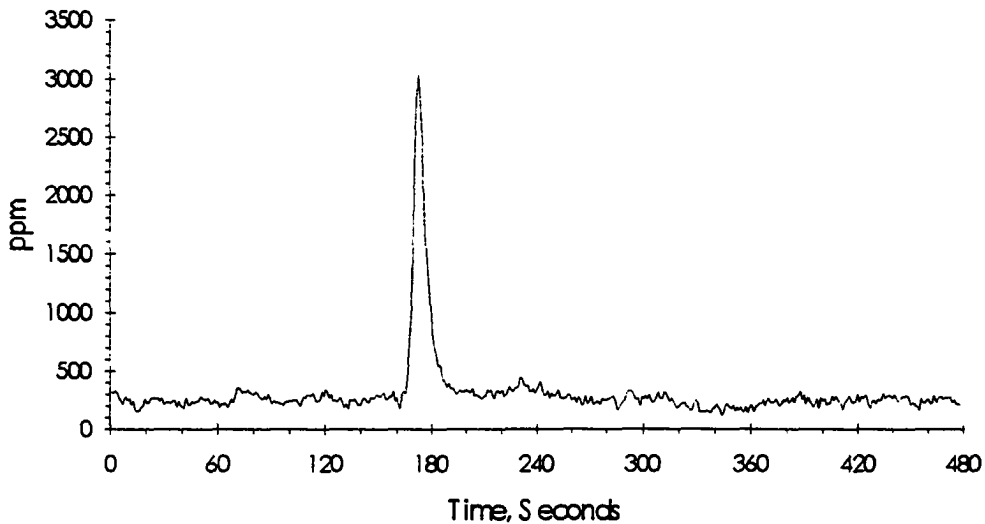


Figure 6.20: Typical  $\text{SO}_2$  profile for 11.34 kg batch test of 16x18 mesh coal

manual) and slight fluctuations in mechanical feed of coal and limestone.

The peak of the  $\text{SO}_2$  release during devolatilization was found to occur about 5-10 seconds later than the CO and  $\text{CO}_2$  peaks, indicating the sulfur was formed slightly slower than the CO and  $\text{CO}_2$ .

No  $\text{H}_2\text{S}$ , which is a primary product of the reaction between hydrogen and  $\text{FeS}_2$  (Eq. 2.80) in a fuel rich environment, was detected. Either it was all reacted before the combustion gases reached the sampling point, or it was below the lower detection limit of the system.

#### 6.4.3 Oxides of nitrogen

Figure 6.21 is a plot of  $\text{NO}_2$ , NO, and  $\text{N}_2\text{O}$  during a batch test of 11.79 kg (26 lb) of 6x8 mesh coal. The interference of methane with  $\text{N}_2\text{O}$  during evolatilization of small particles made evaluation of  $\text{N}_2\text{O}$  difficult. During devolatilization, NO distinctly decreases, while  $\text{N}_2\text{O}$  and  $\text{NO}_2$  increase slightly.

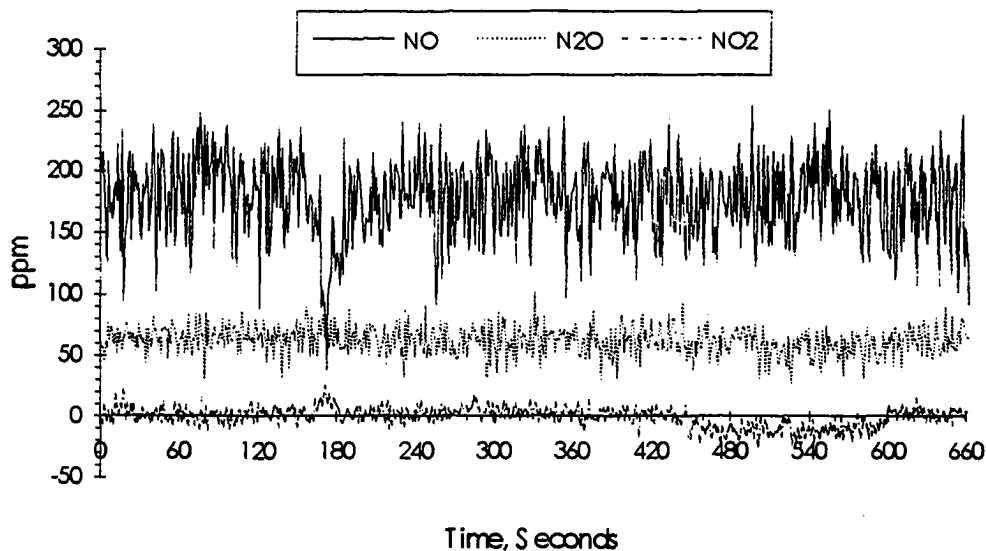


Figure 6.21: Typical profile of NO, N<sub>2</sub>O, and NO<sub>2</sub> for a batch test of 11.79 kg of 6x8 mesh coal

The NO<sub>x</sub> reactions are temperature dependent, but no discernible temperature changes from the power plant instrumentation were noted during the tests. Formation of NO requires high temperatures and adequate O<sub>2</sub>. In the CFB boiler the temperatures are not high (about 893°C in the combustion chamber) compared to optimum temperatures for NO formation. The oxygen level was maintained about 3.7% in the stack. The decrease in NO and increase in N<sub>2</sub>O is likely due to oxygen decrease upon batch input, at least locally to the particles. The scavenging affects of CO and staged combustion could also play a factor.

The NO was about 80-90% of the total NO<sub>x</sub>, with NO<sub>2</sub> being close to the lower detection limits of the FTIR system. The fluctuations in the NO concentration are believed primarily due to its low absorbance levels and the small number of scans taken, which causes a lower than desired signal to noise ratio. Because of this, the NO quantification is sensitive to the small amounts of noise in the baseline.

## 7. CONCLUSIONS

### 7.1 Laboratory Scale Testing

The FTIR detected rapid devolatilization transients in CO<sub>2</sub> at least as well as previously used NDIR equipment [16]. The FTIR was able to individually identify and quantify numerous gases, some of which could not be detected with the previously used NDIR instruments [16].

In addition to the expected products of combustion, the FTIR detected light hydrocarbons such as methane, acetylene, and ethylene. Some of these hydrocarbons had spectral features in regions that overlapped the main bands of the gases being quantified (especially methane for SO<sub>2</sub> & N<sub>2</sub>O) that the NDIR instruments did not detect and which could influence the results of the NDIR. Also, the transient trends of the various oxides of nitrogen could be detected, although trends during devolatilization were masked by hydrocarbons during these tests. Significant spectral features of hydrocarbons in the 1550-1200 cm<sup>-1</sup> region adversely impacted the quantification of SO<sub>2</sub>, N<sub>2</sub>O, and potentially NO<sub>2</sub>.

The evidence of CO and hydrocarbons during the devolatilization phase indicates that the combustion process of the coal is oxygen starved, at least locally to the particles.

The coal combustion model based on CO<sub>2</sub> concentrations, Eq. 2.73, fits the laboratory CO<sub>2</sub> emissions following a batch dump of coal. The plots used to calculate the time constants gave straight lines, indicating the exponential decay assumption for both devolatilization and char burnout is valid, at least for times much less than the char burning time. The devolatilization time,  $t_v$ , obeyed the power law relationship for  $d_i$  greater than 3.0 mm, with exponent equal to 1.75, which is in the range of values determined by other authors [16,25,52]. The power law exponent obtained for char

burning was 1.88, suggesting the combustion was dominated by diffusion control.

Calibration and operating procedures of the FTIR were confirmed in the laboratory prior to installing the system at the power plant with the CFB boiler to provide confidence that any differences in coal combustion found between the bubbling bed and CFB were attributable to different dynamics and not due to the FTIR system. The ability of the FTIR to both detect and quantify the products of combustion was verified. Spectral analysis was developed as an alternative to the time domain method of analysis.

## 7.2 Circulating Fluidized Bed Testing

The FTIR is a powerful tool for studying transient coal combustion processes in an on-line CFB boiler, without interrupting the boiler processes. It has been shown that the characterization of coal can be studied on-line during normal boiler operation. However, lack of control over boiler functions, such as air flow and bed temperature, make it difficult to vary these parameters and evaluate with confidence their affects on the combustion process. The present study, though, found no evidence that they affected the results.

The CFB boiler combustion dynamics are very complex, even more so than in the bubbling fluidized bed combustor. It is believed that staged combustion has an influence on some of the parameters studied here, but the specific impact could not be studied due to the limitation of having only one sampling point at the cyclone outlet.

Better calculation of characteristic times for devolatilization ( $\tau_v$ ) and char burning ( $\tau_c$ ) could be obtained by dumping larger batches of coal, which would give larger perturbations from the background level. However, this was

not feasible because larger perturbations caused adverse consequences on the plant operation.

The small volume of the gas cell used with the FTIR system made possible the study of fast combustion dynamics, but decreased the resolution and detection of trace species (such as HCl and H<sub>2</sub>S). Use of a longer path length cell to improve detection of such gases would diminish the system's utility to study rapid transients.

While CO and methane were present during devolatilization of every test in the bubbling bed combustor, they were present only for tests of smaller particle sizes in the CFB and the amounts were less than those seen in the bubbling bed. The presence of CO and methane indicated oxygen starvation occurred during devolatilization, at least locally to the particles.

Contrary to laboratory studies, char burnout did not begin until devolatilization was complete in the power plant tests. This result is in agreement with other authors, such as Saxena [54] and Ragland and Weiss [52] who theorized char combustion did not begin until devolatilization was complete.

The devolatilization time was found to be proportional to  $d_i^{0.73}$ . Char burnout dynamics differed significantly from those seen in the bubbling bed. Contrary to Christofides and Brown [16] who suggested devolatilization and char burning occurred simultaneously in the bubbling bed, the CO<sub>2</sub> profiles in the CFB boiler indicated that char burning did not commence until a short time after the completion of devolatilization. The char time constant was proportional to  $d_i^{0.54}$ , or  $d_i^{0.55}$ , depending on the method used to calculate it. This suggests the char combustion is controlled by chemical kinetics with primary fragmentation. This conclusion disagrees with past research conducted in bubbling fluidized beds or pulverized coal combustion which concluded that mass diffusion was the rate controlling mechanism.

Theory would indicate that the char time constant would be equal to 2 for diffusion control, and 1 for chemical kinetics control. With the much higher flow velocities in the CFB boiler, it is plausible that chemical kinetics control might dominate, rather than diffusion. This was the case, with  $\tau_c$  being proportional to  $d_i^{0.54}$ .

The burning rate of single particles was also studied. The burning rate determined in the CFB by this work is the same order of magnitude as reported by Basu [4]. The burning rate is expected to be proportional to  $d_i$  for diffusion control, and  $d_i^2$  for chemical kinetics control. This work found the burning rate to be proportional to  $d_i^{2.58}$ , again indicating chemical kinetics control with primary diffusion.

### 7.3 Spectral Analysis

Spectral analysis was developed as a powerful new method of determining char and devolatilization time constants from the transient  $\text{CO}_2$  emissions from coal combustion. The Bode plot obtained from spectral analysis was consistent with the assumption of rapid exponential devolatilization decay and slower exponential  $\text{CO}_2$  decay during char burning, at least for the bubbling bed data. Horizontal and -20 dB/decade straight line asymptotes fitted to the Bode plot provided two distinct cornering frequencies, corresponding to devolatilization and char time constants. Distinct cornering frequencies representing the reciprocals of  $\tau_v$  and  $\tau_c/3$  were observed. However, it was shown that a data set of minimum time length must be recorded for use with spectral analysis to prevent getting falsely low time constants.

For the bubbling bed combustor the time constants calculated with spectral analysis were in good agreement with those calculated using time domain methods for smaller particle sizes, where the time length of the data set was adequate. However, it was found that the time constants

calculated with spectral analysis were consistently smaller than those calculated with time domain methods for the larger particle sizes, indicating the lengths of the data sets were too short. Some order of magnitude estimate of the char time constant must be known before taking data to ensure taking data for a long enough time period for spectral analysis to be effective.

The background fluctuations in the CFB CO<sub>2</sub> data precluded its use for spectral analysis, as the "noise" introduced by the high frequency background fluctuations masked the actual spectral features.

#### **7.4 Recommendations for Future Work**

This work has demonstrated that characterization of coal is possible in an on-line CFB boiler. Many of the combustion models and theories in use were developed in stagnant flow or in bubbling fluidized beds. This work has shown that coal combustion dynamics can be studied in an on-line CFB boiler, allowing greater study of more realistic combustion conditions. The impact of staged combustion on the combustion process in the CFB is amenable to the type of research described in this work if additional gas sampling points were available. Better digital filtering methods would make spectral analysis of CFB boiler data with its fluctuating CO<sub>2</sub> background feasible. The primary and secondary air flow rates and coal feed rate respond to plant steam demand. Although this work did not indicate that varying these rates affected the calculation of the parameters studied, additional testing with some control of coal feed rate, primary air flow, and secondary air flow would provide information on if, or how, these parameters influence the combustion dynamics.

## BIBLIOGRAPHY

1. Anthony, D. B., Howard, J. B., Hottel, H. C., and Meissner, H. P. *Fifteenth Symp. (Int.) on Combustion*, The Combustion Institute, Pittsburgh, PA, pp 1303-1317 (1976).
2. Avedesian, M. M. and Davidson, J. F., *Trans. Instn. Chem. Engrs.* 51: 121-131 (1973).
3. Bates, S. C., Morrison, P. W. Jr., and Solomon, P. R., SPIE Vol. 1434 *Environmental Sensing and Combustion Diagnostics*, pp 28-38 (1991).
4. Basu, P., *Fuel* 56: 390-392 (1977).
5. Basu, P. and Fraser, S. A., *Circulating Fluidized Bed Boilers Design and Operations*; Butterworth-Heinemann: Boston, 1991.
6. Basu, P. and Halder, P. K., *Fuel* 68: 1056-1063 (1989).
7. Baumeister, T. (ed-in-chief), *Mark's Standard Handbook for Mechanical Engineers*; McGraw-Hill: New York, 1978.
8. Beér, J. M., *Sixteenth Symp. (Int.) on Combustion*, The Combustion Institute, Pittsburgh, PA, pp 439-459 (1976).
9. Bramer, E. A., Valk, M. *Fluidized Bed Combustion*, ASME, pp 701-706 (1991).
10. Brown, R. G., *Introduction to Random Signal Analysis and Kalman Filtering*; John Wiley: New York, 1983.
10. Chakraborty, R. K. and Howard, J. R., *J. Inst. Fuel* 51: 220-224 (1978).
12. Chakraborty, R. K. and Howard, J. R., *Chem. Eng. Commun.* 4: 705-719 (1980).
13. Chakraborty, R. K. and Howard, J. R., *J. Inst. Energy* 54: 48-54 (1981).

14. Chamberlain, J., *The Principles of Interferometric Spectroscopy*; John Wiley & Sons/Wiley Interscience: Chichester, 1979.
15. Chirone, R., Massimilla, L, and Salatino, P., *Prog. Energy Combust. Sci.* 17: 297-326 (1991).
16. Christofides, N. J. and Brown, R. C. *Combustion and Flame* 94: 449-461 (1993).
17. Christofides, N. J., "Determining char burning and sulfur sorption rates from dynamic analysis of CO<sub>2</sub> and SO<sub>2</sub> profiles", Ph.D. Dissertation, Iowa State University, 1993.
18. Compton, D. A. D., Young, J. R., Kollar, R. G., Mooney, J. R., and Grasselli, J. G., *Computerized Quantitative Infrared Analysis*, Gregory L. McClure (ed.); ASTM: Philadelphia, 1987; pp 36-57.
19. Conley, R. T., *Infrared Spectroscopy*; Allyn and Bacon, Inc.: Boston, 1972.
20. Cooper, B. R. and W. A. Ellingson (ed.), *The Science and Technology of Coal and Coal Utilization*; Plenum Press: New York, 1984.
21. Crocombe, R. A., Olson, M. L., and Hill, S. L. *Computerized Quantitative Infrared Analysis*; Gregory L. McClure (ed.); ASTM: Philadelphia 1987; pp 95-130.
22. Dakic', D., van der Honing, G, and Valk, M, *Fuel* 68: 911-916 (1989).
23. Dingle H., *The British Journal for the History of Science* 1: 199-216 (1963).
24. Doyle, W. M., *Process control and quality* 2: 11-41 (1992).
25. Essenhigh, R. H., *J. Eng. Power* 85: 183-190 (1963).
26. Essenhigh, R. H. *Chemistry of coal utilization*, Second Supplementary Vol., Martin A. Elliot (ed.); Wiley & Sons: New York, 1981; pp 1153-1312.
27. Field, M. A., *Combustion & Flame* 14: 237-248 (1970).

28. Graupe, D., *Identification of Systems*; R. E. Krieger Pub. Co.: Huntington, N.Y., 1976.
29. Griffiths, P. R. and de Haseth, J. A., *Fourier Transform Infrared Spectrometry*; John Wiley & Sons/Wiley-Interscience: New York 1986.
30. Hanst, P. L., *Fourier Transform Infrared Spectroscopy Applications to Chemical Systems* Vol. 2; Ed. by Ferraro, J. R., and Basile, L. J., Academic Press: New York, 1979; pp .
31. Hayhurst, A. N., *Combustion and Flame* 85: 155-168 (1991).
32. Helstrom, C. W., *Probability and Stochastic Processes for Engineers*; Macmillan: New York, 1991.
33. Howard, J. B. *Chemistry of coal utilization*, Second Supplementary Vol., Martin A. Elliot (ed.); Wiley & Sons: New York, 1981; pp 665-784.
34. Howarth, O. *Theory of Spectroscopy An Elementary Introduction*; John Wiley & Sons: New York, 1973.
35. Hoy, H. R. and Gill, D. W. *Principles for Combustion for Engineering for Boilers*, Lawn, (ed), Academic, New York, 1987; pp 521-619.
36. Jenkins, G. M., and Watts, D. G., *Spectral Analysis and Its Applications*; Holden-Day: San Francisco, 1968.
37. Johnston, S. F. *Fourier Transform Infrared a Constantly Evolving Technology*; Ellis Horwood: New York, 1991.
38. Junk, K. W. and Brown, R. C. *Combustion and Flame* 95: 219-228 (1993).
39. Junk, K. W. "A model of coal combustion dynamics in a fluidized bed combustor," Ph.D. dissertation, Iowa State University, Ames, Iowa, 1993.
40. Kanury, A. M. *Introduction to Combustion Phenomena*; Gordon and Breach Science Publishers: New York, 1975.
41. Kay, S. M., *Modern Spectral Estimation: Theory and Application*; Prentice Hall: Englewood Cliffs, New Jersey, 1988.

42. LaNauze, R. D. *Chem. Eng. Res. Des.* 63: 3-33 (1985).
43. LaNauze, R. D. and Jung, K., *Nineteenth Symp. (Int.) on Combustion*, The Combustion Institute, Pittsburgh, PA, pp 1087-1092 (1982).
44. Marban, G., Pis, J. J., and Fuertes, A. B., *Combustion and Flame* 103: 41-58 (1995).
45. Moritomi, H., Suzuki, Y., Kido, N., and Ogishu, Y., *Fluidized Bed Combustion*, ASME, pp 1005-1011 (1991).
46. Morrison, P. W., Jr., Cosgrove, J. E., Carangelo, R. M., Carangelo, M. D., Solomon, P. R., Leroueil, P., and Thorn, P. A. *Tappi Journal* 74: 68-78 (1991).
47. Neavel, R. C. *Chemistry of Coal Utilization*, Second Supplementary Vol., Martin A. Elliot (ed.); Wiley & Sons: New York; 1981, pp 91-158.
48. Ogato, K., *Modern Control Engineering*; Prentice-Hall: Englewood Cliffs, N. J. 1970.
49. Oude Lohuis, J. A., Tromp, P. J. J., and Moulijn, J. A., *Fuel* 71: 9-14 (1992).
50. Pillai, K. K., *Journal of the Institute of Energy* 58: 3-7 (1985).
51. Prins, W., Siemons, R., Van Swaaij, W. P. M., and Radovanovic, M., *Combustion and Flame* 75: 57-79 (1989).
52. Ragland, K. W., and Weiss, C. A., *Energy* 4: 341-348 (1979).
53. Ross, I. B. and Davidson, J. F. *Trans. of the Instn. of Chem. Eng.* 59: 108-114 (1981).
54. Saxena, S. C., *Prog. Energy Combust. Sci.* 16: 55-94 (1990).
55. Schobert, H. H. *Coal: The Energy Source of the Past and Future*; American Chemical Society: Washington, D. C., 1987.
56. Serio, M. A., Carangelo, R. M., Solomon, P. R., and Markham, J. R., *8<sup>TH</sup> Annual International Pittsburgh Coal Conference Proceedings* pp 1073-1078 (1991).

57. Smith, C., and Corripio, A., *Principles and Practice of Automatic Process Control*; Wiley: New York, 1985.
58. Smith, I. W., [B5] LaNauze, R. D. and Jung, K., *Nineteenth Symp. (Int.) on Combustion*, The Combustion Institute, Pittsburgh, PA, pp 1087-1092 (1982).
59. Smith, K. L., Smoot, L. D., and Fletcher, T. H. *Fundamentals of Coal Combustion for Clean and Efficient Use*, L. D. Smoot (ed.); Elsevier Science: Amsterdam, 1993; pp 131-298.
60. Solomon, P. R., Morrison, P. W. Jr., Serio, M. A., Carangelo, R. M., Markham, J. R., Bates, S. C., Cosgrove, J. E., SPIE vol. 1681 *Optically Based Methods for Process Analysis*, pp 264-275 (1992).
61. R. E. Sonntag and G. J. Van Wylen, *Fundamentals of Statistical Thermodynamics*; John Wiley & Sons, Inc.: New York, 1966.
62. Stubington, J. F., and Linjewile, T. M., *Fuel*: 68: 155-159 (1989).
63. Sundback, C. A., Beer, J. M., and Sarofim, A. F., *Twentieth Symp. (Int.) on Combust.*; The Combustion Institute: 1495-1503 (1984).
64. Thorne, A. P., *Analytical Chemistry* 63: 57A-65A (1991).
65. Valk, M. and Bijvoet, U. H. C. *Atmospheric Fluidized Bed Coal Combustion Research, Development and Application*, Valk, M. (ed); Elsevier Science: Amsterdam, pp 1-50, 1995.
66. Verweyen, N., Renz, U., and Reinartz, A. *Fluidized Bed Combustion*, ASME, pp 1401-1406 (1991).
67. Wall, T. F. *Principles for Combustion for Engineering for Boilers*, Lawn, C. J. (ed); Academic, New York: pp 197-264, 1987.
68. Wang, S. S., Gibbs, B. M., and Rhodes, M. J., *Combustion and Flame* 99: 508-515 (1994).

69. Wormhoudt, J. (ed.) *Infrared Methods for Gaseous Measurements, Theory and Practice*; Marcel Dekker, Inc.: New York, 1985.
70. Zeller, M. V. *Infrared Methods in Air Analysis*, Perkin-Elmer, Publication 993-9236.

**APPENDIX A: QUANTIFICATION PROGRAM**

This program takes the reprocessed spectra from OMNIC, removes the water vapor spectral regions, performs a baseline correct, and uses Quantir quantification methods to determine gas concentration at each sample time. This quantified data is stored on disk in text format for further analysis.

There are two main subroutines: Find\_factor and OpenSpectra\_Click. Find\_factor calculates the area under the water vapor spectrum to use in subtracting out the water vapor interference from the sample spectra. OpenSpectra\_Click loops through each of the spectra in the series data set to perform the gas quantification determination.

```
Sub Delay ()
```

```
For z = 1 To 10000
```

```
q = DoEvents()
```

```
Next z
```

```
End Sub
```

```
Sub Find_Factor (ReconstWin$, Arearef#)
```

```
Dim SpectRef#
```

```
' Open New Factor Window
```

```
ExecuteOMNIC "NewWindow ""Factor Window"""
```

```
ExecuteOMNIC "SelectWindow ""Factor Window"""
```

```
' Open H2O Reference Spectrum
```

```
ExecuteOMNIC "Import C:\OMNIC\cal_std2\h2o2r_50.spa"
```

```
' Determine area under H2O Peak
```

```
' Baseline: 1958.6-803; Region: 1440-1426
```

```
ExecuteOMNIC "CorrectedPeakArea 1958.6 1440.0 1426 803 "
```

```
' Pull out the Reference Area from the H2O Data Set
```

```
RefArea$ = GetOMNIC("Result Current")
```

```
Arearef# = GetVal(RefArea$, "Area")
```

```
' ExecuteOMNIC "DeleteSpectrum"
```

```
' Switch to the Series Reconstruct Window
```

```
ExecuteOMNIC "SelectWindow " & ReconstWin$
```

```
ExecuteOMNIC "CloseWindow No ""Factor Window"""
```

```
End Sub
```

```
Sub Form_Load ()
```

```
'Load OMTALK services and maximize OMNIC application window.
```

```
Load OMTALK
```

```
End Sub
```

```

Sub OpenSpectra_Click ()
' NOTE! This Program Assumes that the Data File has
already been reprocessed to Absorbance!
Msg = "This Quantification Program Makes the Following
Assumptions: "
Msg = Msg & "Series Data Taken at 2 resolution, 600mm Hg
Pressure, 2 scans (=1.03 second interval) "
Msg = Msg & "Data has been reprocessed to Absorbance.
Quant optimized for 10/2/95 & later data"
MsgBox (Msg)

i% = StartOMNIC(4, "")
' Open New window with name QuantWindow
ExecuteOMNIC "NewWindow ""QuantWindow""
errmsgbox
' Open up the series data set to be quantified
ExecuteOMNIC "OpenDataSet "
errmsgbox
ReconstWin$ = "" + GetOMNIC("Window Title") + ""
' Set the time interval between samples, assumes 1.03
second sampling rate
GCTime! = .0173
' Open file for storing data after quantification:
Msg = "Enter File Name for saving data, including
extension; "
Msg = Msg & "Default directory is c:\temp"
Title = "Filename Input"
Fnamein = InputBox(Msg, Title)
' Input total length of the Series Data Set
Msgtime = "Enter Total Time of Series Data Set; in
Minutes"
Title = "Time Input"
Series_time = InputBox(Msgtime, Title)
Number_Points% = (Series_time / .01732) - 1
'
' Find Factor for Subtraction
Call Find_Factor(ReconstWin$, Arearef#)
'
Open "c:\temp\" & Fnamein For Output As #1
Write #1, ReconstWin$
Write #1, "Time,s", "TimeGC,s", "CO2", "SO2", "CO", "NO2",
"NO", "N2O", "Factor"
' Loop through the Gram_Schmidt or Rapid Scan for all
the spectra
For Number% = 1 To Number_Points%
x = DoEvents()
errmsgbox
Window$ = "" + "QuantWindow" + ""
' Extract current spectrum and place in QuantWindow for
quantification
cmd$ = "ExtractSpectrum " + Str$(GCTime!) + " " + Window$

```

```

ExecuteOMNIC cmd$
' Open the Quant Window
ExecuteOMNIC "SelectWindow ""QuantWindow""
' Find Area Under H2O Spectrum for Subtraction Factor
ExecuteOMNIC "CorrectedPeakArea 1958.6 1440 1426 803"
SpectArea$ = GetOMNIC("Result Current")
AreaSpect# = GetVal(SpectArea$, "Area")
Factor = AreaSpect# / Arearef#
Subfactor$ = Str$(Factor)
SpectralTitle$ = GetOMNIC("Spectrum Title")
errmsgbox
'
' Get spectrum time from spectrum title for more exact
timing
TrimTitle$ = RTrim$(SpectralTitle$) 'Trim off the spaces
to the right
TrimTitle2$ = Right$(TrimTitle$, 11) ' Pull off the right
10 characters
Spect_Time = Val(TrimTitle2$) * 60' Numeric value of the
string, In seconds
'
' Import the H2O File to be used for Water Vapor
Subtraction
ExecuteOMNIC "Import C:\omnic\cal_std2\h2o2r_50.spa"
' Select this spectrum as the first
ExecuteOMNIC "Select First"
Msg = "Pause"
' Select the Data spectrum as the Next spectrum
ExecuteOMNIC "Select Next"
' Select the Water Vapor spectrum as the second of two
spectra for subtraction
ExecuteOMNIC "Select First Shift"
' Perform the subtraction of the water vapor from the
data spectrum
ExecuteOMNIC "Subtract " & Subfactor$
ExecuteOMNIC "AutoBaseline"
'
' Get the values of the quantification from Result
Current
' This may need to be modified to correspond the the
gases in the quant method
'
' Quantify CO with Optimized quant method 9/21/95.
ExecuteOMNIC "QuantSetup COPWRPLO.QNT"
ExecuteOMNIC "Quantify"
QuantResults$ = GetOMNIC("Result Current")
CO = GetVal(QuantResults$, "Carbon Monoxide")
'
' Quantify SO2 with Optimized quant method, 2 pt
baseline, High Conc.
ExecuteOMNIC "QuantSetup 2RES600S.QNT"

```

```

ExecuteOMNIC "Quantify"
QuantResults$ = GetOMNIC("Result Current")
SO2 = GetVal(QuantResults$, "Sulfur Dioxide")
'
' Quantify NO2 with Optimized quant method.
ExecuteOMNIC "QuantSetup 2RESNO26.QNT"
ExecuteOMNIC "Quantify"
QuantResults$ = GetOMNIC("Result Current")
NO2 = GetVal(QuantResults$, "Nitrogen Dioxide")
'
' Quantify NO with Optimized quant method 9/21/95.
ExecuteOMNIC "QuantSetup NOPWRPLT.QNT"
ExecuteOMNIC "Quantify"
QuantResults$ = GetOMNIC("Result Current")
NO = GetVal(QuantResults$, "Nitric Oxide (NO)")
'
' Quantify N2O with Optimized quant method 9/21/95.
ExecuteOMNIC "QuantSetup N2OPWRPM.QNT"
ExecuteOMNIC "Quantify"
QuantResults$ = GetOMNIC("Result Current")
N2O = GetVal(QuantResults$, "Nitrous Oxide (N2O)")
'
' Quantify CO2 with Optimized quant method 7/11/95; HTD.
ExecuteOMNIC "QuantSetup 2RESCO26.QNT"
ExecuteOMNIC "Quantify"
QuantResults$ = GetOMNIC("Result Current")
CO2 = GetVal(QuantResults$, "Carbon Dioxide ")
'
errmsgbox
' Clear All the Spectra to Start All Over Again With the
Next Spectrum
ExecuteOMNIC "Select All"
ExecuteOMNIC "DeleteSelectedSpectra"
' Correct time from minutes to seconds
Abstime = GCTime! * 60
' Write data to disk
Write #1, Abstime, Spect_Time, CO2, SO2, CO, NO2, NO,
N2O, Factor
Text1.Text = Text1.Text + Str$(Number%) + " " +
SpectralTitle$ + Chr$(13) + Chr$(10) + QuantResults$
ExecuteOMNIC "SelectWindow " & ReconstWin$
errmsgbox
Form1.Show
GCTime! = GCTime! + .01732
Next Number%
EndOMNIC
End Sub

```

**APPENDIX B: PROGRAM TO DEVELOP BODE PLOT**

This program takes the FTIR quantification data for CO<sub>2</sub> profile and calculates the Bode plot used to find the devolatilization and char time constants. The steady state background level has been removed and the time zero starts at the CO<sub>2</sub> peak during devolatilization. Comment lines are preceded by a percent sign. MATLAB is case sensitive. The semicolons at the end of each command prevent the entire vector from scrolling on the screen. The data has been taken from an Excel file saved as two columns, time and CO<sub>2</sub>, in text format.

```
%
% Nomenclature
% t = time vector
% tp = padded time vector
% C = vector of CO2 data
% Cp = padded CO2 data vector
% deltat = the time interval,  $\Delta t$ 
% N = total number of data points
% Fy = fast fourier transform of the CO2 data
% Fyp = FFT of padded CO2 data
% P = number of data points in zero padded data set
% Pyy = PSD of the data
% Pryp = PSD of the padded data
% Db = PSD converted to decibels
% Dbp = PSD of padded data set converted to decibels
% faxis = frequency vector
% faxisp = frequency vector for padded data set
% A, the input matrix, has been loaded.
% plot C versus t to verify data is correct

t=A(1:N,1);
```

```

C=A(1:N,2);
plot(t,C);

%   Input the variable parameters
N=256;    % or whatever value it is
P=4000;
deltat=t(N)/(N--1);
tp=[0:deltat:deltat*(P-1)];
Cp=ones(size(tp))*C(N);
Cp(1:N)=C(1:N);
plot(tp,Cp);

%   Calculate the FFT of C
Fy=fft(C);
Fyp=fft(Cp);

%   The FFT is squared by use of the complex conjugate, .*
Pyy=Fy.*conj(Fy)/N;
Pryp=Fyp.*conj(Fyp)/P;

%   Convert the PSD to decibels
%   Only half of the data is used, as it is symmetric and the
%   second half does not yield useful information
Db=10*log10(Pyy(1:N/2));
Dbp=10*log10(Pryp(1:P/2));

%   Calculate the frequency, faxis
faxis=2*pi*(1:N/2)/t(N);
faxisp=2*pi*(1:P/2)/tp(P);

%   plot Db versus faxis on a semilog plot, both padded and
unpadded
semilogx(faxis,Db,faxisp,Dbp);

```

### APPENDIX C: UNCERTAINTY ANALYSIS

The CO<sub>2</sub> concentration is determined from the quantification of the sample in the gas cell is a function of the calibration gas concentration, pressure, temperature, and the quantification linear regression:

$$\text{CO}_2 = f(\text{P}, \text{T}, \text{cal gas}, \text{and Quantir regression}) \quad (\text{C.1})$$

For the CO<sub>2</sub>, the calibration gas tolerance is 1%. Pressure in the cell was maintained within 6 mm Hg during sampling, the temperature within 1°, and the Quantir regression was within 5%. From this the CO<sub>2</sub> uncertainty is:

$$\frac{u_{\text{CO}_2}}{\text{CO}_2} = \left(\frac{u_{\text{P}}}{\text{P}}\right)^2 + \left(\frac{u_{\text{T}}}{\text{T}}\right)^2 + \left(\frac{u_{\text{Tol}}}{\text{CO}_2 \text{conc}}\right)^2 + \left(\frac{u_{\text{Quant}}}{\text{Quant}}\right)^2 \quad (\text{C.2})$$

Substituting the values for the above, the uncertainty is:

$$\left(\frac{u_{\text{CO}_2}}{\text{CO}_2}\right)^2 = \left(\frac{6}{600}\right)^2 + \left(\frac{1}{181}\right)^2 + (.01)^2 + (.05)^2 \quad (\text{C.3})$$

giving: 
$$\left(\frac{u_{\text{CO}_2}}{\text{CO}_2}\right) = 5.2\% \quad (\text{C.4})$$

The devolatilization time constant is calculated for the CFB boiler data from:

$$\tau_v = \frac{-t}{\ln\left(\frac{[\text{CO}_2]_R}{[\text{CO}_2]_S}\right)} \quad (\text{C.5})$$

For the worst case values of the CFB boiler data, the uncertainty of  $t$  is .1 second over 20 seconds,  $[\text{CO}_2]_R - [\text{CO}_2]_S$  is about 1% CO<sub>2</sub>, and the uncertainty is the CO<sub>2</sub> concentration

is 7%, based on the residuals of the steady state fluctuations. Applying a Taylor series expansion to obtain the uncertainty, the following is obtained:

$$\left(\frac{u_{\tau v}}{\tau v}\right)^2 = \left(\frac{u_t}{t}\right)^2 + 2\left(\frac{u_{CO_2}}{\ln([CO_2]_R - [CO_2]_S)}\right)^2 \quad (C.6)$$

Inserting the values:

$$\left(\frac{u_{\tau v}}{\tau v}\right)^2 = \left(\frac{.1}{100}\right)^2 + 2\left(\frac{.07 * .125}{\ln(.01)(.01)}\right)^2 \quad (C.7)$$

giving: 
$$\left(\frac{u_{\tau v}}{\tau v}\right) = 38\% \quad (C.8)$$

The char time constant is calculated from the slope of:

$$\ln(m(t)/m_i)^{1/3} \quad (C.9)$$

vs time. From this  $\tau_c$  is a function of  $m$ ,  $m_i$ , time,  $Q$ ,  $CO_2$  concentration:

$$\left(\frac{u_m}{m}\right)^2 = \left(\frac{u_{CO_2 R}}{[CO_2]_R}\right)^2 + \left(\frac{u_Q}{Q}\right)^2 + \left(\frac{u_t}{t}\right)^2 + \left(\frac{u_{CO_2 S}}{[CO_2]_S}\right)^2 \quad (C.10)$$

From Eq. C.4  $\left(\frac{u_{CO_2}}{[CO_2]}\right) = 5.2\%$  and  $(u_Q/Q) = 5\%$ . Substituting into C.10 gives:

$$\left(\frac{u_m}{m}\right)^2 = (.052)^2 + (.05)^2 + \left(\frac{.1}{100}\right)^2 + (.052)^2 \quad (C.11)$$

giving:

$$\left( \frac{u_m}{m} \right) = 9.7\% \quad (\text{C.12})$$

The char time constant  $\tau_c$  uncertainty is calculated from:

$$\left( \frac{u_{\tau_c}}{\tau_c} \right)^2 = \left( \frac{u_m}{m} \right)^2 + \left( \frac{u_t}{t} \right)^2 \quad (\text{C.13})$$

Substituting in the worst case values for the CFB boiler data:

$$\left( \frac{u_{\tau_c}}{\tau_c} \right)^2 = (.097)^2 + \left( \frac{.1}{100} \right)^2 \quad (\text{C.14})$$

Giving and uncertainty of  $\tau_c$  of:

$$\left( \frac{u_{\tau_c}}{\tau_c} \right) = 9.8\% \quad (\text{C.15})$$